Photovoltaic Thermal System Design Including Aquifer Thermal Energy Storage in a Fifth Generation District Heating Network in Hilversum

MSc Sustainable Energy Technology

Ties Beijneveld

TU Delft

Delft University of Technology

Thesis Sustainable Energy technology

Photovoltaic Thermal System Design Including Aquifer Thermal Energy Storage in a Fifth Generation District Heating Network in Hilversum

Author
Ties Beijneveld

Supervisors
Dr. Laura Ramirez Elizondo
Joel-Alpízar Castillo
Darío Slaifstein

September 6, 2024

Abstract

The pressing need to mitigate global warming and transition to sustainable energy solutions has accelerated the development of innovative energy systems. This thesis investigates the sizing and design of a photovoltaic thermal (PVT) system integrated with aquifer thermal energy storage (ATES) within a fifth-generation district heating network (5GDHN) for a case study in the Werfgebied district in Hilversum, Netherlands. The study focuses on the configuration, storage distribution, and optimisation of component sizing within the district heating network to minimise overall electrical power usage, thus reducing grid dependency and CO_2 emissions. A Python model of the multi-energy carrier system is developed, embedding the physical principles underlying the thermal and electrical properties of the components. The research finds that an optimal configuration for the ATES and PVT combination involves a single ATES well rather than distributed thermal energy storage. The results indicate that the size of the aquifer significantly affects the overall operating temperature and its fluctuations. A larger ATES maintains a stable but relatively colder temperature. Optimal sizing is achieved at the maximum allowed operating temperatures of an ATES in these areas, resulting in the most favorable temperature for maximum COP in the heat pumps. This minimises grid exchange and CO_2 emissions. The optimal ATES size is determined to be 380,000 m^3, in combination with 800 PVT modules, leading to a total CO_2 equivalent emission of 856 tonnes.

Preface

This thesis report is submitted as part of my Master's program in Sustainable Energy Technology at TU Delft. It focuses on optimising a district heating network with photovoltaic thermal modules and aquifer thermal energy storage.

I would like to thank my supervisors for their guidance throughout this project. Thanks to Joel and Dario for our weekly meetings, which provided insightful tips and stimulating discussions on the topic. I am also particularly grateful for your previous research insights and the opportunity to use your calculation models. Additionally, I would like to thank Laura for the opportunity to complete my thesis at DCE&S, as well as for our monthly meetings and feedback on the overall research structure, especially regarding my main research questions.

I also wish to thank Jeroen and Tjalling from HET, and Stefan from the municipality of Hilversum, for providing a real-life district heating network case study for my research. I am eager to see the final results of the building project.

Ties Beijneveld
Delft, September 2024

Contents

1 Introduction **4**
- 1.1 Hilversum Project . . . 5
- 1.2 Components . . . 6
  - 1.2.1 Photovoltaic Thermal modules . . . 6
  - 1.2.2 Heat Pumps . . . 6
  - 1.2.3 Fifth Generation District Heating Network . . . 7
  - 1.2.4 Aquifer Thermal Energy Storage . . . 9
- 1.3 Research . . . 10
  - 1.3.1 Research Questions . . . 10
  - 1.3.2 Research gap . . . 10
  - 1.3.3 Contribution . . . 11
  - 1.3.4 Approach . . . 12

2 Modelling **13**
- 2.1 Thermal components . . . 13
  - 2.1.1 Photovoltaic Thermal . . . 13
  - 2.1.2 Aquifer Thermal Energy Storage . . . 17
  - 2.1.3 Heat pumps . . . 18
  - 2.1.4 District Heating . . . 19
  - 2.1.5 Thermal Demand . . . 23
- 2.2 Electrical components . . . 26
  - 2.2.1 Photovoltaic . . . 26
  - 2.2.2 Heat Pumps . . . 26
  - 2.2.3 Electrical Demand . . . 26
  - 2.2.4 ATES Hydraulic Pumps . . . 27
- 2.3 Component connection . . . 28
  - 2.3.1 Thermal Network . . . 28
  - 2.3.2 Electrical Network . . . 30
  - 2.3.3 District . . . 31

3 Distribution and Configuration **32**
- 3.1 Centralised ATES . . . 32
- 3.2 Distributed ATES . . . 44
- 3.3 Configuration . . . 53
- 3.4 Results . . . 57
- 3.5 Discussion . . . 58

4 Sizing **60**
- 4.1 Component size analysis . . . 60
- 4.2 Long term operation analysis . . . 67
- 4.3 Results . . . 69
- 4.4 Discussion . . . 70

5 Optimisation **71**
- 5.1 CO_2 emissions . . . 71
- 5.2 Optimisation problem . . . 72
- 5.3 Results . . . 74
- 5.4 Discussion . . . 78

6 Conclusion **79**
- 6.1 Future research . . . 80

A Appendix **C**
- A.1 Parameters model . . . C
- A.2 Operating temperatures optimisation . . . E
- A.3 Model inputs . . . E

1 Introduction

The escalating challenges of global warming and the urgent need for sustainable energy solutions have led to the development of a fifth-generation district heating network (5GDHN) in Hilversum, Netherlands. This pioneering initiative is a collaboration between the company HET and the municipality of Hilversum. It features the integration of a photovoltaic-thermal (PVT) carport, positioning it at the forefront of innovative energy systems. This project leverages renewable energy sources to provide sustainable district heating.

The urgency of transitioning away from fossil fuels and reducing greenhouse gas emissions has never been more clear. With the world's primary energy consumption heavily dependent on non-renewable sources, the resultant environmental impact underscores the necessity for a shift towards more sustainable and resilient energy systems. Globally, fossil fuels constitute 80% of the total energy supply [1]. In the Netherlands, this figure rises to 84% for total energy consumption. Within the domestic sector in the Netherlands, 15% of energy originates from solar or wind sources [2]. The necessary energy transition aligns with the global commitments outlined in the United Nations' Sustainable Development Goals and the Paris Agreement, which aim to limit global warming to well below 2 degrees Celsius above pre-industrial levels.

The European Union and the Netherlands have embarked on ambitious paths to reduce their carbon footprints and transition towards renewable energy sources. In this context, the implementation of district heating networks, especially 5GDHNs, offers a promising avenue for enhancing energy efficiency, reducing carbon emissions, and easing overall network congestion. By integrating low-temperature operations with renewable energy technologies such as photovoltaic thermal modules, thermal storage, and heat pumps, 5GDHNs represent a significant advancement in district heating systems. This integration not only optimises energy distribution but also lessens the strain on electrical grids, contributing to a more resilient and efficient energy infrastructure.

This thesis project focuses on the configuration, sizing and optimisation of the components of an implemented 5GDHN in the Werfgebied located in Hilversum. Through a comprehensive analysis of the technological challenges, this research aims to uncover how such innovative systems can be optimally designed to minimise the CO_2 emissions. The insights gained from this study are intended to contribute in 5GDHN research and aid the Netherlands in meeting its climate targets, showcasing the role of advanced heating networks in facilitating a transition towards a more sustainable and resilient energy future.

This chapter will explain the project planned for development in Hilversum. Following this, the individual components of the 5GDHN will be introduced. Subsequently, the research framework will be detailed, starting with the formulation of research questions. The research section will then delve into identifying the literature gap, highlighting the study's scientific contribution, and ending with an explanation of the research approach.

1.1 Hilversum Project

In Hilversum-Oost, the Werfgebied, a diverse area encompassing offices, industrial production, hospitality, and residential housing, is undergoing a transformation towards sustainability. This initiative, led by the Vereniging duurzaam Werfgebied (VDW)—a collective of four real estate partners—aims to make the district energy-neutral by 2028. The VDW's preliminary research has laid the groundwork for this ambitious project [3].

This research looks into the current building landscape and forthcoming construction plans to identify opportunities for sustainable development and energy efficiency improvements. It also assesses existing energy consumption patterns and evaluates ongoing sustainability efforts, projecting their impact up to 2028. A significant focus is on exploring innovative solutions for further enhancing sustainability, such as renewable energy sources and smart energy management systems, with the ultimate goal of achieving energy neutrality.

By reimagining the Werfgebied as a more residential and sustainably designed area, this initiative reflects a committed step towards a greener future, setting a precedent for sustainable urban development in Hilversum and beyond. A digital image of the construction plans of the Werf neighbourhood is shown in Figure 1.

Figure 1: New Construction Development Werf [3]

The journey towards energy neutrality in the Hilversum project is underpinned by a comprehensive strategy comprising several critical building blocks: Energy conservation in existing constructions and energy-neutral new buildings, local energy generation (with a special focus on electricity and heat), sustainable mobility, and innovative storage solutions. While each component plays a crucial role in the overarching goal of achieving energy neutrality, the focus of this research centers predominantly on the heat aspect, exploring its potential and implementation intricacies in depth.

The heating strategy comprises several key components:

1. Individual heat pumps per building: This foundational element involves installing dedicated heat pumps for each building.
2. PVT systems: Particularly envisaged for deployment at the solar parking lot Mussenstraat, these systems combine solar photovoltaic (PV) modules with thermal collectors.
3. Connection to a district heating network: An integration of a 5GDHN, originating from the local wastewater treatment plant.

In the coming years, the Werfgebied can evolve from an industrial estate into a completely energy-neutral, and even energy-positive, residential and working area, where energy efficiency is linked to sustainability and a pleasant living and working climate. In doing so, the Werf contributes to national and municipal climate objectives, and it appears likely that this will also be financially wise [3].

1.2 Components

In this subsection, the essential technologies that underpin the Werf's transformation into an energy-neutral and potentially energy-positive hub are introduced: PVT systems, heat pumps, 5GDHN, and aquifier thermal energy storage (ATES). These components, crucial for harnessing, converting, and storing energy efficiently, are briefly overviewed here to set the stage for a detailed exploration later on.

1.2.1 Photovoltaic Thermal modules

PVT systems represent an innovative approach in solar energy technology, integrating solar thermal (ST) and PV modules into a single system. This multidisciplinary configuration allows for dual energy extraction: electricity generation through the photovoltaic process and thermal energy capture for heating purposes. The synergy between PV and ST components in PVT systems facilitates a higher overall conversion efficiency of solar radiation compared to what individual PV or ST modules can achieve independently [4]. This efficiency boost is one of the key advantages of PVT technology, making it a more attractive option for those seeking to maximize the utilization of solar energy. Economically, PVT systems are also very attractive. The combined generation of thermal and electrical energy leads to a faster payback on investment compared to installing separate PV and ST systems [5].

An additional advantage of PVT systems lies in their operational efficiency. By extracting heat from the module, PVT systems help mitigate the efficiency loss typically experienced by PV modules under high temperatures. In standard PV modules, excessive heat can lead to thermalization losses, where energy from solar radiation is converted into heat instead of electricity, and non-absorption losses, where part of the solar spectrum is not absorbed and thus not converted into any form of useful energy. The thermal management feature of PVT systems reduces these losses by maintaining the PV cells at a more optimal operating temperature [4].

The integration of electrical and thermal components in PVT systems improves the system's overall efficiency. A PVT has a thermal efficiency between 27% and 79% and photovoltaic efficiency between 6.4% and 58% [6], resulting in a total efficiency between 45% and 91%. This enhancement in global efficiency can be quantified by the sum of the electrical and thermal efficiencies. By harnessing both solar electricity and heat, PVT systems achieve a significantly higher overall efficiency compared to traditional PV cells alone.

1.2.2 Heat Pumps

Heat pump systems have emerged as a cornerstone in the transition towards residential heating electrification, offering a highly efficient alternative to traditional heating methods. At the heart of a heat pump's operation lies a specialised fluid, chosen for its boiling points which are lower than typical outdoor temperatures. This fluid undergoes a cyclical process that begins with boiling using an evaporator and transitioning it into a gas. Once gaseous, the fluid is compressed, a step that significantly increases its temperature [7].

This heated gas is then channeled through a heat exchanger, where it imparts its heat to the heating system before being depressurised. The reduction in pressure causes the gas to condense, reverting it back to its liquid form and readying it for the next cycle. This operation principle is what makes heat pumps very efficient, with an efficiency rating 3 to 4 times greater than that of conventional fossil fuel boilers [8]. The efficiency of heat pumps is not only beneficial in terms of energy savings but also contributes significantly to reducing carbon emissions associated with residential heating.

Within this research, water-to-water heat pumps are considered. These systems operate by extracting heat from water sourced from district heating networks to evaporate the refrigerant. This method allows for the utilisation of existing thermal energy in water, increasing the efficiency of the heat transfer process and reducing the overall energy consumption required for heating. The typical working principle of a water to water heat pump is shown in Figure 2.

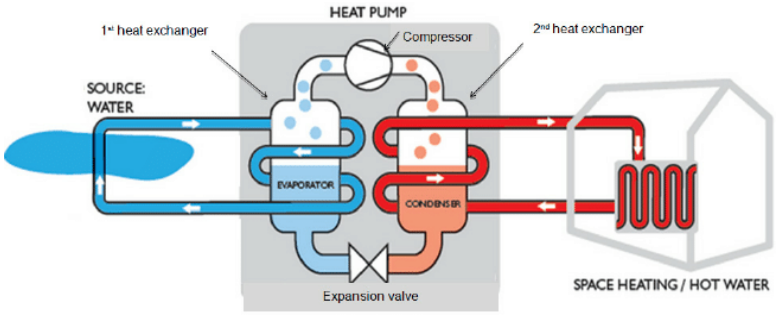

Figure 2: A typical diagram of a water source heat pump [9].

Integrating heat pump systems with PVT systems offers a comprehensive solution for residential heating. The prioritized electricity source for the heat pumps is generated by the PV component of the PVT systems before extracting power from the grid, significantly enhancing the system's independence in meeting heating demands.

1.2.3 Fifth Generation District Heating Network

District heating networks serve as an efficient conduit for the delivery of heat from various energy sources to end-users through an intricate underground piping system. The latest advancement in this domain is the Fifth Generation District Heating networks (5GDHN), which epitomize the cutting-edge in thermal energy distribution technology.

5GDHN are designed to simultaneously fulfill both heating and cooling requirements using an ultra-low temperature distribution system, operating below 45°C. These networks are characterized by the presence of bidirectional heat substations outfitted with water-to-water heat pumps. These pumps are capable of adjusting temperatures to meet user-specific demands, thereby facilitating a seamless integration between thermal and electrical grids. The dual-pipeline system, consisting of cold and warm conduits, is a hallmark of 5GDHN networks, enabling the transfer of heat where it is most needed across the network. This design principle allows for the efficient utilisation of waste heat or cooling from one user to satisfy the demand of another, enhancing overall system efficiency. A crucial element of 5GDHN networks is the end-users' substations, which play an important role in meeting the thermal energy needs of buildings. In the context of 5GDHN, these substations function both as recipients and contributors of thermal energy [10].

One of the notable advantages of 5GDHN networks is their operation at temperatures close to that of the ground, significantly minimising heat losses during distribution, especially in urban settings where low-grade heat sources are readily accessible [10]. Moreover, the integration of heating, cooling, and electricity grids, alongside thermal energy storage technologies, provides 5GDHN networks with unparalleled flexibility. This combination enables the provision of thermal energy at various temperatures and timescales, introducing a new era of heating sector electrification through the use of decentralised heat pumps or chillers. The design of 5GDHN networks also enhances energy and cost efficiency by leveraging both heating and cooling sources, particularly beneficial when these demands coexist. The decentralised nature of low-grade energy sources negates the need for extensive pipeline construction. Figure 3 shows a representation of a 5GDHN.

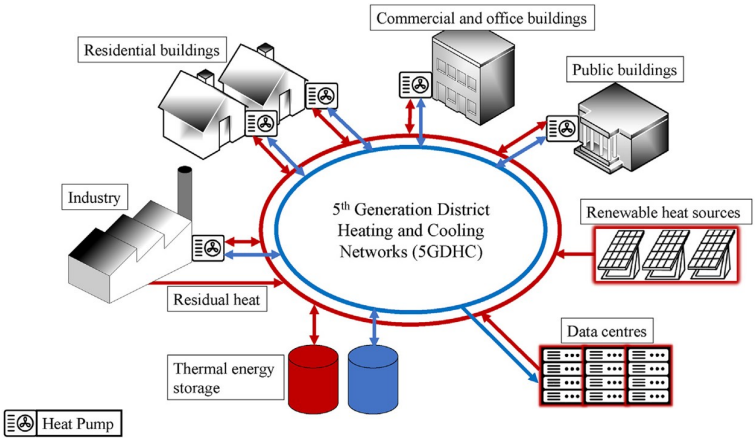

Figure 3: A representation of a typical fifth generation district heating and cooling network [10].

However, the system is not without its challenges. The low operational temperatures increase pumping costs due to the volume of water required. Additionally, to meet specific heat demands, a supplementary boost in temperature may be necessary. Despite these considerations, the benefits of 5GDHN networks, particularly in terms of efficiency, flexibility, and cost-effectiveness, make them a compelling option for modern urban heating and cooling solutions.

1.2.4 Aquifer Thermal Energy Storage

ATES, short for aquifer thermal storage, presents an innovative approach to subterranean thermal storage. This method falls under the broader category of Underground Thermal Energy Storage (UTES), which is divided into open or closed systems. Specifically, ATES operates as an open system where groundwater is withdrawn and then reinjected into the ground through wells, facilitating the transfer of thermal energy into and out of an aquifer. This process enables the utilisation of groundwater as a thermal fluid within district heating networks. In contrast to closed systems, where typically water is circulated through underground heat exchangers, ATES uses aquifers, water-bearing geological formations. The operation of ATES typically involves two hydraulically connected wells, designed to segregate the water supply from its storage function [11]. An Illustration of the basic working principle of a low-temperature seasonal ATES system with example temperatures is shown in Figure 4.

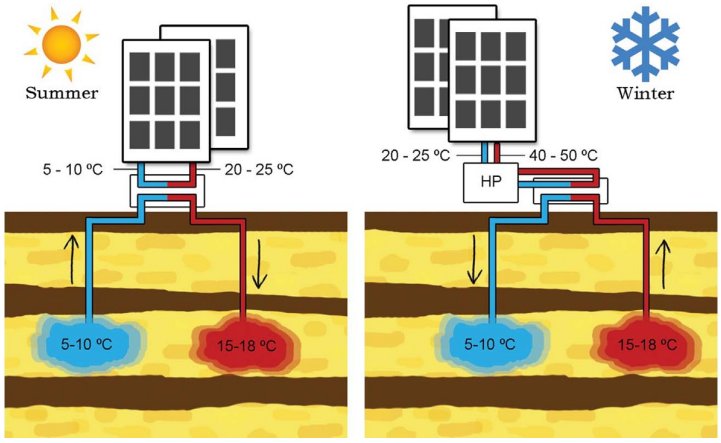

Figure 4: in Left: in direct cooling mode while storing heat for winter. Right: vice-versa in heating mode supported by a heat pump while storing cooling capacity for summer [12].

A notable advantage of open systems like ATES over closed systems is their superior heat transfer capabilities, primarily due to the efficiency of wells compared to boreholes. The ATES system involves drilling a few wells into an aquifer to facilitate the circulation of water between the storage area and the energy system. The system is adept at storing energy while concurrently providing heating and cooling solutions on a seasonal basis. The design of well spacing and depth ensures the separation of warm and cold storages, preventing thermal crossover within the same season. The Netherlands emerges as a leader in ATES technology, propelled by positive experiences with aquifer storage in subsequent projects and the widespread availability of aquifers across the country, leading to further advancements in ATES applications [11].

1.3 Research

The conducted research is on component configuration, storage distribution and sizing of the earlier mentioned components. These three aspects will be optimised for the lowest CO2 emissions possible. The project, which will be built in Hilversum is used as case study to research and analyse how components respond in a low temperature district heating network. This section includes the research questions, scientific contribution and proposed approach of the research.

1.3.1 Research Questions

The following research questions are formulated consisting of a main question and four subquestions that align with the essential steps required to conduct the research. By answering the main research question and its subquestions, the aim is to develop a practical and efficient solution to the challenges outlined earlier.

Main Question:

What are the optimal component sizing, configuration and storage distribution of a low temperature district heating network using PVT and ATES to minimise grid exchange resulting in the lowest the CO2 emissions?

Subquestions:

- What effect has storage distribution and configuration of district heating and ATES have on the thermal performance?
- How does the size of the components influence the system's temperature stability throughout a year?
- How does the size of the components influence the system's generation capability and net grid exchange?
- What are the optimal component sizes to minimise CO2 emissions while ensuring system reliability and reduce grid power exchange?

1.3.2 Research gap

The aim of this work is to design, size and optimise a district heating system in residential areas with a case study in Hilversum, specifically targeting CO_2 emissions reduction. This involves a comprehensive analysis of how various component sizes and storage distribution influence power consumption from the grid to the electrical components, which in turn affects CO_2 emissions. With the application of 5GDHN, the methodology incorporates the use of PVT systems and ATES. The integration of PVT and ATES within 5GDHN frameworks is relatively novel, presenting various unexplored aspects. To establish a solid foundation on the existing knowledge on this combination, a literature search was conducted focusing on studies that utilise both PVT and ATES. The specific query used in the Scopus database was 'ATES OR "Aquifer Thermal Energy Storage" AND PVT OR "Photovoltaic Thermal",' which led to the identification of three studies.

Khlebnikova [13] explored the use of PVT in combination with 5GDHN, water-to-water heat pumps (HP), and ATES in Haarlem, Netherlands. This study focuses on the control strategy of the system. It considers a decentralised PVT system and emphasises on the control system within the household. Jansen [14] discusses the design of a sustainable urban energy system in Haarlem, aimed at creating an energy-neutral neighborhood. Considering multiple technologies and district heating networks, it results in a low-temperature heating network utilising decentralised PVT, HPs, and ATES. Apa and Picone [15] evaluate the performance of various ATES pilot sites across Europe, including a project in Delft that integrates ATES with PVT systems. This study provides valuable performance data and operational insights from different European contexts, adding depth to the analysis of ATES and PVT technologies in district heating networks.

The aforementioned studies utilise a combination of PVT and ATES, however with a different scope compared to this thesis. Both Khlebnikova [13] and Jansen [14] explore decentralised PVT installations on individual households, whereas this research focuses on a centralised PVT system installed on a carport. Additionally, all these papers employ differing methodologies and pursue different objectives. In contrast, this thesis aims to analyse the effects of distribution of the ATES, as well as the impact of different component sizes. It also includes a sizing optimisation method designed to minimise the CO_2 emissions from the district heating network. These aspects have not been addressed in the mentioned papers.

To design an optimal low-temperature district heating network utilising PVT and ATES, the initial step involves designing the topology of the network. This process includes evaluating two scenarios for locating the ATES, considering one with centralised ATES and another with distributed ATES. Significant research has explored the effects of distributed heat storage within district heating networks. Jebamalai [16] analyses the cost and efficiency implications of centralised versus distributed thermal storage within a thermal network, highlighting cost reductions associated with distributed storage configurations. Roder [17] developed an optimisation tool in Python using Mixed Integer Linear Programming (MILP) for low-temperature district heating networks, focusing on economic optimisation to reduce thermal losses and operational costs. Nuytten [18] examines a multi-carrier energy system, analysing the impact of centralised versus distributed thermal energy storage. The study notes that distributed storage reduces power supply flexibility for combined heat and power (CHP) systems, due to variability among storage tanks. While these studies are closely related in terms of thermal energy distribution, they focus on Thermal Energy Storage Systems (TESS) instead of ATES, which is the focus of this thesis.

The second step in the system's design involves sizing the components. This includes determining the optimal dimensions for the ATES system(s) and the quantity of PVT modules to be installed. Initially, the performance of various component sizes will be analysed for both centralised and distributed storage systems, focusing on heat generation and loss. Third, an optimisation method will be employed to adjust the sizes of the PVT modules and ATES, with the aim of minimising CO_2 emissions. This strategy seeks to derive an optimal design that enhances the system's autonomy. Previous research has made significant contributions to sizing optimisation in district heating networks using PVT. Geraedts [19] discusses the combination of PVT with 5GDHN and TESS, employing MILP for cost and environmental optimisation, focusing on sizing TESS. Krishna Priya [20] explores the optimal sizing of a PVT system in conjunction with thermal storage and load, focussing on cost-effectiveness. Testi [21] examines a PVT system combined with thermal storage for a residential building, including economic considerations in the sizing process.

1.3.3 Contribution

This thesis contributes by designing and optimising a district heating system in residential areas with a case study in Hilversum, specifically targeting CO2 emissions reduction. The primary scientific contributions, identified after addressing the research gap in Section 1.3.2, are as follows:

- Investigation on the effects of temperature and overall power consumption of distributed ATES.
- Analysis on the sizing effects of a centralised PVT installation in combination with ATES.
- Development of an available model for calculations on district heating networks including PVT, buildings, piping, ATES and heat pumps.

1.3.4 Approach

The tool for designing the heating network will be a Python model that includes the thermodynamic properties of all involved components. This model will integrate specific parameters from the Hilversum project, considering the physical constraints of the designated area. A critical element of this process is the precise estimation of the area's capabilities for electrical and thermal production, along with a detailed analysis of heat losses within the system. The sizing and configuration of the system will be guided by the environmental conditions and energy demands throughout the year. The ultimate objective is to create a system that is optimally sized and configured to ensure a balanced thermal energy flow across seasons, thereby achieving the lowest possible carbon footprint while maintaining efficiency.

The research will proceed in alignment with the outlined subquestions, beginning with an analysis of how different storage distribution and configurations of district heating and ATES affect thermal performance. Multiple cases will be constructed for this purpose: one utilising a single, centralised ATES unit in various configurations, and the other employing multiple, smaller, distributed ATES units. The distributed ATES units will be smaller in size but greater in number, totalling the same volume of water compared to the centralised ATES. The feasibility of installing these ATES units will be determined based on the capabilities of the existing area. This approach will enable a comprehensive assessment of thermal losses and the overall performance of the distribution scenario.

Second, the size of the PVT and ATES systems will be altered in different scenarios for both distributed and centralised ATES configurations. The influence of these changes on the system's generation capability and stability will be analysed. This will involve creating a feasible region of scenarios, each with specific dimensions, configurations, and ATES location, while considering the physical constraints of the project. These potential scenarios will then be used for the optimisation of the network.

Lastly, the optimal component sizes for the systems will be determined to ensure reliability and minimise CO2 emissions. These emissions will be directly linked to the electrical use and generation of the components resulting from the thermal behavior of the system. This electrical power flow results in power extracted from the grid to operate the system. An objective function will be created with minimal CO2 emissions as the target. The variables in this function will include the number of PVT modules and the sizes of the ATES units. The constraints will be based on the available area and the findings from the component size analysis.

2 Modelling

A model is constructed in Python to simulate the district heating network. This chapter describes the working principle of the model. It begins by outlining the fundamental physics within the model, starting with the thermodynamic principles of thermal components within the network. Then it explains the electrical equations that apply to the electrical components. Finally, the chapter discusses how these components are interconnected, detailing the inputs, time intervals, and control mechanisms that drive the simulation.

2.1 Thermal components

In the study of heating networks, understanding the thermodynamics of each component within the system is crucial for accurate modeling and simulation. To effectively represent the total system in a Python model, it is essential to first set up the thermodynamic equations specific to each component. This involves detailing the various heat flows associated with these components, including heat input, output, and losses within the system. By quantifying these thermal transactions, we can construct a comprehensive framework that allows for the integration of these components into a unified model. This approach not only facilitates the simulation of the network's overall performance but also enables the identification and optimisation of energy efficiency and loss minimisation strategies within the heating network.

2.1.1 Photovoltaic Thermal

In this section, the thermodynamic behavior and equations of PVT system is explained. Exploring how they respond to changes in irradiance and temperature, and the conversion of energy from the environment into heat. Setting up thermodynamic equations which can be used to model the whole system.

The PVT system in this case is a liquid based PVT module in contrast with air-based PVT modules, due to the connection with the fluid of the thermal network. A PVT system is a solar module able to generate electricity and thermal energy. The module consists of multiple layers: a glass top, an air gap, the PV, thermal absorber and thermal fluid tubes [4]. Each layer exchanges heat due to conduction, convection or radiation. Dependant on the position of the layer of the PVT, thermal exchange with another layer or the atmosphere needs to be expressed in the equations.

The method of expressing the thermodynamic behaviour is derived from [4], describing the heat transfer in each layer dependant on the adjacent layers or atmosphere. To simplify, the following assumptions are made:

- Edges are well insulated, no heat loss.
- The layers are very thin, so negligible vertical heat conduction.
- No dust or shading effects.
- The flow rate of the fluid is constant

The layers which are analysed are the glass, PV, thermal absorber and fluid. It is assumed that the temperatures of the air layer and thermal absorber are not relevant [4]. The thermal energy transfers through the layers and the atmosphere in the form of conduction, convection and radiation. Note that the PV layer consists of multiple layers itself: glass, two layers of EVA, the Si cell, Tedlar layer and an adhesive [7]. A cross section of the PVT collector layers is shown in Figure 5

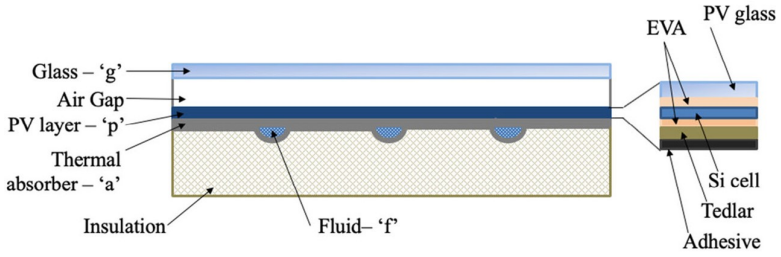

Figure 5: Cross section of the PVT collector [4].

The different heat transfer processes in the PVT are divided over the different layers. First, the glass layer receives solar irradiation, a part is reflected the rest is absorbed or transmitted to the PV layer. The glass layer receives reflected radiation and radiative losses from the PV layer. Thereby, it loses heat due to convection caused by wind. The PV layer receives solar radiation, of which some is reflected to the glass layer and some is absorbed. The radiation to the glass is heat loss from the PV layer. Convection between the PV and and the glass layer also takes place due to the air gap. Some of the irradiation absorbed by the PV layer is converted into electricity. The heat absorber layer exchanges heat with the PV layer, the insulation and the fluid through convection. The insulation loses heat to the environment trough convection from the wind. The heat transfer in the fluid in the tubes is also caused through convection by the pumping system [4]. All heat transfer processes are shown in Figure 6.

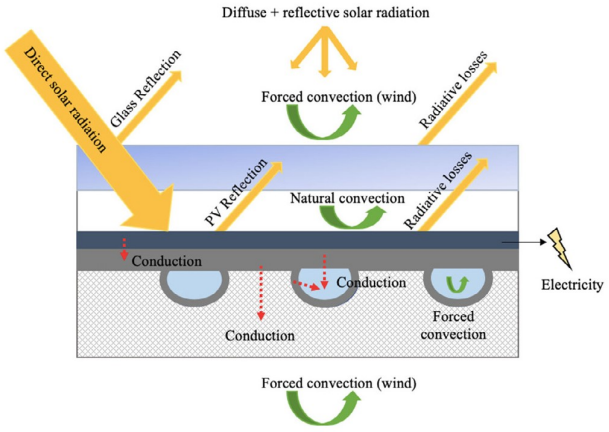

Figure 6: Schematic heat transfer processes in the layer of a PVT module [4].

To model these heat transfers through the different layers, the equation for the variation of internal energy in a physical body is used.

$$mc\frac{\Delta T}{\Delta t} = \dot{Q} \tag{1}$$

Then, the heat transfer $\dot{Q}$ can be expressed in different methods, dependant on the kind of heat transfer [4]. Convective and radiative heat transfer is expressed with the general equation

$$\dot{Q} = h_{\mathrm{i}} A_{\mathrm{i}} \frac{\Delta T}{\Delta t} \tag{2}$$

Heat absorbance due to irradiance can be expressed with [4]

$$\dot{Q} = A_{\mathrm{i}} \alpha_{\mathrm{i}} \frac{G}{\Delta t} \tag{3}$$

The equations for all different layers of the PVT module are expressed to obtain the temperature of the fluid transferring the heat into the heating distribution system. Using the method of [4] considering every different layer's heat transfer. The energy balance equations for the different layers are rearranged by isolating the temperatures of the glass layer, PV layer, thermal absorber layer and the fluid: T_{glass}, T_{PV}, T_a and T_{fluid}. This gives the following set of equations [7].

$$\begin{cases} T_{\text{glass}}\,(k+1) = C_1(k)T_{\text{glass}}\,(k) + C_2(k)T_{\text{PV}}(k) - D_1(k) \\ T_{\text{PV}}(k+1) = C_3(k)T_{\text{glass}}\,(k) + C_4(k)T_{\text{PV}}(k) + C_5(k)T_{\text{a}}(k) - D_2(k) \\ T_{\text{a}}(k+1) = C_6(k)T_{\text{PV}}(k) + C_7(k)T_{\text{a}}(k) + C_8(k)T_{\text{f}}(k) - D_3(k) \\ T_{\text{f}}(k+1) = C_9(k)T_{\text{a}}(k) + C_{10}(k)T_{\text{f}}(k) - D_4(k) \end{cases}, \tag{4}$$

$$C_1(k) = \frac{A_{\text{glass}}\Delta t}{m_{\text{glass}}c_{\text{glass}}}\left[\frac{m_{\text{glass}}c_{\text{glass}}}{A_{\text{glass}}\Delta t} - h^{\text{conv}}_{\text{glass}}(k) - h^{r}_{\text{glass}}(k) - h_{\text{gap}}(k) - h^{r}_{\text{glass-PV}}(k)\right] \tag{5}$$

$$C_2(k) = \frac{A_{\text{glass}}\Delta t}{m_{\text{glass}}c_{\text{glass}}}\left[h_{\text{gap}}(k) + h^{r}_{\text{glass-PV}}(k)\right] \tag{6}$$

$$C_3(k) = \frac{A_{\text{PV}}\Delta t}{m_{\text{PV}}c_{\text{PV}}}\left[h_{\text{gap}}(k) + h^{r}_{\text{glass-PV}}(k)\right] \tag{7}$$

$$C_4(k) = \frac{A_{\text{PV}}\Delta t}{m_{\text{PV}}c_{\text{PV}}}\left[\frac{m_{\text{PV}}c_{\text{PV}}}{A_{\text{PV}}\Delta t} - h_{\text{gap}}(k) - h^{r}_{\text{glass-PV}}(k) - h^{\text{cond}}_{\text{PV-a}}(k)\right] \tag{8}$$

$$C_5(k) = \frac{A_{\text{PV}}\Delta t}{m_{\text{PV}}c_{\text{PV}}}h^{\text{cond}}_{\text{PV-a}}(k) \tag{9}$$

$$C_6(k) = \frac{A_{\text{a}}\Delta t}{m_{\text{a}}c_{\text{a}}}h^{\text{cond}}_{\text{PV-a}}(k) \tag{10}$$

$$C_7(k) = \frac{\Delta t}{m_{\text{a}}c_{\text{a}}}\left[\frac{m_{\text{a}}c_{\text{a}}}{\Delta t} - h^{\text{cond}}_{\text{PV-a}}(k)A_{\text{a}} - h_{\text{a-f}}(k)A^{\text{abs}}_{\text{t}} - h^{\text{cond}}_{\text{a}}(k)A_{\text{a}}\right] \tag{11}$$

$$C_8(k) = \frac{\Delta t}{m_{\text{a}}c_{\text{a}}}h_{\text{a-f}}(k)A^{\text{abs}}_{\text{t}} \tag{12}$$

$$C_9(k) = \frac{A^{\text{abs}}_{\text{t}}\Delta t}{m_{\text{f}}c_{\text{f}}}h_{\text{a-f}}(k) \tag{13}$$

$$C_{10}(k) = \frac{\Delta t}{m_{\text{f}}c_{\text{f}}}\left[\frac{m_{\text{f}}c_{\text{f}}}{\Delta t} - h_{\text{a-f}}(k)A^{\text{surf}}_{\text{t}} - 2\dot{m}_{\text{f}}c_{\text{f}}\right] \tag{14}$$

$$D_1(k) = \frac{A_{\text{glass}}\Delta t}{m_{\text{glass}}c_{\text{glass}}}\left[h^{\text{conv}}_{\text{glass}}T_{\text{amb}}(k) + h^{r}_{\text{glass}}(k)T_{\text{sky}}(k) + \alpha_{\text{glass}}G(k)\right] \tag{15}$$

$$D_2(k) = \frac{A_{\text{PV}}\Delta t}{m_{\text{PV}}c_{\text{PV}}}\alpha_{\text{PV}}\tau_{\text{glass}}G(k)\left[1 - \eta_{\text{PV}}(k)\right] \tag{16}$$

$$D_3(k) = \frac{A_{\text{a}}\Delta t}{m_{\text{a}}c_{\text{a}}}h^{\text{cond}}_{\text{a}}(k)T_{\text{amb}}(k) \tag{17}$$

$$D_4(k) = 2\frac{\Delta t}{m_{\text{f}}}\dot{m}_{\text{f}}T^{\text{in}}_{\text{f}}(k) \tag{18}$$

The parameters of the equations are defined in the following way. $h^{\text{cond}}_{\text{i-j}}$ and $h^{\text{r}}_{\text{i-j}}$ are the conductive and radiative thermal coefficients from the i-th to the j-th layer, h_{i} and $h^{\text{conv}}_{\text{i}}$ are the total thermal coefficient and the convective thermal coefficient released into the environment for the i-th layer. A_{i} [m^2], m_{i} [kg], c_{i} [J/kg], L_{i} [m], α_{i} [-] and τ_{i} [-] are the area, mass, specific heat, thickness, absorbance and transmittance of the i-th layer. $\dot{m}_{\text{f}}$ is the mass flow of the fluid in the tube per time step. $A^{\text{abs}}_{\text{t}}$ [m^2] is the area of the tube which is in contact with the absorber, $A^{\text{surf}}_{\text{t}}$ [m^2] is the tube's lower surface area which is in contact with the isolation layer. G [Wm^{-2}] is the solar irradiation, T_{amb} is the ambient temperature and η_{PV} [-] is the PV electrical efficiency[7].

The difference in temperature over time is expressed discretely. $T_{\mathrm{i}}(k+1)$ is the temperature after time step Δt in using the previous temperature (one time step back) $T_{\mathrm{i}}(k)$. T_{sky} is the equivalent radiative temperature of the sky. There are multiple equations and methods to define the equivalent radiative temperature of the sky. In this case, the Brunt model is used [22].

$$T_{\mathrm{sky}}(k) = \left(0.62 + 0.056\left(6.11\left(\frac{RH}{100}\right)e^{\left(\frac{17.63T_{\mathrm{amb}}(k)}{243.04+T_{\mathrm{amb}}(k)}\right)}\right)^{0.5}\right)^{0.25} T_{\mathrm{amb}}(k) \tag{19}$$

Here, RH is the relative humidity. The thermal coefficients have to be calculated separately for each heat transfer expression between the layers. $h^{\mathrm{conv}}_{\mathrm{glass}}(k)$ can be calculated using the following equation

$$h^{\mathrm{conv}}_{\mathrm{glass}}(k) = \begin{cases} 5.7 + 3.8v_{\mathrm{w}}(k) & \forall v_{\mathrm{w}} \in [0,5] \text{ m/s} \\ 6.47 + v_{\mathrm{w}}^{0.78}(k) & \forall v_{\mathrm{w}} \in [5,10[\text{ m/s} \end{cases} \tag{20}$$

Where v_{w} is the wind speed. $h^{\mathrm{r}}_{\mathrm{glass}}(k)$ can be calculated using the following equation [4]

$$h^{\mathrm{r}}_{\mathrm{glass}}(k) = \varepsilon\sigma\left(T^2_{glass}(k-1) + T^2_{sky}(k)\right)\left(T_{glass}(k-1) + T_{sky}(k)\right) \tag{21}$$

Here, ε is the emissivity of the glass and σ is the Stefan-Boltzmann constant ($\sigma = 5.67{\times}10^{-8} Wm^{-2}$).
The thermal coefficient h_{gap} can be calculated using [4]:

$$\frac{1}{h_{gap}} = \frac{1}{h^{CV}_{glass-PV}} + \frac{L_{PVg}}{k_{PVg}} + \frac{L_{EVA}}{k_{EVA}} \tag{22}$$

Where, The L_i[m] is the thickness of the two top layers within the PV layer, the PV glass layer and the EVA layer. k_i[W/mK] is the thermal conductivity of the PV glass layer and the EVA layer. $h^{CV}_{glass-PV}$ is thermal coefficient of convective heat transfer between the glass and the PV layer and can be calculated with [4]:

$$h^{\mathrm{conv}}_{\text{glass-PV}}(k) = \frac{\mathrm{Nu}_{\mathrm{gap}}\, k_{\mathrm{gap}}}{L_{\mathrm{gap}}} \tag{23}$$

$\mathrm{Nu}_{\mathrm{gap}}$ is the Nusselt number for air within the gap. The radiative heat transfer coefficient between the glass and the PV layer is calculated with [4]:

$$h^{\mathrm{r}}_{\text{glass-PV}}(k) = \frac{1}{\frac{1}{\varepsilon_{\mathrm{glass}}} + \frac{1}{\varepsilon_{\mathrm{PV}}} - 1}\sigma\left(T^2_{\mathrm{glass}}(k-1) + T^2_{PV}(k-1)\right)\left(T_{\mathrm{glass}}(k-1) + T_{PV}(k-1)\right) \tag{24}$$

The conductive heat transfer coefficient through the layers of the PV to the thermal absorber, $h^{\mathrm{cond}}_{\mathrm{PV-a}}$ and the conductive heat transfer coefficient of the absorber to the environment $h^{\mathrm{cond}}_{\mathrm{a}}$ can be calculated with[4].

$$\frac{1}{h^{\mathrm{cond}}_{\mathrm{PV-a}}} = \frac{L_{EVA}}{k_{EVA}} + \frac{L_{Tedlar}}{k_{Tedlar}} + \frac{L_{Adhesive}}{k_{Adhesive}} \tag{25}$$

and

$$\frac{1}{h^{\mathrm{cond}}_{\mathrm{a}}} = \frac{L_a}{k_a} \tag{26}$$

The heat transfer coefficient of the fluid $h_{\mathrm{a-f}}$ depends on whether the flow in the tube is laminar or turbulent [4].

$$h_{\mathrm{a-f}}(k) = \begin{cases} 2\frac{k_{\mathrm{f}}}{D_{\mathrm{H}}} & \forall\, \mathrm{Re} = 0 \\ 4.36\frac{k_{\mathrm{f}}}{D_{\mathrm{H}}} & \forall\ 0 < \mathrm{Re} < 2300 \\ 0.023\frac{k_{\mathrm{f}}}{D_{\mathrm{H}}}\,\mathrm{Re}^{0.8}\,\mathrm{Pr}^{0.4} & \forall\, \mathrm{Re} \geq 2300 \end{cases} \tag{27}$$

Where D_{H} is the diameter of the tube and Re and Pr are the Reynolds and Prantl numbers of the fluid's flow. The fluid temperature in the tubes is considered the average of the temperature in and temperature out

$$T_{\mathrm{f}}(k) = \frac{T^{\mathrm{in}}_{\mathrm{f}}(k) + T^{\mathrm{out}}_{\mathrm{f}}(k)}{2} \tag{28}$$

The electrical efficiency of the PV η_{PV} is dependant on on the temperature of the PV, it is calculated using:

$$\eta_{\mathrm{PV}}(k) = \eta_{\mathrm{PV}}^{\mathrm{STC}} \left(1 - \beta_{\mathrm{PV}} \left(T_{\mathrm{PV}}(k) - T_{\mathrm{ref}}\right)\right) \tag{29}$$

Where $\eta_{\mathrm{PV}}^{\mathrm{STC}}$ is the electrical efficiency of the PV under standard test conditions (irradiance = 1000 Wm^{-2}, T = 25 °C, AM = 1.5). T_{ref} is the temperature under the standard test conditions and β_{PV} is the temperature coefficient of the PV.

Finally, the heat output of the PVT modules can be calculated using the temperature of the fluid in the tubes [7].

$$\dot{Q}_{\mathrm{PVT}}(k) = \eta_{\mathrm{T}} N \dot{m}_{\mathrm{f}} c_{\mathrm{f}} \left(T_{\mathrm{f}}^{\mathrm{out}}(k) - T_{\mathrm{f}}^{\mathrm{in}}(k)\right) = 2\eta_{\mathrm{T}} N \dot{m}_{\mathrm{f}} c_{\mathrm{f}} \left(T_{\mathrm{f}}(k) - T_{\mathrm{f}}^{\mathrm{in}}(k)\right) \tag{30}$$

Where η_{T} is the efficiency of the heat exchanger from the PVT to the heating network and N is the number of tubes in the PVT.

2.1.2 Aquifer Thermal Energy Storage

For the ATES, an underground water-bearing layer (aquifer) is utilised for thermal energy storage. The ATES system is employed for addressing the residential heating demand in winter and cooling demand in summer, serving as a flexible solution for thermal energy management throughout the year. This system adopts a doublet ATES configuration, wherein the cooling and heating wells are installed in separate boreholes. To prevent interference between the two, a specific horizontal distance is carefully maintained. During winter, water is cooled by the thermal demand of the building and then directed into the cold well after its use. Conversely, in the summer, the water heated by the building's cooling requirements is stored in the warm water well, ready for use in the following winter. This cyclical process facilitates an efficient use of underground thermal energy, contributing to the sustainability and energy efficiency of residential heating and cooling systems.

Due to the significantly smaller height of the aquifer compared with the area, the aquifer's heat losses are attributed exclusively to thermal diffusion towards the overburden and underburden layers [11]. It is assumed that the applicable temperature in the ground surrounding an ATES system is constant and not dependent on the environment. It is observed that at a certain depth—typically between 4 to 6 meters—the ground temperature becomes relatively constant and remains unaffected by annual environmental changes [23], but is solely dependant on geothermal energy. This principle holds true in the Netherlands, where ATES systems are usually installed at depths ranging from 20 m to 150 m, a range considered relatively shallow yet sufficiently deep to negate environmental influences [12]. Measurements in Hilversum indicate a stable temperature of 11°C at both 25 m and 125 m depths [24], suggesting no significant temperature variation occurs within this subsurface span.

In the context of the Hilversum ATES, the depth of the wells demonstrates a similarity. The aquifer under Hilversum is positioned between two impermeable layers, consisting of clay and fine sand, which prevents water from permeating through them. This aquifer stretches to depths varying from approximately 45 m to 65 m and extends further to around 148 m to 170 m. Due to the presence of oxic pollution water at shallower depths, a minimum operational depth of 110 m is maintained for the aquifer's use [25]. Consequently, the operational depth range for the well in this aquifer lies between 110 m and 170 m. Based on this setup, it is assumed that the temperature within this specified depth range remains constant at 11°C, aligning with the observed stable temperature characteristics at similar depths within the region.

The aquifer's heat balance comprises the heat supplied by the water inlet, the heat withdrawn by the water outlet, and heat losses to the surrounding overburden and underburden geological formations. The ATES is an open system, so the input and output heat is expressed as the the flow of warm water.

$$\dot{m}_{\mathrm{in}} c_f T_{\mathrm{in}}(k) - \dot{m}_{\mathrm{out}} c_f T_{\mathrm{ATES}}(k) - \dot{Q}_{\mathrm{soil}}(k) = \sum_{i=1}^{n} m_i c_i \frac{\Delta T_{\mathrm{ATES}}}{\Delta t} \tag{31}$$

Where $\dot{m}_{\mathrm{in}}$ is the mass flow into the ATES, with temperature T^{in}. $\dot{m}_{\mathrm{in}}$ is the mass flow from the ATES, with temperature T_{ATES}. $\dot{Q}_{\mathrm{soil}}$ is the heat exchange with surrounding underground layers. m_i and c_i are the mass and specific heat of the aquifer material. The aquifer is assumed to consist of water and rock, thus the internal heat is dependant on the ratio of these materials, thus [11].

$$\sum_{i=1}^{n} m_i c_i = (1-n) m_r c_r + n m_f c_f \tag{32}$$

Where n is the porosity of the aquifer, m_r and m_f the mass of the rock and water, c_r and c_f the heat capacity of rock and water. The temperature within the ATES can be modeled using the following equation, under the assumption that the aquifer behaves like a perfectly mixed water tank.

$$T_{\text{ATES}}(k+1) = T_{\text{ATES}}(k) + \frac{\Delta t[\dot{m}_{\text{in}} c_f T_{\text{in}}(k) - \dot{m}_{\text{out}} c_f T_{\text{ATES}}(k) - \dot{Q}_{\text{soil}}(k)]}{(1-n) m_r c_r + n m_f c_f} \tag{33}$$

The total heat loss to the ground can be split up into heat loss into the overburden and underburden layers.

$$\dot{Q}_{\text{soil}} = \dot{Q}_{\text{overburden}} + \dot{Q}_{\text{underburden}} \tag{34}$$

Equation 2 can be specified to the conductive heat transfer from the aquifer into the overburden and underburden layers.

$$\dot{Q}_{\text{overburden}} = h^{cond}_{\text{ATE}-\text{o}} A_{\text{top}} [T_{\text{ATE}}(k) - T_{\text{overburden}}] \tag{35}$$

$$\dot{Q}_{\text{underburden}} = h^{cond}_{\text{ATE}-\text{u}} A_{\text{bottom}} [T_{\text{ATE}}(k) - T_{\text{underburden}}] \tag{36}$$

Where $h^{cond}_{\text{ATE}-\text{o}}$ and $h^{cond}_{\text{ATE}-\text{u}}$ can be calculated with the method of Equation 26.

2.1.3 Heat pumps

This section outlines the energy conversion characteristics of heat pump systems, which are installed in each building to supply the heat to match demand. Water-to-water heat pumps are used, where the heat pump extracts thermal energy from a water supply. Figure 7 provides a schematic overview of the heating cycle of the heat pumps, illustrating the temperatures and heat transfers involved.

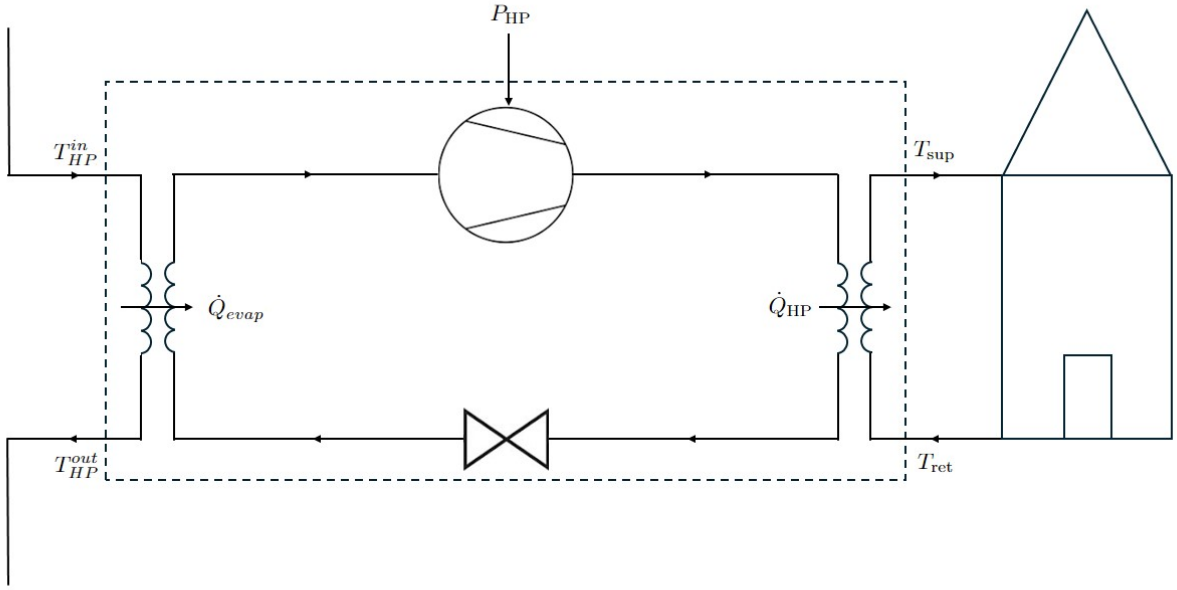

Figure 7: Schematic overview of the heat pump cycle.

Heat pumps convert heat and electrical energy into the thermal heat supply through a reversed refrigeration cycle. To determine the amount of power necessary to meet heating demand, the coefficient of performance is calculated with

$$\mathrm{COP}(k) = 7.90471e^{-0.024(T_{\mathrm{ret}}(k)-T_{in}(k))} \tag{37}$$

The constants where established by regression of 10 different heat pump models by [26]. Here, T_{ret} is the return temperature of the fluid at the inlet of the heat pump which is cooled by the thermal demand of the building and T_{in} is inlet temperature of the district heating into the heat pump. The COP is the coefficient of performance. This coefficient is the relation for the conversion of electrical power consumption into heat supply [7].

$$P_{\mathrm{HP}}(k) = \frac{\dot{Q}_{\mathrm{HP}}(k)}{\mathrm{COP}(k)} \tag{38}$$

The practical COP of a heat pump is typically different from the theoretical value due to various real-world factors affecting efficiency. To prevent unrealistic values, a maximum COP is used. The heat pump uses R32 refrigerant [27], which, according to studies, has a maximum COP of 3.6 for water-to-water systems [28].

The heat which the heat pumps use to evaporate the refrigerant is extracted form the water in the district heating network. This extracted heat can be calculated with the following Equation [29].

$$\dot{Q}_{evap}(k) = \dot{Q}_{HP}(k)\left(1 - \frac{1}{\mathrm{COP}(k)}\right) \tag{39}$$

The heat supply of the heat pumps can be expressed using a similar method as Equation 30, namely

$$\dot{Q}_{\mathrm{HP}}(k) = \eta_{\mathrm{HP}}\dot{m}_f c_f \left(T_{\mathrm{sup}} - T_{\mathrm{ret}}(k)\right) \tag{40}$$

Where the heat supply of the heat pump $\dot{Q}_{\mathrm{HP}}$ is expressed using the fluid's mass flow $\dot{m}_f$ from and to the building, the heat pump's efficiency η_{HP} and the specific heat of the fluid c_f. T_{sup} is the required supply temperature of the fluid which will be at the inlet of the building. This temperature is fixed to remain a constant temperature in the buildings' boiler.

2.1.4 District Heating

This section describes the thermodynamic effects when transporting heat in the form of warm water through underground pipes. These pipes form the heat distribution system, transporting the heat from the PVT modules and ATE storage to the heat demanding buildings.

To accurately assess the heat losses in the pipe, a temperature profile is established that delineates how temperature varies along the pipe's length. This pipe, which is embedded underground, principally dissipates heat to the surrounding soil. Given that the pipe's temperature fluctuates along its length, the rate of heat transfer to the soil also varies correspondingly. To model this phenomenon, the following equations are introduced, employing dx to represent an infinitesimally small segment of the pipe:

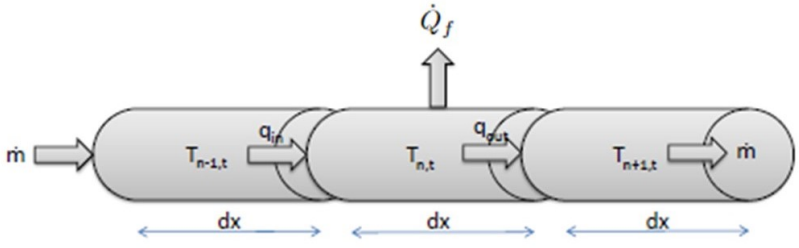

Figure 8: An infinitesimal section of a pipe [30].

$$\dot{m}_f c_f dT_f = \dot{Q}_f = \dot{m}_f c_f \left(T_{\mathrm{f}}^{\mathrm{x}}(k) - T_{\mathrm{f}}^{\mathrm{x+dx}}(k)\right) \tag{41}$$

$$\dot{Q}_f = \frac{(T_{\mathrm{f}}^{\mathrm{x}}(k) - T_{\mathrm{s}}(k)))dx}{R_t} \tag{42}$$

Where $\dot{m}_f$ and c_f are the mass flow and specific heat of the fluid in the pipes. $T_{\mathrm{f}}^{\mathrm{x}}$ is the temperature of the fluid at the inlet of pipe segment with length dx, and $T_{\mathrm{f}}^{\mathrm{x+dx}}$ is the outlet temperature of the segment. R_t is the total thermal resistance from the fluid to the grounds' surface. The length of the small segment of the pipe is dx and T_s is the temperature at the ground's surface.

In the analysis of heat transfer within the pipe system, a differential approach is employed to quantify the variation in heat exchange along the pipe's length, accounting for the changing temperature of the fluid inside the pipe as it loses heat to the surrounding soil. This method involves setting up an integral equation, where integration with respect to the fluid temperature change dT_f on the left-hand side is done, representing the thermal energy variation within the pipe, and with respect to the pipe segment length dx on the right-hand side, denoting the spatial progression along the pipe. When Equations 41 and 42 are combined, the following equation is formed [31].

$$\frac{dT_f}{T_{\mathrm{f}}^{\mathrm{x}}(k) - T_{\mathrm{s}}(k)} = \frac{dx}{\dot{m}_f c_f R_t} \tag{43}$$

The integration boundaries are defined by the inlet and outlet fluid temperatures for the left-hand side, and the start and end points of the pipe's length for the right-hand side. This approach yields a comprehensive model that captures the dynamics of heat loss across the pipe, facilitating a precise determination of how the fluid temperature evolves from the point of entry to the point of exit [32].

$$\int_{T_{in}}^{T_{out}} \frac{dT_f}{T_{\mathrm{f}}^{\mathrm{x}}(k) - T_{\mathrm{s}}(k)} = \int_0^L \frac{1}{\dot{m}_f c_f R_t}\, dx \tag{44}$$

After integration, Equation 45 is established. A constant temperature over the area is assumed due to negligible district heating influence on ground surface temperature [33].

$$\frac{T_{\mathrm{s}}(k) - T_f^{out}(k)}{T_{\mathrm{s}}(k) - T_f^{in}(k)} = e^{-\frac{L}{\dot{m}_f c_f R_t}} \tag{45}$$

And isolating T_f^{out} gives the following equation.

$$T_f^{out}(k) = T_{\mathrm{s}}(k) - \left(T_{\mathrm{s}}(k) - T_f^{in}(k)\right) e^{-\frac{L}{\dot{m}_f c_f R_t}} \tag{46}$$

Where T_f^{out} is the outlet temperature and T_f^{in} is the inlet temperature of the pipe, L is the length of the pipe. The total thermal resistance R_t is a combination of the conductive and convective heat transfer coefficients from the fluid to the ground.

To calculate the temperature at the grounds' surface, a method to model a temperature gradient over a depth y is used [7]. For modeling heat loss to the ground, the temperature at any specific depth y is assumed to be constant over the total area. To calculate the soil temperature, the system is represented as a semi-infinite solid along one-dimensional coordinates, [7] used this method for a standard thermal energy storage system. The boundary conditions for the model are surface temperature and the temperature at a point underground with a constant temperature. The first boundary, the surface temperature, can be obtained using Fourier's Conductivity Law, Newton's Law of Cooling, and Stefan-Boltzmann's Law of Radiation [7].

$$-k_{\mathrm{soil}} \frac{\Delta T_{\mathrm{soil}}(y,k)}{\Delta y} = h(k)\left[T_{\mathrm{amb}}(k) - T_{\mathrm{s}}(k)\right] - \epsilon \Delta R(k) + \alpha_0 G(k) \tag{47}$$

Where $T_{\mathrm{s}}(y=0)$ is the temperature of the soil at the surface, k_{soil} is the thermal conductivity of the soil. ϵ is the thermal emissivity of the soil, α_0 is the soil's absorbtivity and G is the solar radiation. T_{amb} is the ambient temperature. ΔR is given with the following equation:

$$\Delta R\left(k\right)=\sigma\left[T_{\mathrm{s}}^{4}\left(k-1\right)-T_{\mathrm{sky}}^{4}\left(k\right)\right] \tag{48}$$

Here, T_{sky} can be calculated using Equation 19 and $T_{\mathrm{s}}\left(k-1\right)$ is the surface temperature ate the previous time step. The total heat transfer coefficient h is a combination of the convective and radiative heat transfer coefficients:

$$h\left(k\right)=h^{\mathrm{conv}}\left(k\right)+h^{r}\left(k\right) \tag{49}$$

The convective heat transfer coefficient h^{conv} is calculated with Equation 20 and radiative heat transfer coefficient h^{r} is calculated with:

$$h^{r}\left(k\right)=\epsilon\sigma\left[T_{\mathrm{s}}^{2}\left(k-1\right)+T_{sky}^{2}\left(k\right)\right]\left[T_{\mathrm{s}}\left(k-1\right)+T_{sky}\left(k\right)\right] \tag{50}$$

Making the assumption that the temperature profile over y within the soil is linear, the following equation can be used.

$$-k_{\mathrm{soil}}\frac{\Delta T_{\mathrm{soil}}\left(y,k\right)}{\Delta y}=-k_{\mathrm{soil}}\frac{T_{\mathrm{d}}-T_{\mathrm{s}}}{d} \tag{51}$$

Where d is the distance of the surface to the a point underground where the environmental effects are neglectable, this is considered at a depth of 6 meters [23]. This temperature can be calculated with the following equation:

$$T_{\mathrm{d}}=0.0318d+8.01768 \tag{52}$$

Combining Equation 47 and 51 allows to obtain the expression for the temperature at the surface.

$$T_{\mathrm{s}}(k)=\frac{k_{\mathrm{soil}}T_{\mathrm{d}}+dhT_{\mathrm{amb}}\left(k\right)-d\varepsilon\Delta R\left(k\right)+d\alpha_{o}G\left(k\right)}{dh+k_{\mathrm{soil}}} \tag{53}$$

To quantify the heat loss to the ground, a theory from Wallenten [34] is applied, which focuses on the heat conduction dynamics of an insulated pipe embedded in the ground. The situation is shown in Figure 9.

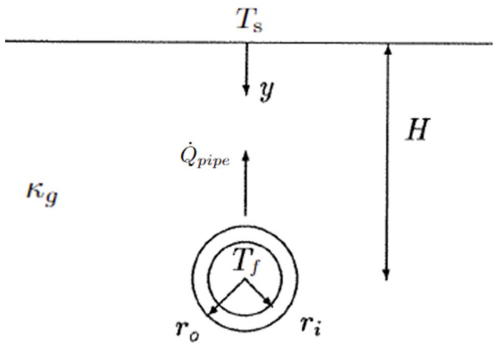

Figure 9: One pipe in the ground [34].

The conductive heat transfer resistance of the pipe $h_{\mathrm{f-s}}^{\mathrm{cond}}$ can be calculated using [34] with equation.

$$\frac{1}{h_{\mathrm{f-s}}^{\mathrm{cond}}}=\ln\left(\frac{2H}{r_{o}}\right)+\beta \tag{54}$$

The distance between the center of the pipe and the ground is H. The thickness of the insulation of the pipe is expressed with an inside radius r_i and outside radius r_o. The dimensionless parameter β is expressed with the following equation. The error, using this formula for $h_{\mathrm{p-g}}^{\mathrm{cond}}$, is typically less than 0.5% [34].

$$\beta = \frac{\kappa_g}{\kappa_t} \ln\left(\frac{r_o}{r_i}\right) \tag{55}$$

The thermal conductivity of the tube is κ_t and the thermal conductivity of the ground is κ_g. This equation is designed for a single-layer tube embedded in the ground. However, the district heating network employs a pipe that features an inner tube encased by an additional layer of insulation. Therefore, the dimensionless parameter needs to be adapted to accommodate this multi-layered structure as follows.

$$\beta = \frac{\kappa_g}{\kappa_t} \ln\left(\frac{r_{i-o}}{r_i}\right) + \frac{\kappa_g}{\kappa_i} \ln\left(\frac{r_o}{r_{i-o}}\right) \tag{56}$$

The thermal conductivity of the insulation is κ_i and r_{i-o} is the outer diameter of the tube which is the inner diameter of the insulation. The total heat transfer coefficient can be translated to a total heat resistance to simplify.

$$R_t = R_{cond} + R_{conv} \tag{57}$$

$$R_{cond} = \frac{\ln\left(\frac{2H}{r_o}\right)}{2\pi\kappa_g} + \frac{\ln\left(\frac{r_{i-o}}{r_i}\right)}{2\pi\kappa_t} + \frac{\ln\left(\frac{r_o}{r_{i-o}}\right)}{2\pi\kappa_i} \tag{58}$$

R_{conv} can be calculated using Equation 27, where the resistance is the inverse of the thermal convective coefficient. Finally, the total heat loss of the pipe can be calculated using the inlet and outlet temperature of the fluid in the pipe.

$$\dot{Q}_{pipe} = \dot{m}_{\mathrm{f}} c_{\mathrm{f}} \left(T_{\mathrm{f}}^{\mathrm{out}}(k) - T_{\mathrm{f}}^{\mathrm{in}}(k)\right) \tag{59}$$

2.1.5 Thermal Demand

The thermal demand for buildings primarily stems from the need to maintain a consistent indoor temperature which is set on a thermostat. Heat losses to the environment result in a temperature decline within these buildings. To counteract this effect and keep the temperature stable, it is necessary to supply an amount of heat equivalent to the thermal losses. This is done using an indoor boiler which is kept at a constant temperature, where heat can be extracted from to maintain a desired indoor temperature. Given the Netherlands' relatively low temperatures, the focus is primarily on meeting the heating requirements.

A similar approach for modelling the buildings is used in [7]. The buildings are considered with losses to the environment through walls, double-glass windows and the roof. Assuming no mass exchange between the exterior and interior of the house, the internal energy of the building can be calculated with.

$$\frac{\Delta T}{\Delta t} \sum_{i=1}^{n} m_i c_i = \sum_{i=1}^{n} \dot{Q}_i \tag{60}$$

Considering a single input of heat into the building and considering a heat demand equivalent to the heat losses, the equation can be rewritten as

$$\frac{\Delta T_{\text{in}}}{\Delta t} \sum_{i=1}^{n} m_i c_i = \dot{Q}_{in} - \dot{Q}_{\text{D}} \tag{61}$$

Each building is heated by its own individual heat pump. The pump supplies a constant temperature supply into the building T_{sup}, to remain a constant temperature of the indoor boiler equal to the supply temperature. Isolating the indoor temperature gives the following equation, where the heat inserted to the building is provided by the heat pump. Where ΔT_{in} is the change in temperature during time step Δt.

$$T_{\text{in}}\left(k+1\right) = T_{\text{in}}\left(k\right) + \frac{\Delta t(\dot{Q}_{HP} - \dot{Q}_{\text{D}})}{\sum_{i=1}^{n} m_i c_i} \tag{62}$$

For the analysis of building heat loss, the building is conceptualised as one space with its thermal mass and losses to the external environment. Heat transfers to the ground and radiative heat transfers are not considered in this model. The heat loss from the building primarily results from the unique characteristics of the walls, windows, and roof that interface with the environment. These losses are conductive and convective heat transfers and additionally ventilation and air infiltration losses, using a method described by [7], the convective losses are modeled by dividing them into two identical sections, each spanning half the original distance, with the thermal mass positioned in between. The overall heat transfer coefficient, which quantifies these losses, is shown in Figure 10 and can be calculated using the following equation:

$$U = \left(\sum_{i=1}^{n} \frac{1}{h_i} + \sum_{i=1}^{m} \frac{L_i}{k_i} \right)^{-1} \tag{63}$$

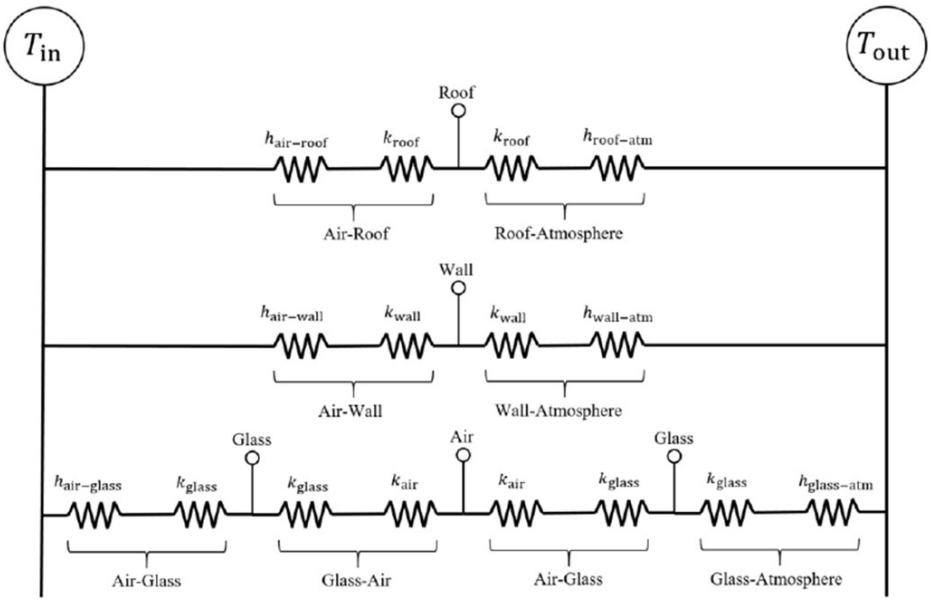

Figure 10: Convective and conductive thermal losses through the roof, walls, and windows considered per house room [7].

Where h_i are the convective heat transfer coefficients, k_i is the materials' conductivity and L_i the thickness of the conductive materials. Using this heat transfer coefficient, the heat losses from the building through conduction and convection can be determined as follows:

$$\dot{Q}_{\mathrm{L}} = \sum_{i=1}^{n} U_i A_i \Delta T \tag{64}$$

Here, A_i are the surface areas with the corresponding heat transfer coefficients, and ΔT denotes the temperature difference between the indoor and outdoor environments.

The ventilation and infiltration heat exchange can be calculated through a method provided by [7] and [32]. This heat exchange results from the mass exchange of air entering and exiting the house. The process can be divided into two parts: intentional ventilation and incidental infiltration. Firstly, ventilation heat exchange is described as:

$$\dot{Q}_{\mathrm{v}} = c_a \rho_a q_v \Delta T \tag{65}$$

Where, c_a and ρ_a are the specific heat capacity and density of air, ΔT is the temperature difference between the outside and inside of the building. The ventilation airflow, denoted as q_v can be calculated using the following equation:

$$q_v = 0.03 A_{\mathrm{cf}} + 7.5\,(N_{\mathrm{br}} + 1) \tag{66}$$

Here, A_{cf} is the conditioned area of the building and N_{br} is the number of bedrooms. Next, the infiltration heat exchange is described in a similar way:

$$\dot{Q}_{\mathrm{i}} = c_a \rho_a q_i \Delta T \tag{67}$$

Where the infiltration airflow, denoted as q_v can be calculated using the following equation:

$$q_i = A_{\mathrm{ex}} A_l \sqrt{C_s \left|\Delta T\,(k)\right| + C_w u^2} \tag{68}$$

The exposed area is represented as A_{es} and the leakage area as A_l. The stacking coefficient C_s depends on the number of floors, while the wind coefficient C_w depends on the building's surroundings [32].

The total heat demand of the buildings is the sum of the losses due to conduction and convection, ventilation losses, and infiltration losses.

$$\dot{Q}_D = \dot{Q}_{\text{L}} + \dot{Q}_{\text{v}} + \dot{Q}_{\text{i}} \tag{69}$$

2.2 Electrical components

This section examines the system's electrical components to be implemented in the model. This includes PV modules within the PVT that generate electricity. Additionally, the electricity demand from heat pumps is included, which is influenced by the buildings' thermal needs. The electrical demand of the buildings is also approximated to include the total power consumption. Additionally, the electrical demand for hydraulic pumps used in the ATES system is accounted for. The model also includes a grid connection to distribute excess electricity or supplement shortages from the PV system, ensuring a consistent power supply to all electrical components.

The power balance is shaped by the electricity from PV modules, the power demand from heat pumps, electrical load of the buildings and ATES hydraulic pump. This setup defines the grid interactions, and can be expressed with the following.

$$P_{\mathrm{G}} = P_{\mathrm{PV}} - \sum_{i=1}^{n} P_{\mathrm{HP,i}} - P_{\mathrm{Load}} - P_{\mathrm{ATES}} \tag{70}$$

2.2.1 Photovoltaic

The thermal properties of the PVT system were discussed in section 2.1.1. This includes the temperature for all different layers of the PVT system. The electrical properties of the PV is dependant on the temperature of the PV layer, this temperature can be calculated using the PVT model. The efficiency of the PV can be calculated using:

$$\eta_{\mathrm{PV}}(k) = \eta_{\mathrm{PV}}^{\mathrm{STC}} \left(1 - \beta_{\mathrm{PV}} \left(T_{\mathrm{PV}}(k) - T_{\mathrm{ref}}\right)\right) \tag{71}$$

where $\eta_{\mathrm{PV}}^{\mathrm{STC}}$ is the electrical efficiency of the PV under standard test conditions (irradiance = 1000 Wm^{-2}, T = 25C°, AM = 1.5). T_{ref} is the temperature under the standard test conditions and β_{PV} is the temperature coefficient of the PV. The electrical power produced by the PV can be calculated with [7]:

$$P_{\mathrm{PV}}(k) = \eta_{\mathrm{PV}}(k)\, A_{\mathrm{PV}} G(k) \tag{72}$$

where A_{PV} represents the surface area of the photovoltaic (PV) modules, and G denotes the solar irradiance received by the PV surface.

2.2.2 Heat Pumps

The electrical properties of the heat pump are among other aspects explained in section 2.1.3 using:

$$\mathrm{COP}(k) = 7.90471 e^{-0.024(T_{\mathrm{ret}}(k) - T_{in}(k))} \tag{73}$$

$$P_{\mathrm{HP}}(k) = \frac{\dot{Q}_{\mathrm{HP}}(k)}{\mathrm{COP}(k)} \tag{74}$$

The power for the heat pumps is primarily sourced from PV modules, with electricity from the grid being a secondary option. For simplicity, the grid is assumed to be an infinite energy source, allowing for unlimited energy extraction as needed. However, since grid electricity is the only component potentially linked to fossil fuel consumption, CO_2 emissions from the system are directly tied to the heat pumps' reliance on the grid. Minimising this dependency, therefore, is a key focus of the research to ensure both system viability and reduced CO_2 emissions.

2.2.3 Electrical Demand

To approximate the electrical demand for all buildings, the total predicted power usage of the buildings is used [35]. A synthetic load profile generated for the number of houses, as described in [36], is then applied. This profile is scaled based on the difference between the total power used in the initial profile and the predicted total power consumed in the buildings. The total building load is denoted as P_{Load} in Equation 70.

2.2.4 ATES Hydraulic Pumps

Water extraction and injection into aquifers for ATES systems require the installation of pumps for each ATES well. These pumps consume electricity, similar to the operation of heat pumps within the system. Primarily, the electricity needed to power these hydraulic pumps is sourced from PV modules, with grid electricity serving as a secondary source. The power consumption of these hydraulic pumps can be calculated using the following equation [32]. Considering a constant pump efficiency and constant volume flow of water.

$$P_{\text{ATES}} = \frac{\dot{V}(\rho g h + L p_L)}{\eta_{\text{ATES}}} \tag{75}$$

Where $\dot{V}$ represents the volume flow rate of water, with ρ, g, and h, denoting the density of water, the gravitational constant, and the vertical distance traversed. L signifies the length of the underground pipe, while η_{ATEP} is the efficiency of the pump. The unit p_L represents the pressure loss per unit length within the pipe, this can be calculated using the following equation.

$$p_L = \frac{64}{Re}\left(\frac{L}{\mathrm{d}}\right)\left(\frac{\rho_f V^2}{2}\right) \tag{76}$$

Here, Re is the Reynolds number of the fluids' flow and V is the velocity. The length of the tube is L and the diameter is d.

2.3 Component connection

The district heating network is constructed in the Python model by linking together the components: PVT, ATES, HP, pipes, and buildings. Data on ambient temperature, irradiance, and electrical load is implemented at 15-minute intervals, using weather conditions provided by the KNMI [37]. The desired indoor temperature 20°C during the day and 17°C at night. The model calculates the temperatures and heat exchange within the system at each 15-minute interval. Based on the thermal state at each time step, the components' response is determined. The next chapter will detail the configuration and connections of these components within the model.

2.3.1 Thermal Network

The components will include PVT, ATES, HP, pipes, and buildings, all connected to analyse the performance of the thermal network. The entry and exit temperature points for each component form the basis of the systems' dynamics. Here, the outlet temperature for one component is assumed becoming the inlet temperature for the other in a sequential manner. The temperature differences in each component due to the exchange of heat can be determined mathematically using the equations from Section 2.1.

The system's initial setup features a centralised configuration of a PVT and ATES system. All components are interconnected through pipes except for the heat pumps to the corresponding buildings. This network is designed in such a way that it is a closed loop, and the carrier thermal fluid circulates clockwise through all the heat pumps once it has passed through the PVT and the ATES system. The thermal connection to the heat pumps, buildings and PVT are done through a heat exchanger. On the other hand, for the ATES and pipes, the components are directly connected to the thermal carrier. The schematic overview of the system can be seen in Figure 11. The number of buildings with heat pumps is in reality higher, and is therefore expressed as the ith building, heat pump or pipe.

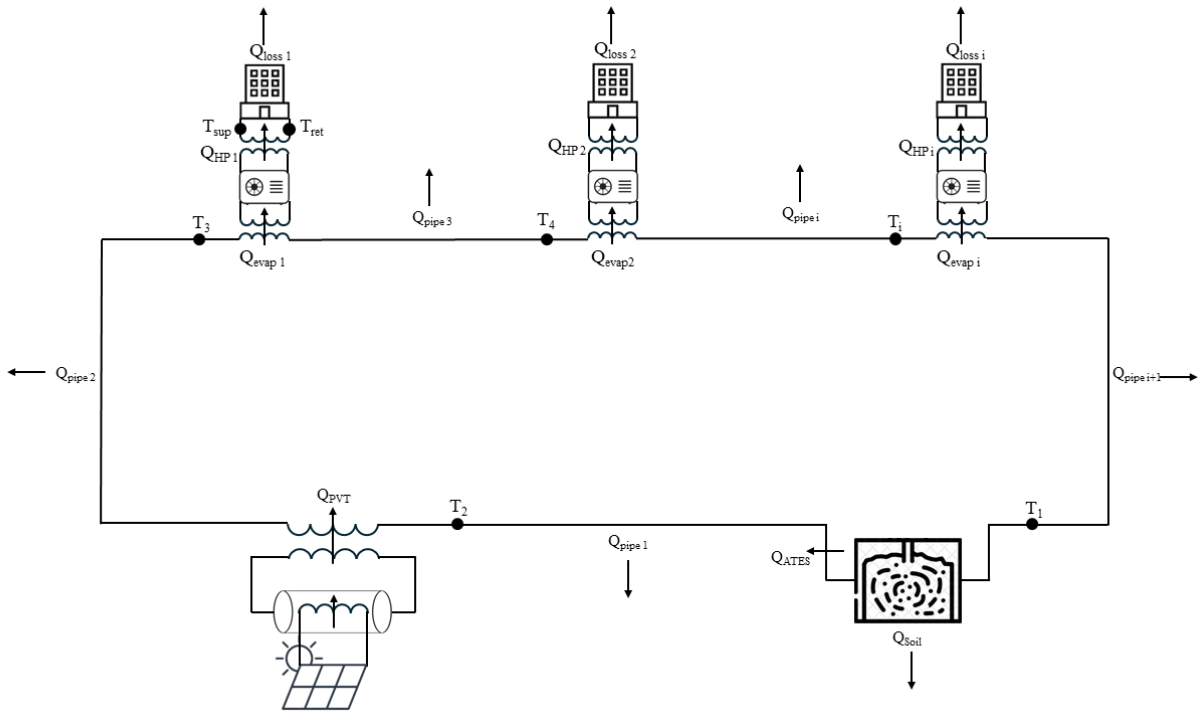

Figure 11: Thermal network configuration

The temperatures at the different points in the thermal network are calculated using the previous temperature and the characteristic heat exchange of the component. Due to multiple buildings with corresponding heat pumps and pipes connecting them, a set of equations is formed for each ith combination of these components. The temperatures of the connection between the buildings and the heat pumps can be calculated using Equation 40.

$$\dot{Q}_{\text{building}} = \frac{\sum_{i=1}^{n} m_i c_i \cdot (T_{\text{in}}(k-1) - T_{\text{in}}(k-2))}{\Delta t} - \dot{Q}_{\text{D}} \tag{77}$$

$$T_{\text{sup}}(k) = T_{\text{ret}}(k-1) + \frac{\dot{Q}_{\text{building}}(k)}{\dot{m}_{fb} c_f} \tag{78}$$

$$T_{\text{ret}}(k) = T_{\text{ret}}(k-1) + \frac{\dot{Q}_{building}(k-1) + \dot{Q}_{\text{HP}}(k-1)}{\dot{m}_{fb} c_f} \tag{79}$$

Where the T_{sup} is the supply temperature into the building which is heated up to 53°C when the T_{ret} out of the building drops below 50°C, T_{in} is the inside temperature of the building. The water mass flow in and out of the building is $\dot{m}_{fb}$. The following equations connect the heat pumps with its subsequent pipe.

$$T^{out}_{HP,i}(k) = T^{in}_{HP,i}\,(k-1) - \frac{Q_{\text{evap,i}}(k)}{\dot{m}_f c_f}, \tag{80}$$

$$T^{out}_{pipe,i}(k) = T^{in}_{HP,i}\,(k-1) - \frac{\dot{Q}_{evap,i}(k) + \dot{Q}_{pipe,i}(k-1)}{\dot{m}_f c_f}, \tag{81}$$

$$T^{in}_{HP,i+1}(k) = T^{out}_{pipe,i}(k) \tag{82}$$

Considering a centralised PVT and ATES, the following equations express the total systems' thermodynamics. Using the sum of all heat pumps and pipes, which remove heat from the system.

$$T^{out}_{PVT}(k) = T^{in}_{ATES}\,(k-1) - \frac{\sum_{i=1}^{n} \dot{Q}_{evap,i}(k) + \sum_{i=2}^{n} \dot{Q}_{pipe,i}(k)}{\dot{m}_f c_f}, \tag{83}$$

$$T^{in}_{PVT}(k) = T^{in}_{ATES}\,(k-1) + \frac{\dot{Q}_{PVT} - \sum_{i=1}^{n} \dot{Q}_{evap}(k) - \sum_{i=2}^{n} \dot{Q}_{pipe,i}(k)}{\dot{m}_f c_f}, \tag{84}$$

$$T^{in}_{ATES}(k) = T^{in}_{ATES}\,(k-1) + \frac{\dot{Q}_{PVT} - \dot{Q}_{ATES} - \sum_{i=1}^{n} \dot{Q}_{evap}(k) - \sum_{i=1}^{n} \dot{Q}_{pipe,i}(k)}{\dot{m}_f c_f} \tag{85}$$

To determine when heat is added or extracted from the district heating network and buildings, a control strategy is created for optimal performance of the system. This heat control is implemented in the heat pumps and the PVT. For the heat pumps, the inside temperature is measured at each 15-minute interval and compared with the desired inside temperature. If the inside temperature is lower than the desired temperature and the heating fluid at the output of the building is colder than the 50°C threshold, the heat pump activates. It delivers sufficient heat to raise the fluid temperature entering the building to 53°C, ensuring the correct amount of heat is transferred, matching the heat extracted from the heating fluid into the house.

The control of the PVT heat involves a tank used for temporarily storing the thermal energy. Water in the tank is heated by the PVT modules, and the district heating network is heated by this tank. The tank exchanges heat with the district heating network only if its temperature is higher than that of the network. This design ensures that the PVT modules never cool down the network, as the tank will not transfer heat to the network unless it has a higher temperature. This approach optimises the heat management, ensuring efficient and effective heating within the system.

2.3.2 Electrical Network

The electrical components: PV, HP, ATES pumps, buildings and grid are connected together in the electrical network shown in Figure 12. The next chapter explains its design.

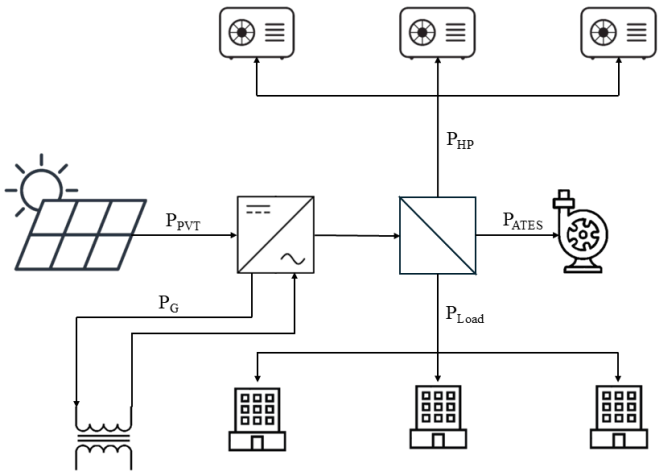

Figure 12: Electrical network configuration

The PV modules produce electricity, as outlined in Equation 72. This generated electricity is direct current (DC) and is converted to alternating current (AC) through an inverter, aligning with the operational requirements of other components in the system. The inverter also connects the electrical exchange with the grid. The power use of the ATES pump and heat pumps are calculated in Equation 75 and 38. Specifically, the ATES pump is supplied with the power needed to maintain the required water flow, while each heat pump receives the power needed to heat the water to the desired temperature for building inlet.

2.3.3 District

The parameters of the model are summarised in the Appendix A.3([36] [38] [25] [27]). The equations from Sections 2.1 and 2.2 are implemented in the model. To generate results, the parameters mentioned earlier are defined. Some values in the previously mentioned equations remain variable to facilitate the creation of multiple scenarios for the research.

The previously mentioned parameters depend on the individual components and are therefore not dependent on the configuration and topology of the district. To create a representative approximation of the district in Hilversum, the sizes of the buildings and pipes need to be implemented. For simplicity, the building sizes are considered in three categories: small, medium, and large. Provided data of the buildings is used to calculate the average dimensions for each category of buildings. The annual energy consumption was predicted per building, and this average will be used to scale the synthetic load profile.

Table 1: Parameters of different building sizes [35]

Parameter	**Value**			**Units**
	Small	Medium	Large	
Length	35	50	70	m
Width	25	30	40	m
Height	6	7	8	m
Roof area	874	1,504	3,130	m^2
Glass area	213	400	647	m^2
Annual energy consumption	54,455	72,283	285,836	kWh

Then, the map of the Hilversum Werf is used to approximate the length of the tubes in the district heating network. Below, the map is visualised, showing building sizes marked by colored dots as indicated in the legend, and the different pipes, each with its respective length. These lengths are summarized in Table 2.

Figure 13: Map Hilversum Werf

Table 2: Pipe lengths

Parameter	**L1**	**L2**	**L3**	**L4**	**L5**	**L6**	**L7**	**L8**	**L9**	**L10**	**L11**	**L12**	**L13**	**L14**	**L15**
Value (m)	30	30	45	45	50	50	30	30	50	60	50	40	30	50	30

3 Distribution and Configuration

This chapter presents the case studies to analyse the operation of our model. The Python model previously described will be tested in different scenarios. The parameters in Chapter 2 will remain fixed, while the number, size, and location of ATES, as well as the number of PVT modules, will be variable. First, different scenarios will be researched with regard to the ATES distribution, focusing on thermal losses and overall performance. Then, the different sizes and configurations of ATES and PVT will be analysed, which will determine the system's generation and stability. Finally, an optimisation method is applied to optimise the sizes of the system, resulting in minimal CO_2 emissions.

The initial district heating map, shown in Figure 13, is used as the base case. From this starting point, two cases are developed. First, the centralised ATES case is constructed. The the network will be researched using different cases on centralised and distributed ATES.

3.1 Centralised ATES

The model constructed in Python can be visualised in Figure 14. The base case Hilversum district heating network is used with a single ATES. The radius of the ATES is depicted as a red line, with the center marked by a red dot. The ATES is considered a perfect circle with a specific radius and height. The aquifer consists of water and sand, with the water assumed to be perfectly mixed within the sand of the aquifer. The input and output of the aquifer are visualized using pipes with lengths L16 and L17. The initial amount of PVT modules is based on Hilversum's plans to install 800 solar modules on the carport roof. The parameters are summarised below.

Figure 14: Map Hilversum Werf centralised ATES

Table 3: Parameters centralised ATES

Parameter	Symbol	Value	Units
Radius ATES	R	250	m
Height ATES	d	10	m
Number of PVT	n	800	-
Length pipe 16	L	70	m
Length pipe 17	L	100	m

Below is the graph showing the temperatures at different components of the district heating network during a year, in Figure 15. The month labels are centered on the respective months. The graph illustrates the temperatures at the output of the PVT (green circle in Figure 14), the output of the ATES (orange cirlce in Figure 14) and the input of the ATES (blue circle in 14). The highest temperatures are recorded immediately after the PVT, where the water has just been heated. The temperature of the water exiting the ATES remains the most stable, reflecting the internal temperature of the ATES. The water entering the ATES is the coldest, as heat has been extracted by the heat pumps to warm the buildings. The large fluctuations in temperatures are due to the daily variations between day and night. The PVT generates heat only during the day, and the low peak from the heat pumps corresponds to the morning heating peak in the buildings when the desired temperature rises from 17°C to 20°C.

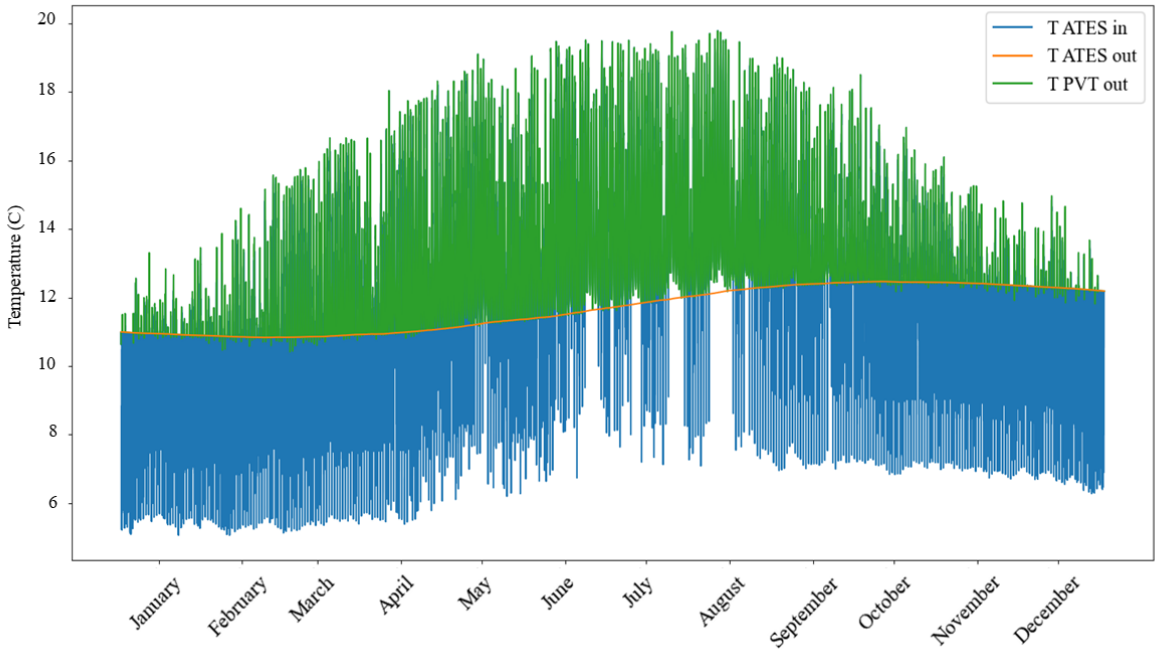

Figure 15: Temperatures district heating network centralised ATES

Next, the heat transfer of all components is visualised during a year in Figure 16. Positive heat is set as heat added to the system, whereas negative heat extracts heat from the network. The highest fluctuations in heat are from the PVT and heat pumps due to daily variations. It can be seen that in winter the building losses are highest and heat added by the PVT is lowest, resulting in the most usage of the heat pumps extracting the most heat from the network during this season. In summer, it is all the other way around. The losses in the ATES are relatively low and stable, and the losses in the pipes are so small that they don't have a significant effect on the system. In Table 24, the total heat transfer over the year is summarized for all components, providing a complete visualisation of the system.

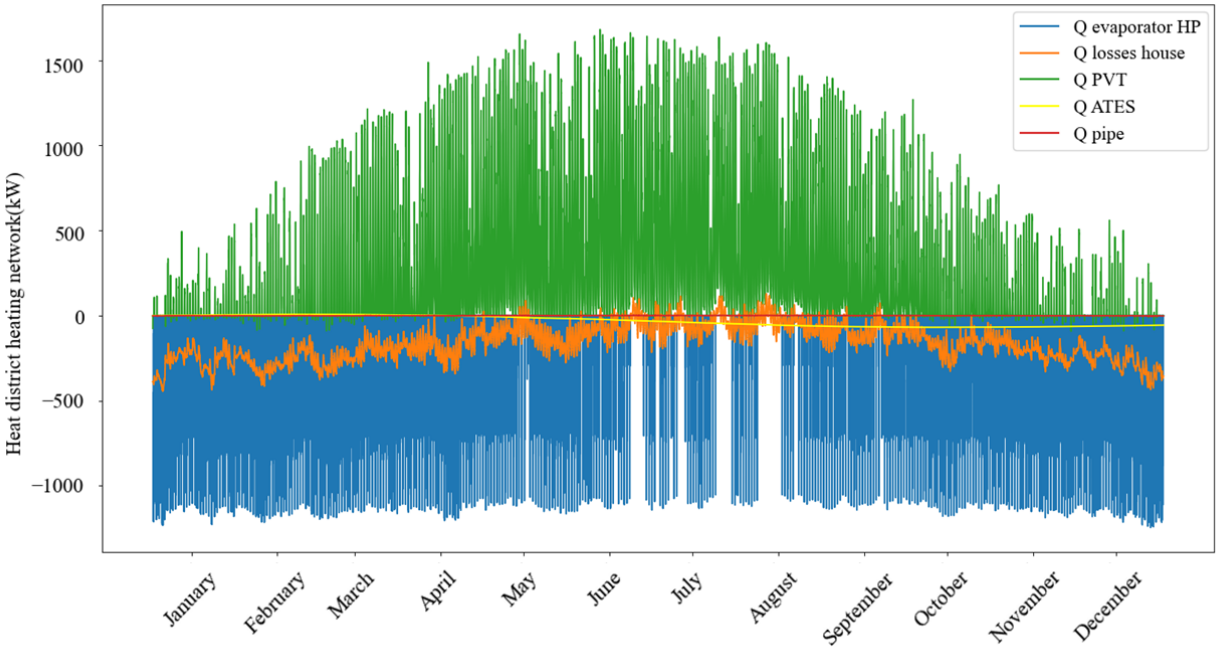

Figure 16: Heat transfer per component centralised ATES

Table 4: Total heat transfer per component

Result	**Symbol**	**Value [MWh]**
PVT	Q_{PVT}	2504
Losses buildings	Q_{loss}	-1410
Evaporator HP	Q_{evap}	-956.0
Heat ATES loss	$Q_{\text{ATES,loss}}$	-277.1
Heat pipe loss	$Q_{\text{pipe,loss}}$	-3.520

Figure 17 presents the annual power supplied and used per component is visualised. The power of the PV within the PVT modules is the only power supplied by the system and is dependent on the irradiance. The power load of the buildings is a fixed synthetic load profile, independent of the system. The power used by the heat pumps depends on the temperature of the district heating network and the temperature in the building. The higher the temperature in the district heating, the more heat can be extracted by the heat pump, and less power would be necessary for the same effect. The power used by the ATES pump is considered constant because water flows constantly in and out of the aquifer. The total annual power supply and usage per component are summarised in Table 5.

Additionally, the exchange with the grid to make the system work is also calculated. The shortage and surplus of power are calculated every 15 minutes. Summing these values gives the net grid power exchange over a year, this is shown in Table 5.

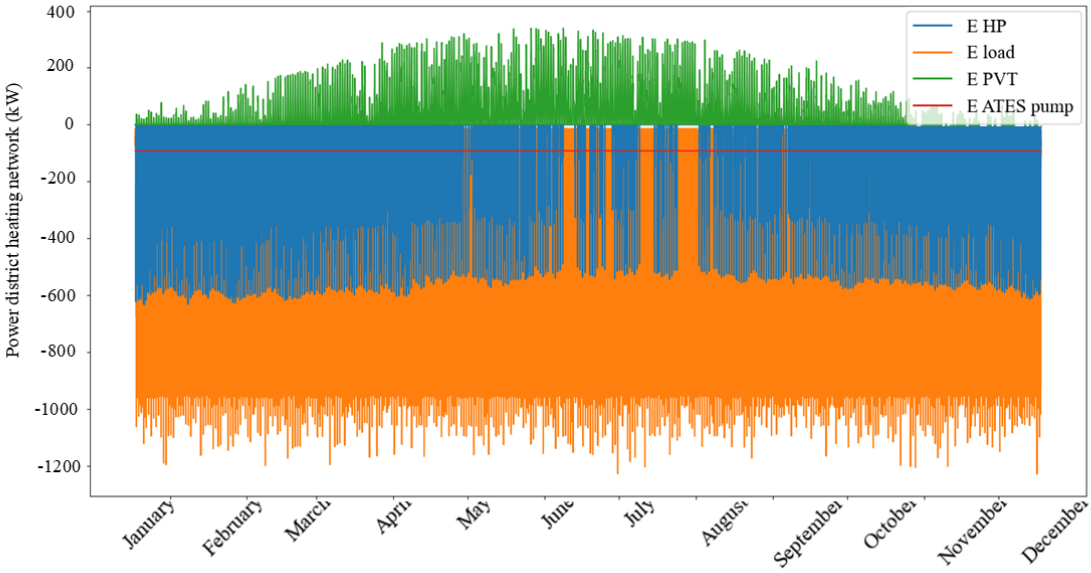

Figure 17: Power per component centralised ATES

Table 5: Total electrical energy transfer per component

Result	**Symbol**	**Value**	**Units**
PVT	E_{PVT}	393.7	MWh
Load buildings	E_{load}	-1120	MWh
Heat pump	E_{HP}	-452.9	MWh
ATES pump	E_{ATEP}	-805.6	MWh
Shortage grid	$E_{\text{grid,shortage}}$	-2023	MWh
Surplus grid	$E_{\text{grid,surplus}}$	38.46	MWh
Net grid	E_{grid}	-1985	MWh

The coefficient of performance (COP) of a heat pump is the ratio of the amount of electricity used to the heat supplied by the pump. This relationship is expressed in Equation 37. A higher temperature in the district heating network results in a higher COP, meaning less power is needed. Figure 18 below illustrates the COPs of all 15 heat pumps, which range from 2.77 to the maximum value of 3.60.

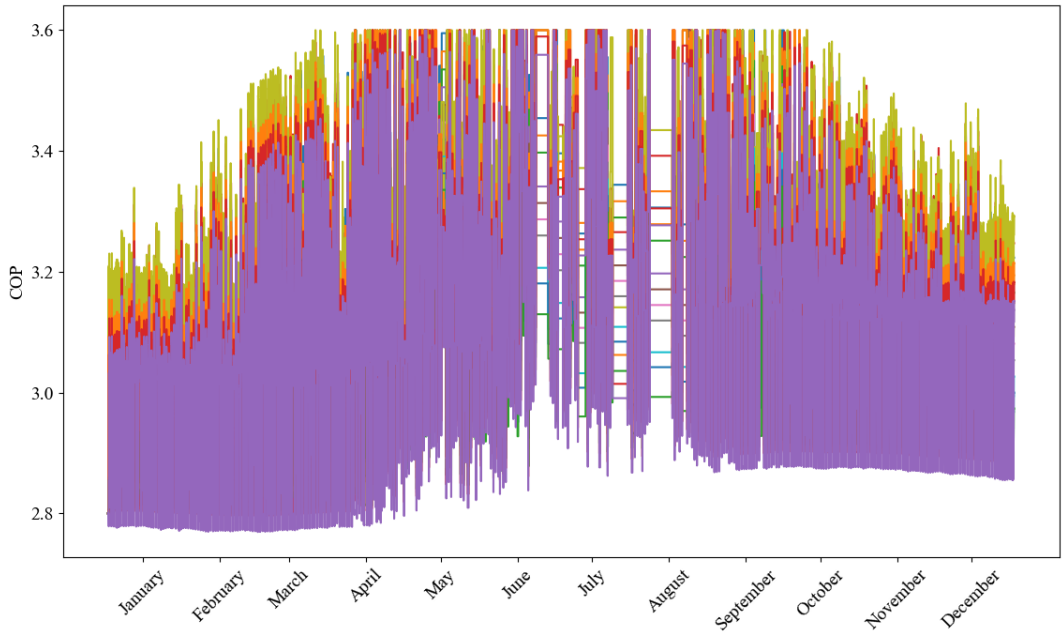

Figure 18: COP heat pumps centralised ATES

Due to the control system, the temperature inside the buildings is kept relatively stable. The heat pumps add heat when the indoor temperature drops below 20°C during the day and 17°C at night. This results in a consistent indoor temperature across all buildings, ranging between 18.93°C and 21.05°C, with the highest temperatures occurring as two peaks due to the relatively mild climate in the Netherlands. The differences in temperature between buildings are minimal and not easily visible in the annual graph (Figure 19). Therefore, a zoomed-in graph for a single week is also provided in Figure 20 to better illustrate these variations.

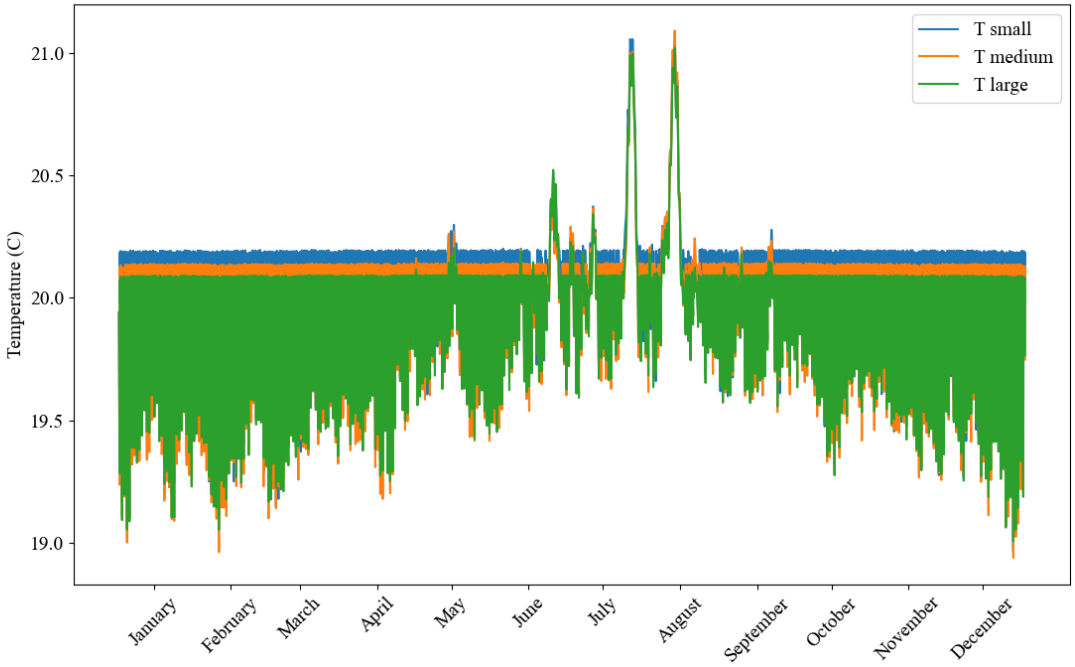

Figure 19: Temperatures buildings centralised ATES

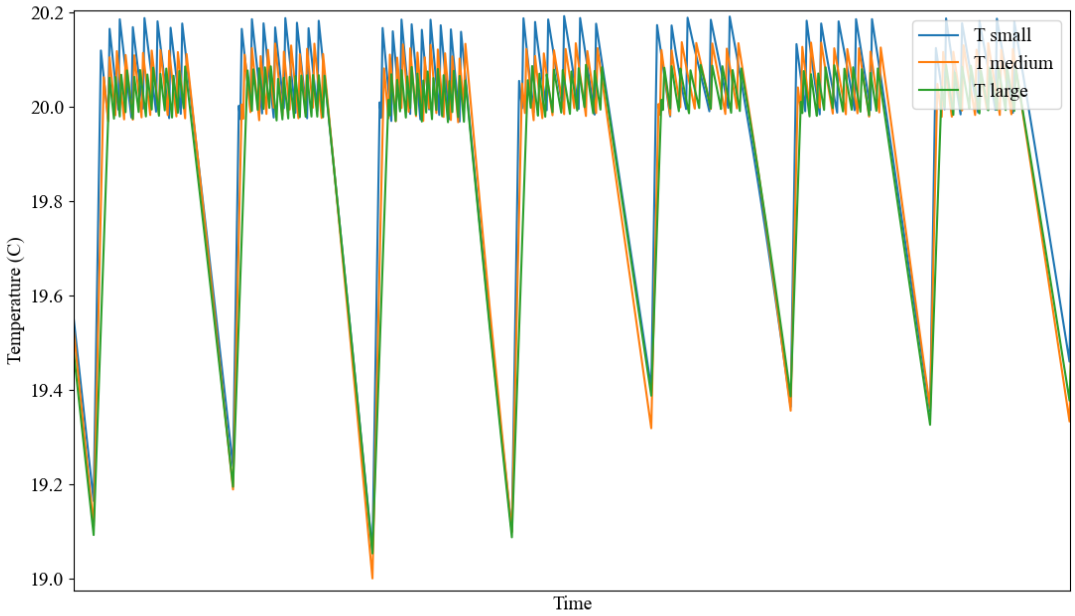

Figure 20: Temperatures buildings one week

Power to heat storage

During certain times of the year, the system generates surplus power, as illustrated in Table 5. This excess power can be sold to the grid at the corresponding power price. However, to minimise grid exchange, it's advantageous to utilise a form of power storage. One effective method is converting surplus power into heat using a heat pump, which can be integrated into the district heating network. The current building heat pumps are not ideal for this conversion, as they would draw heat from the buildings, leading to a cooling effect. Instead, an additional air-to-water heat pump is used to be connected to the district heating network specifically to utilise the surplus power. This setup is depicted in Figure 21.

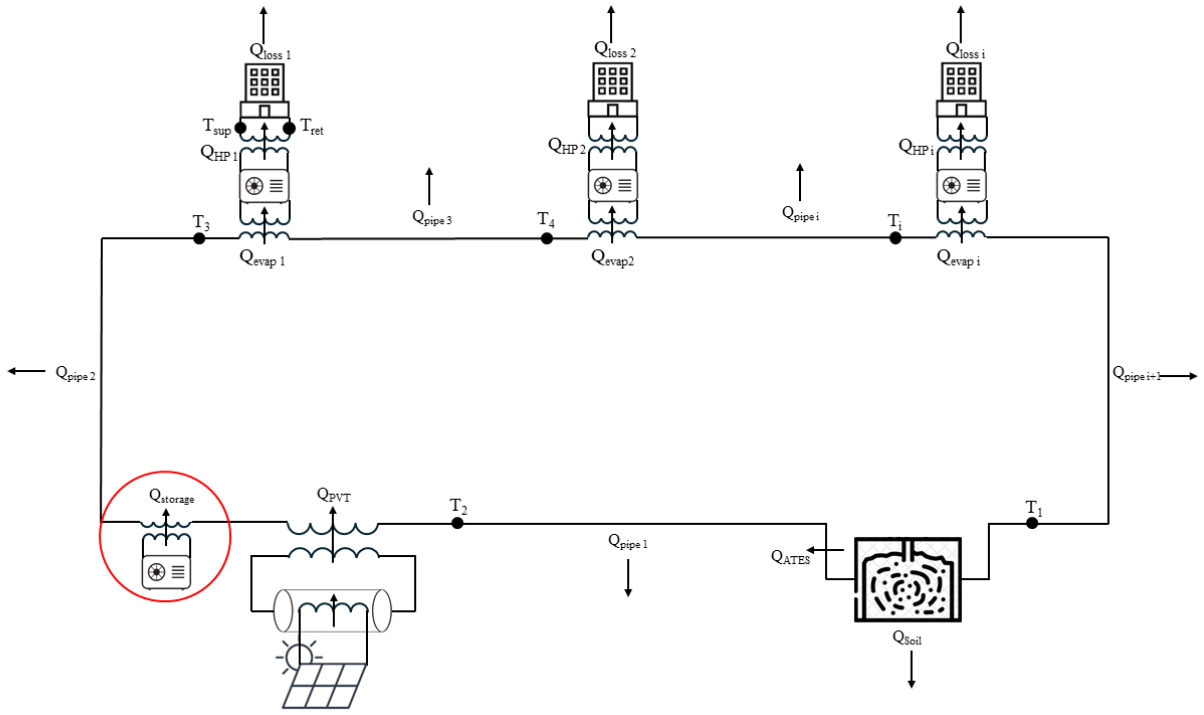

Figure 21: Thermal schematic including storage

The COP of the heat pump can be determined using a similar approach as in Equation 73, with the inlet temperature being the ambient temperature:

$$\mathrm{COP}(k) = 7.90471e^{-0.024(T_{\mathrm{amb}}(k)-T_{ret}(k))} \tag{86}$$

This results in the following heat supply calculation:

$$\dot{Q}_{\mathrm{HP}}(k) = P_{\mathrm{HP}}(k)\mathrm{COP}(k) \tag{87}$$

The integration of extra heat into the district heating network leads to an elevated temperature post-PVT and additional heat pump. This high-temperature water is then circulated throughout the district and used by the corresponding heat pumps. Notably, the extra heat pumps contribute additional heat only during periods of surplus power. These surpluses typically occur in 15-minute intervals, during which the heat pumps do not actively add extra heat to the buildings, resulting in no additional power or heat usage. Consequently, during these moments when the extra heat pump is operational, the building heat pumps do not extract the heat, causing the high-temperature water to flow into the aquifer after traversing through all the tubes in the system. The high-temperature water entering the aquifer are illustrated in Figure 22.

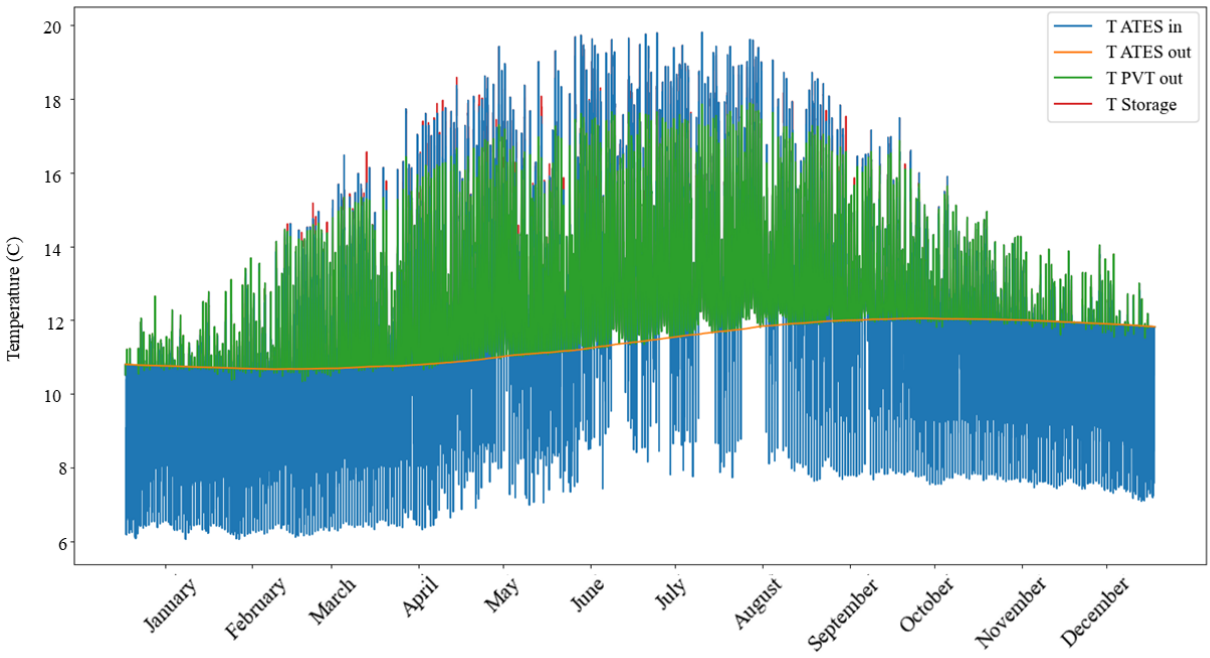

Figure 22: Temperatures district heating network centralised ATES with power to heat storage

The corresponding heat transfer including the extra heat added by the extra power-to-heat heat pump ($Q_{storage}$) is shown in Figure 23. The total heat transfer is shown in Table 13.

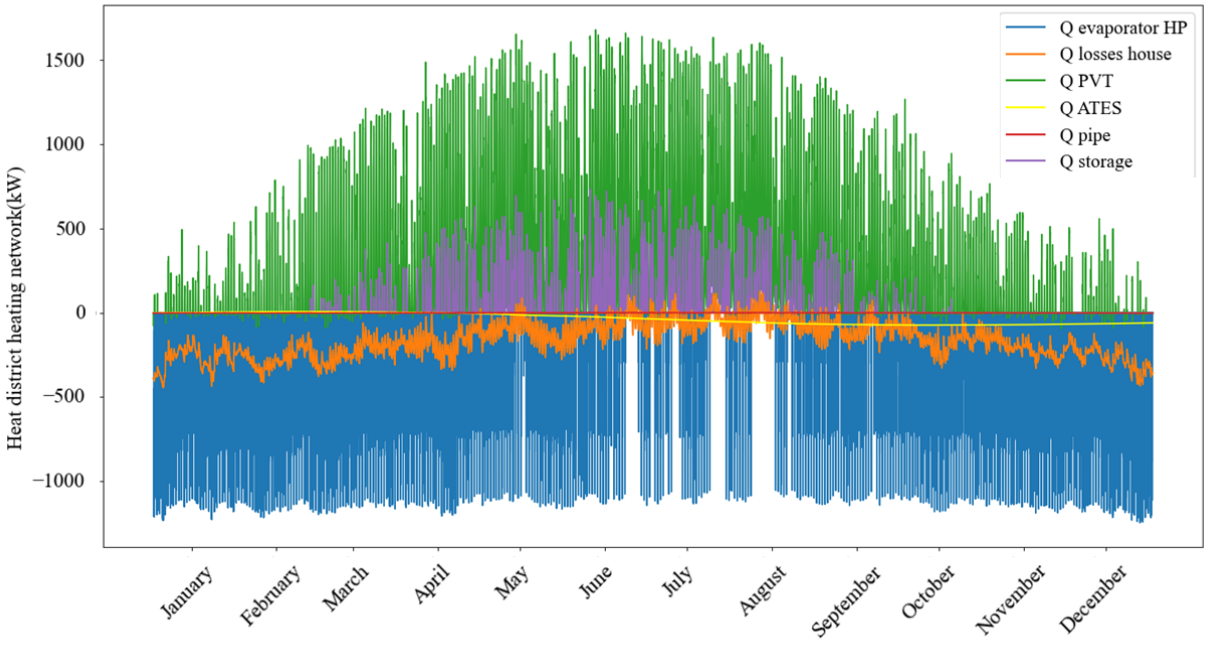

Figure 23: Heat transfer per component centralised ATES with power to heat storage

Table 6: Total heat transfer per component with power to heat storage

Result	Symbol	Value [MWh]
PVT	Q_{PVT}	2494
Losses buildings	Q_{loss}	-1409
Evaporator HP	Q_{evap}	-957.0
ATES loss	$Q_{\text{ATES,loss}}$	-319.1
Pipe losses	$Q_{\text{pipe,loss}}$	-3.828
Storage	Q_{storage}	138.5

The power usage and supply per component during a year is shown in Figure 24, the corresponding total power and grid exchange is shown in Table 14.

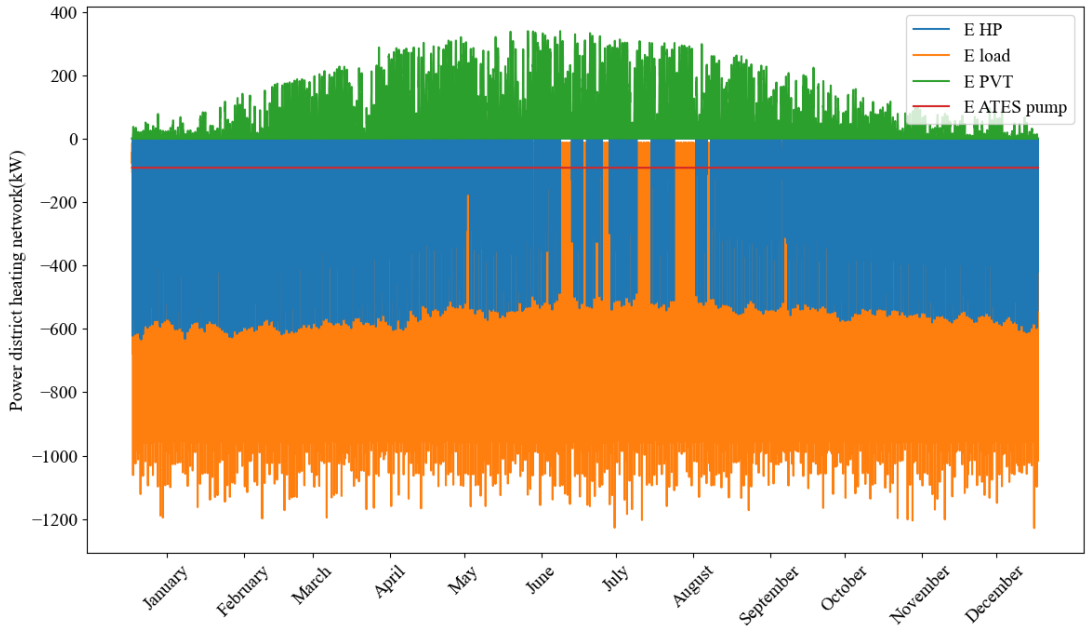

Figure 24: Power per component centralised ATES with power to heat storage

Table 7: Total electrical energy transfer per component with power to heat storage

Result	Symbol	Value [MWh]
PVT	E_{PVT}	393.7
Load buildings	E_{load}	-1120
Heat pump	E_{HP}	-452.0
ATES pump	E_{ATEP}	-805.6
Shortage grid	$E_{\text{grid,shortage}}$	-1984
Surplus grid	$E_{\text{grid,surplus}}$	0.0
Net grid	E_{grid}	-1984

The higher temperature in the district heating network due to the extra heat pump leads to slightly higher COP's of the heat pumps. The results are shown in Figure 38.

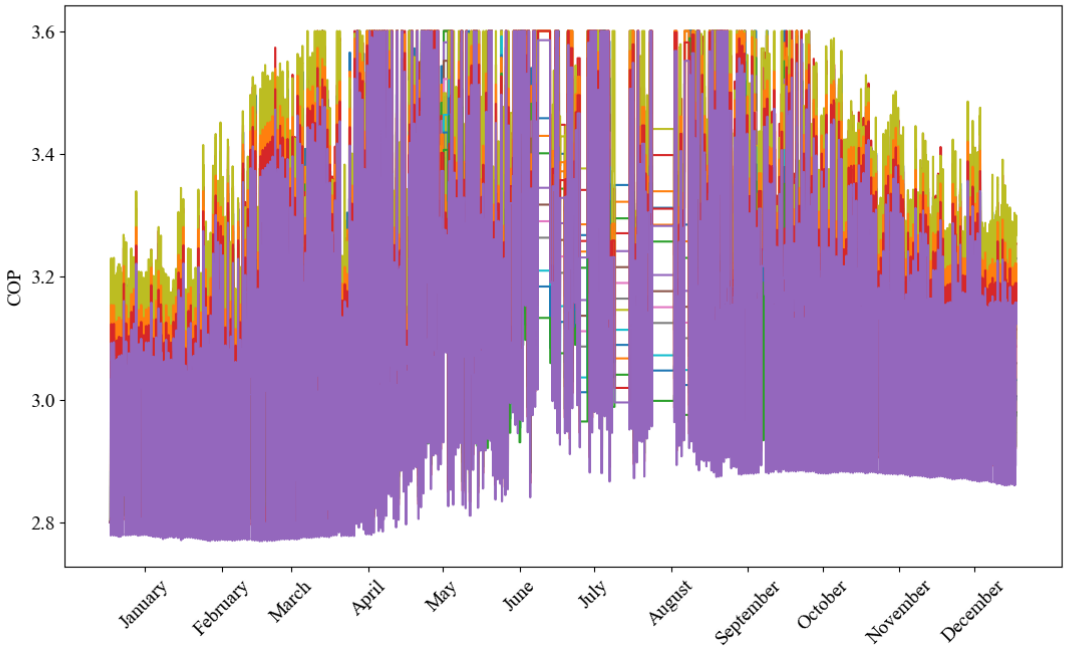

Figure 25: COP heat pumps centralised ATES with power to heat storage

To evaluate the effects and advantages of the extra power-to-heat storage, an analysis of the grid exchange is conducted. This involves tracking the amount of shortage and surplus power in both scenarios. For a comprehensive evaluation, the economic benefits are also calculated. The net power exchange with the grid is assessed by multiplying each interval's net power exchange by the corresponding power price. The total electrical energy purchase and injection are summarised in Table 15. The economical calculation includes costs incurred during power shortages and profits from selling surplus power back to the grid. The power prices for 2023, illustrated in Figure 26, are utilised for these calculations. The total power costs associated with grid exchange are summarised in Table 16.

Table 8: Grid power exchange

Result	**Symbol**	**Value [MWh]**
Without storage		
Grid shortage	$E_{\text{grid,shortage}}$	-2023
Grid surplus	$E_{\text{grid,surplus}}$	38.46
With storage		
Grid shortage	$E_{\text{grid,shortage}}$	-1984
Grid surplus	$E_{\text{grid,surplus}}$	0.0

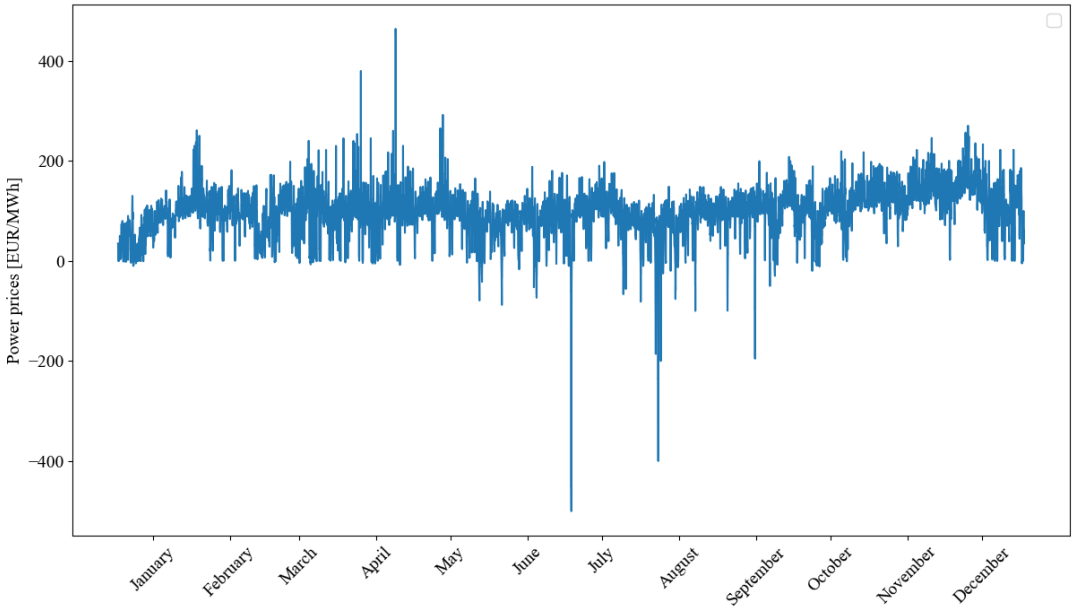

Figure 26: Power prices Netherlands 2023

Table 9: Net power price

Result	**Symbol**	**Value [EUR]**
Cost without storage	-	211,000
Cost with storage	-	214,000

Cooling network

A fifth-generation district heating network is designed to provide both heating and cooling capabilities, as detailed in Section 1.2.3. The initial model employs a single district heating circulation system combined with a mixed ATES for the injection and supply of water. Given the mild and relatively cold climate of the Netherlands, an assessment was conducted to determine the necessity of implementing a cooling network. This assessment assumes that buildings require cooling when the indoor temperature exceeds 24°C. Under current weather conditions, indoor temperatures do not surpass this threshold. To investigate the effects of an extreme hot summer, an artificial ambient temperature profile was created, increasing the temperatures by 4°C from May to September compared to the original profile. This scenario aims to simulate the potential need for cooling under significantly warmer conditions. The resulting indoor temperatures of buildings under this scenario are illustrated in Figure 27. The maximum inside temperature is 23.47°C.

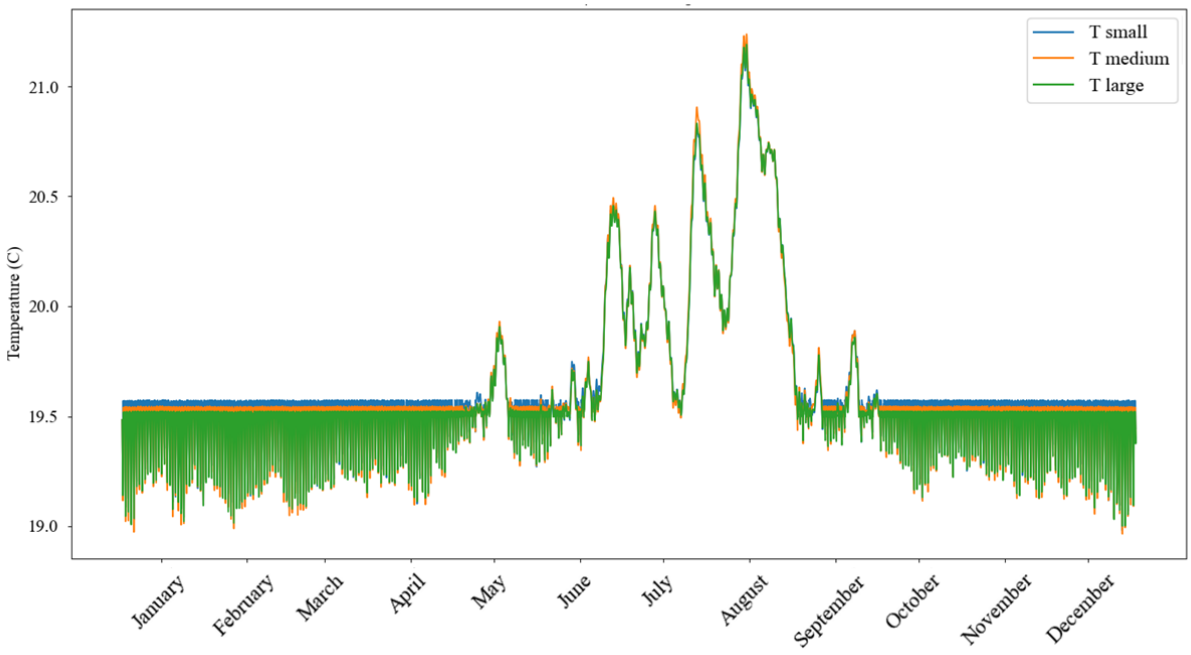

Figure 27: Temperatures buildings centralised ATES extreme summer

3.2 Distributed ATES

The second scenario, illustrated in Figure 28, involves the implementation of multiple ATES systems within the base case of the Hilversum district heating network. The locations for these ATES systems are strategically selected to ensure an equal distribution of buildings between each aquifer and to prevent overlap between the aquifers. The sizes of the individual ATES systems are designed so that their combined total volume matches that of a centralised system utilising a single aquifer. To integrate these ATES systems into the existing district heating network, additional pipes are installed, while all other parameters remain unchanged.

Figure 28: Map Hilversum Werf distributed ATES

Table 10: Parameters distributed ATES

Parameter	Symbol	Value	Units
Radius ATES	R	144	m
Height ATES	d	10	m
Number of PVT	n	800	-
Length pipe 16	L	70	m
Length pipe 17	L	100	m
Length pipe 18	L	80	m
Length pipe 19	L	110	m
Length pipe 20	L	80	m
Length pipe 21	L	80	m

The graph below illustrates the temperatures recorded at various components for the distributed ATES scenario. Each ATES unit is monitored individually to track its specific temperature. The input temperatures of the ATES are not shown due to excessive overlap, which would reduce clarity in the graph. For simplicity, the graph presents the average temperature of all ATES, as the temperature variations among them are too minor to be significant in the primary Figure 29. To better visualise these subtle differences, a zoomed-in version of the graph displaying two random days is provided in Figure 30.

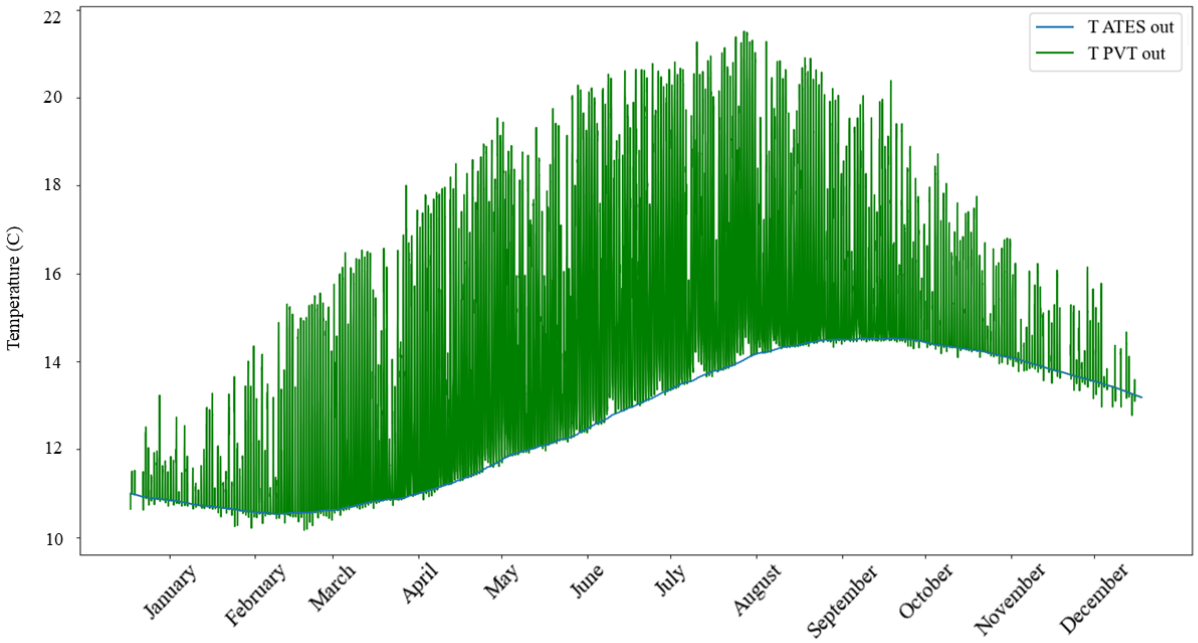

Figure 29: Temperatures district heating network distributed ATES

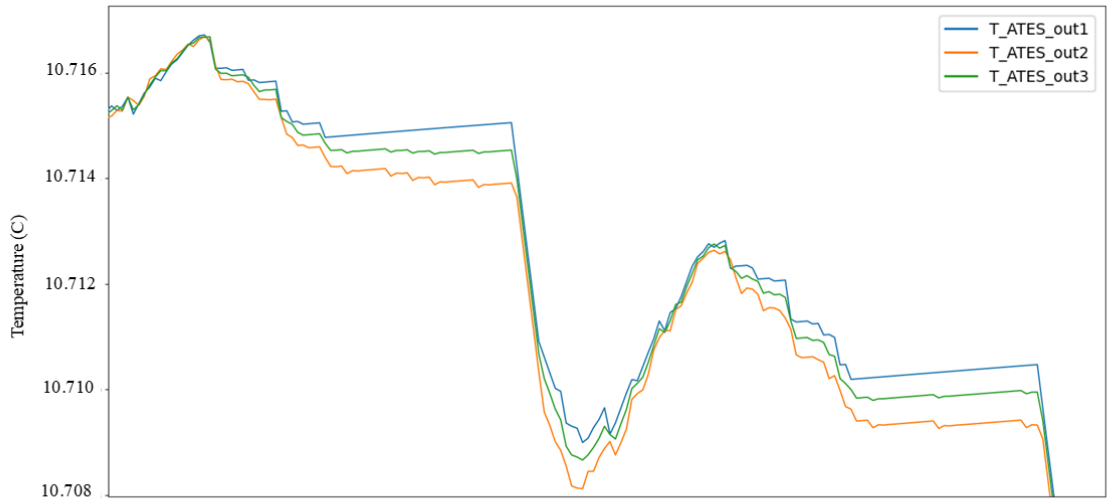

Figure 30: Temperatures distributed ATES

Next, the heat transfer of all components is visualised for distributed ATES in Figure 31. The heat transfer from the ATES represents the cumulative heat transfer from all three ATES units. This total is higher compared to the centralised case, which can be explained to the elevated temperatures in the ATES units, as illustrated in Figure 29. The total heat transfers is summarised in Table 11.

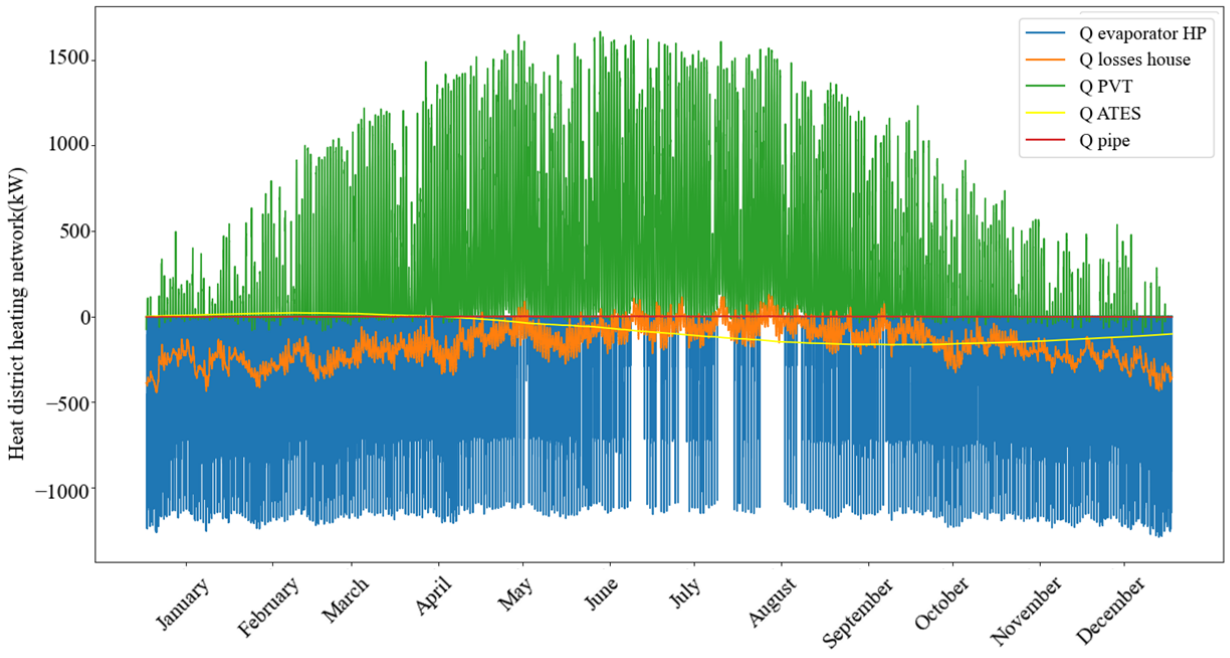

Figure 31: Heat transfer per component distributed ATES

Table 11: Total heat transfer per component with distributed ATES

Result	**Symbol**	**Value [MWh]**
PVT	Q_{PVT}	2408
Losses buildings	Q_{loss}	-1410
Evaporator HP	Q_{evap}	-969.0
ATES losses	$Q_{\text{ATES,loss}}$	-664.4
Pipe losses	$Q_{\text{pipe,loss}}$	-4.895

The power graph in Figure 32 illustrates the annual power supplied and used for each component within the distributed storage system. A particularly noticeable element is the power consumption by the ATES pump, which is three times larger because of the three ATES units. Consequently, this leads to a substantially greater net grid usage and an almost negligible amount of surplus power, as detailed in Table 12.

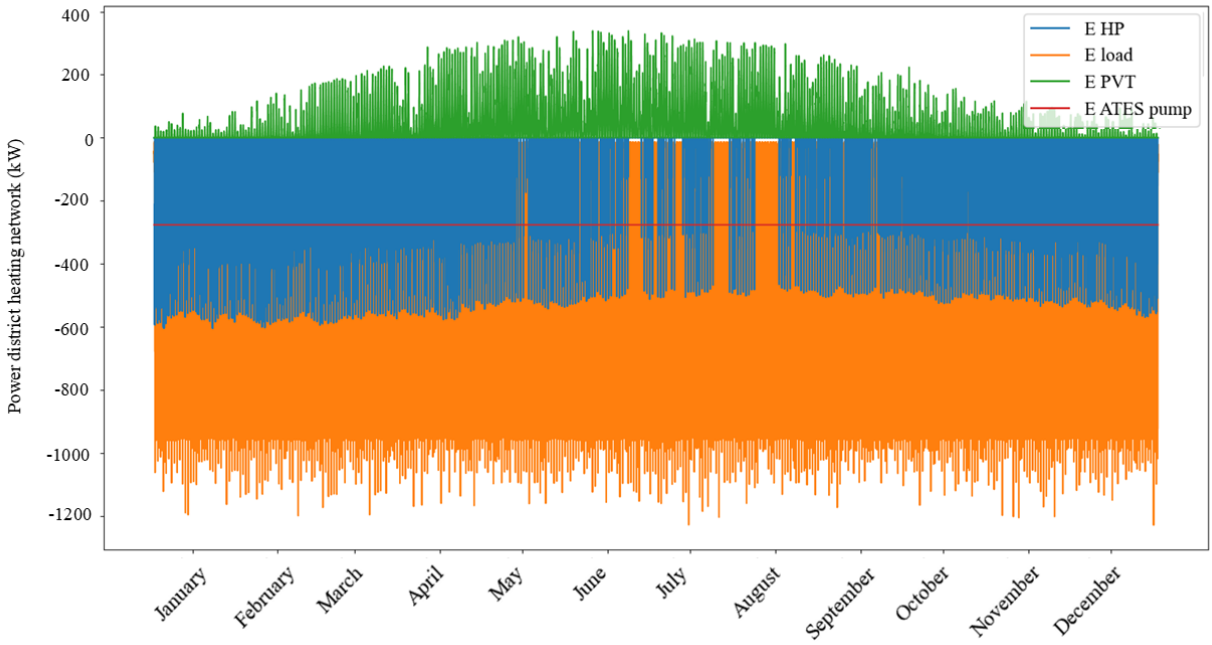

Figure 32: Power per component distributed ATES

Table 12: Total electrical energy transfer per component with distributed ATES

Result	**Symbol**	**Value [MWh]**
PVT	E_{PVT}	393.7
Load buildings	E_{load}	-1119
Heat pump	E_{HP}	-440.0
ATES pump	E_{ATEP}	-2417
Shortage grid	$E_{\text{grid,shortage}}$	-3583
Surplus grid	$E_{\text{grid,surplus}}$	0.02945
Net grid	E_{grid}	-3583

Figure 33 below illustrates the COPs of the heat pumps in the distributed ATES scenario. The COP values are less extreme compared to the centralised scenario and follow the temperature profile of the district heating system more closely. This is because the distributed ATES levels the peak temperatures across the entire district heating system, resulting in a smaller variation in COP. This effect is particularly noticeable for the heat pumps just before entering the PVT.

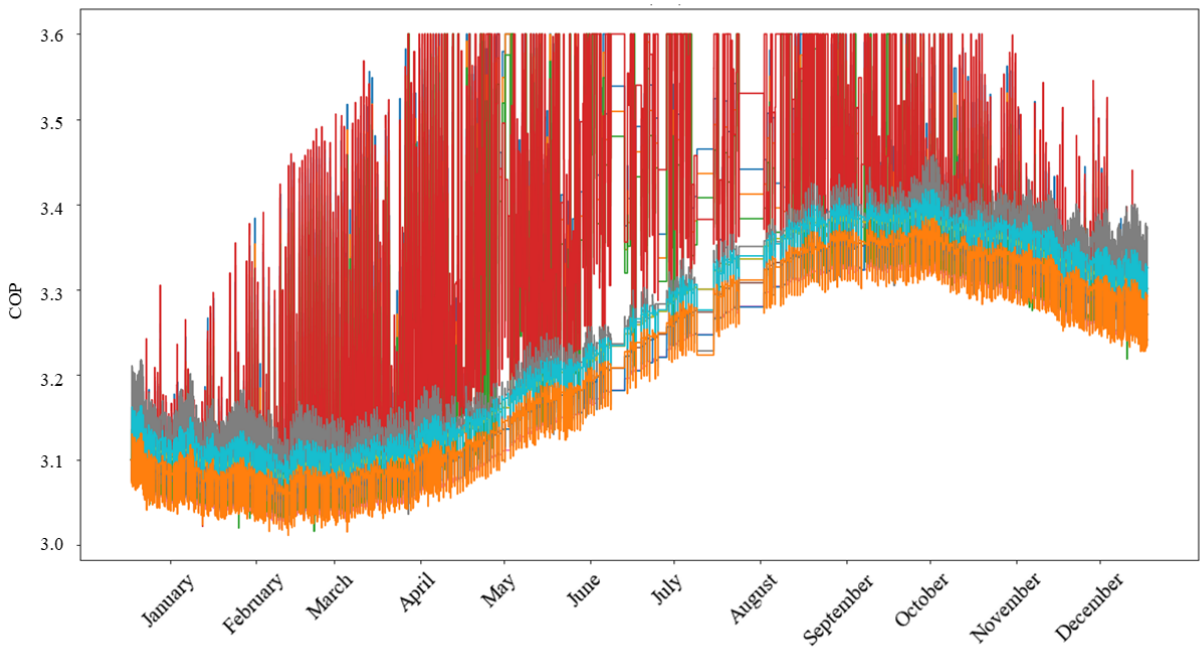

Figure 33: COP heat pumps distributed ATES

The temperatures in the buildings are shown in Figure 34, which remains unchanged compared to the centralised ATES scenario. The heat supplied to the buildings by the heat pumps is independent of the system's temperature.

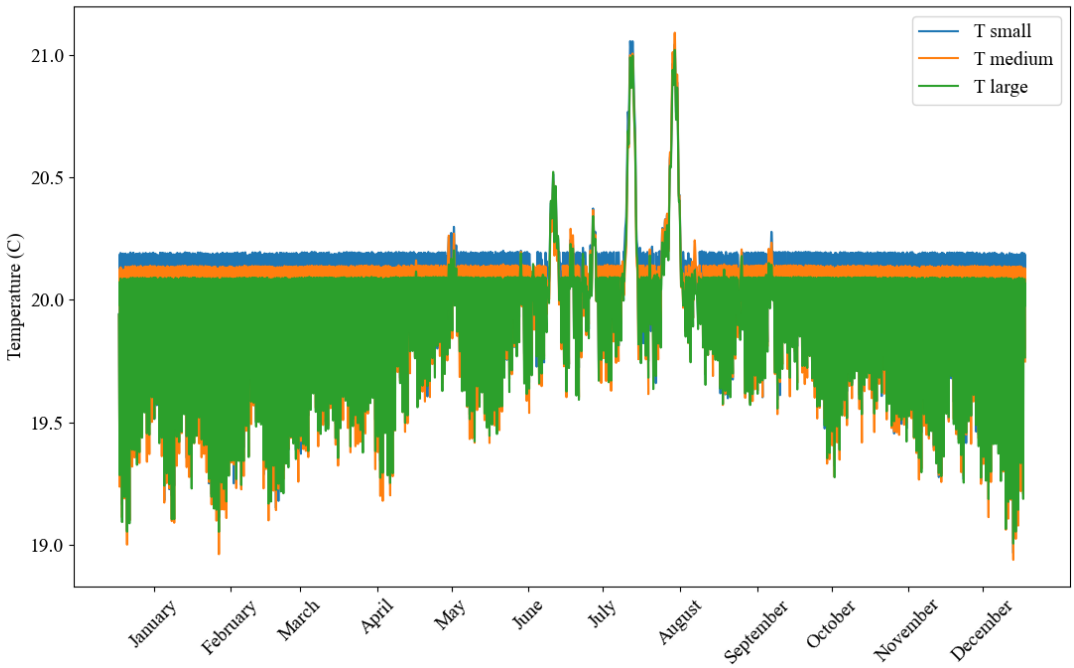

Figure 34: Temperatures buildings distributed ATES

Power to heat storage

In the distributed case, the same power-to-heat storage configuration is used to store surplus energy. However, due to the very low surplus energy in this scenario, the power usage remains relatively high throughout the year, primarily because of the additional ATES pumps. Consequently, there is minimal energy available to store as heat, leading to insignificant differences in the subsequent graphs and tables.

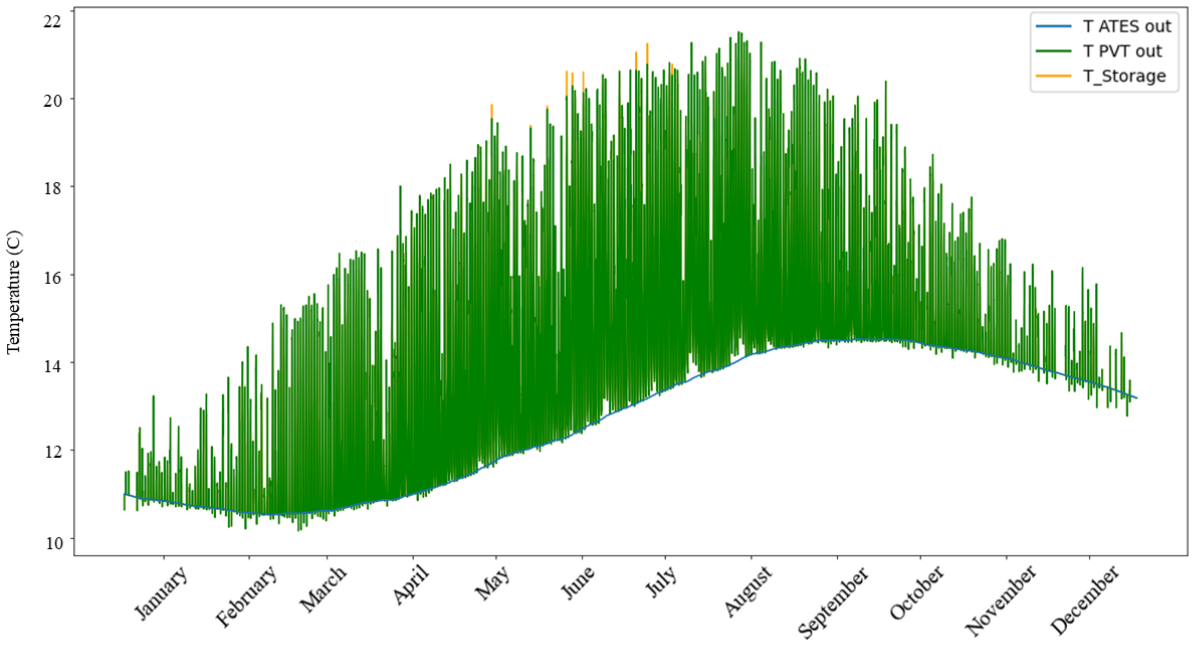

Figure 35: Temperatures district heating network distributed ATES with power to heat storage

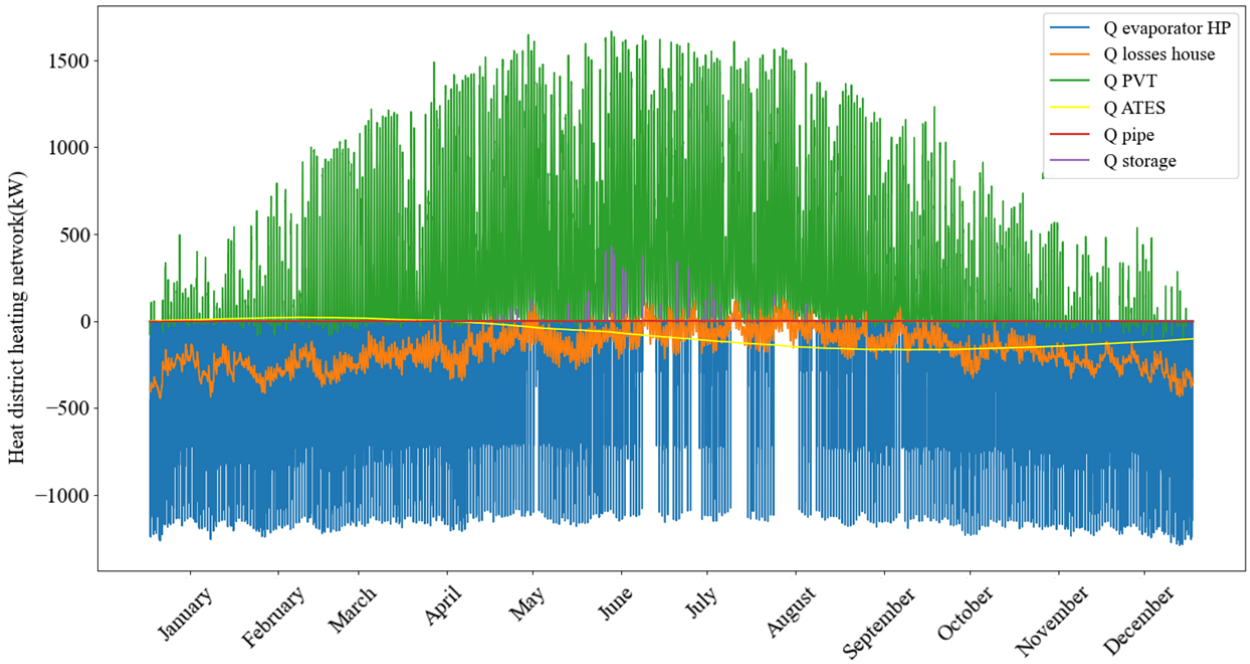

Figure 36: Heat transfer per component distributed ATES with power to heat storage

Table 13: Total heat transfer per component with power to heat storage

Result	Symbol	Value [MWh]
PVT	Q_{PVT}	2408
Losses buildings	Q_{loss}	-1410
Evaporator HP	Q_{evap}	-969.0
ATES losses	$Q_{\text{ATES,loss}}$	-665.2
Pipe losses	$Q_{\text{pipe,loss}}$	-4.899
Storage	Q_{storage}	2.344

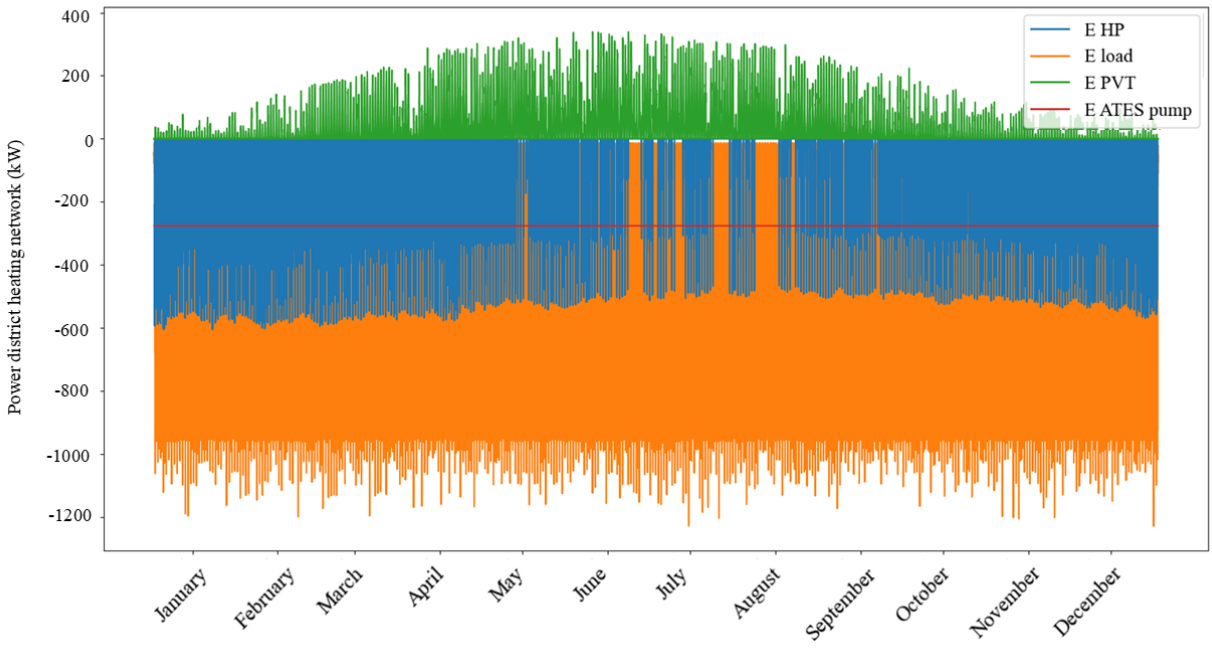

Figure 37: Power per component distributed ATES with power to heat storage

Table 14: Total electrical energy transfer per component with power to heat storage

Result	Symbol	Value [MWh]
PVT	E_{PVT}	393.7
Load buildings	E_{load}	-1119
Heat pump	E_{HP}	-440.0
ATES pump	E_{ATEP}	-2417
Shortage grid	$E_{\text{grid,shortage}}$	-3583
Surplus grid	$E_{\text{grid,surplus}}$	0.0
Net grid	E_{grid}	-3583

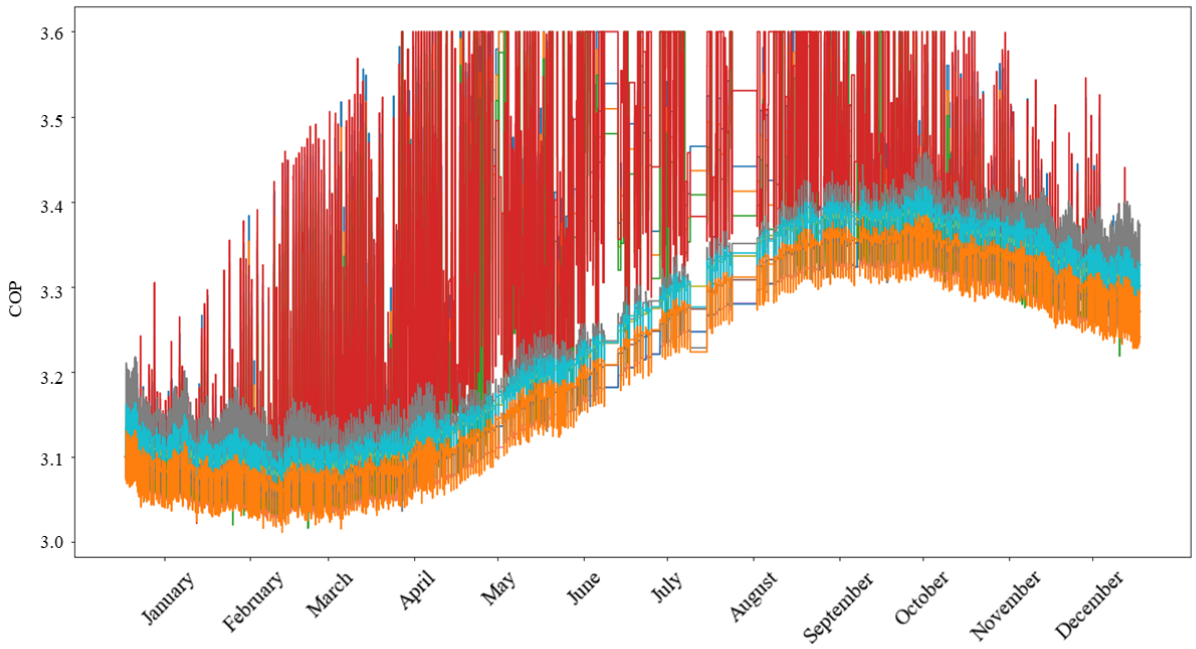

Figure 38: COP heat pumps distributed ATES with power to heat storage

Table 15: Grid power exchange

Result	Symbol	Value [MWh]
Without storage		
Grid shortage	$E_{\text{grid,shortage}}$	-3583
Grid surplus	$E_{\text{grid,surplus}}$	0.02945
With storage		
Grid shortage	$E_{\text{grid,shortage}}$	-3583
Grid surplus	$E_{\text{grid,surplus}}$	0.0

Table 16: Net power price

Result	Symbol	Value [EUR]
Cost without storage	-	365,000
Cost with storage	-	365,000

After evaluating the additional benefits of power-to-heat storage in both the centralised and distributed ATES scenarios, the following observations were made. In the centralised case, power-to-heat storage can prevent up to 38 MWh excess energy from being returned to the grid. However, this results in an increased total energy cost of 2,989.12 EUR. Economically, it is more advantageous to sell the surplus energy back to the grid rather than storing it. In the distributed ATES scenario, the difference is negligible due to the minimal surplus power caused by the high power usage of the ATES pumps.

In conclusion, the benefits of extra power-to-heat storage are too minimal when considering grid exchange savings. Additionally, it leads to additional costs on the electricity market, without even accounting for installation costs. Therefore, power-to-heat storage will not be considered in future configurations.

Cooling network

The same artificial ambient temperature profile, where May to September have an increased temperature of 4°C, is used. As shown in Figure 39, the results remain unaffected compared to the centralised case, with a maximum inside temperature of 23.47°C.

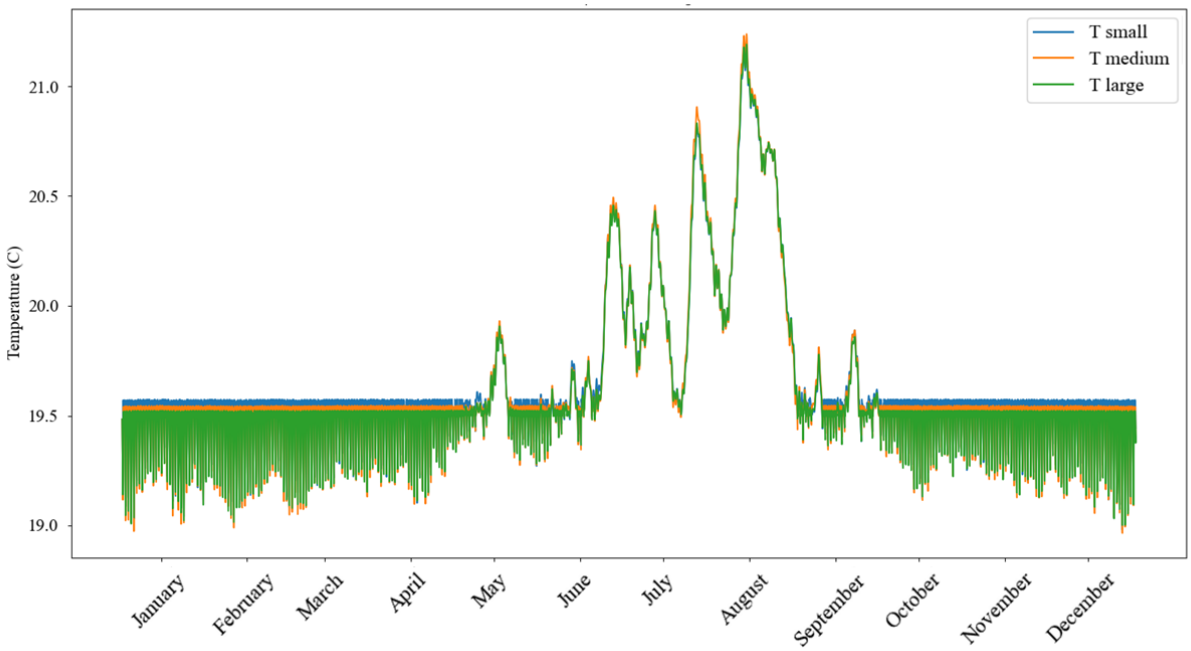

Figure 39: Temperatures buildings distributed ATES extreme summer

The necessity for cooling within the district heating network is evaluated for both the centralised and distributed ATES scenarios. In an extreme summer scenario, although the inside temperature rises, it does not exceed a level where cooling would be necessary. Thereby, the inside temperatures of the buildings remain independent of the district heating network temperatures due to the control mechanisms of the heat pumps. This indicates that it is unnecessary to include a cooling network for the Hilversum case study.

3.3 Configuration

The configuration of the network is researched in this section. Initially, a case will be created by altering the configuration of the main components. The base case depicted in Figure 13 will be adjusted to match the specified scenarios.

In this scenario, water enters the PVT after passing through the building district, before entering the ATES. Essentially, the positions of the PVT and ATES are switched, as illustrated in Figure 40. The main parameters remain consistent with those in the centralised ATES scenario. However, the tubes connecting the PVT are slightly different, as detailed in Table 17.

Figure 40: Map Hilversum Werf centralised ATES

Table 17: Parameters centralised ATES

Parameter	Symbol	Value	Units
Radius ATES	R	250	m
Height ATES	d	10	m
Number of PVT	n	800	-
Length pipe 16	L	50	m
Length pipe 17	L	100	m

The temperatures of the district heating network are shown in Figure 41. The temperature going into the PVT is shown instead of the temperature going into the ATES, to illustrate the temperature of the water exiting the building district.

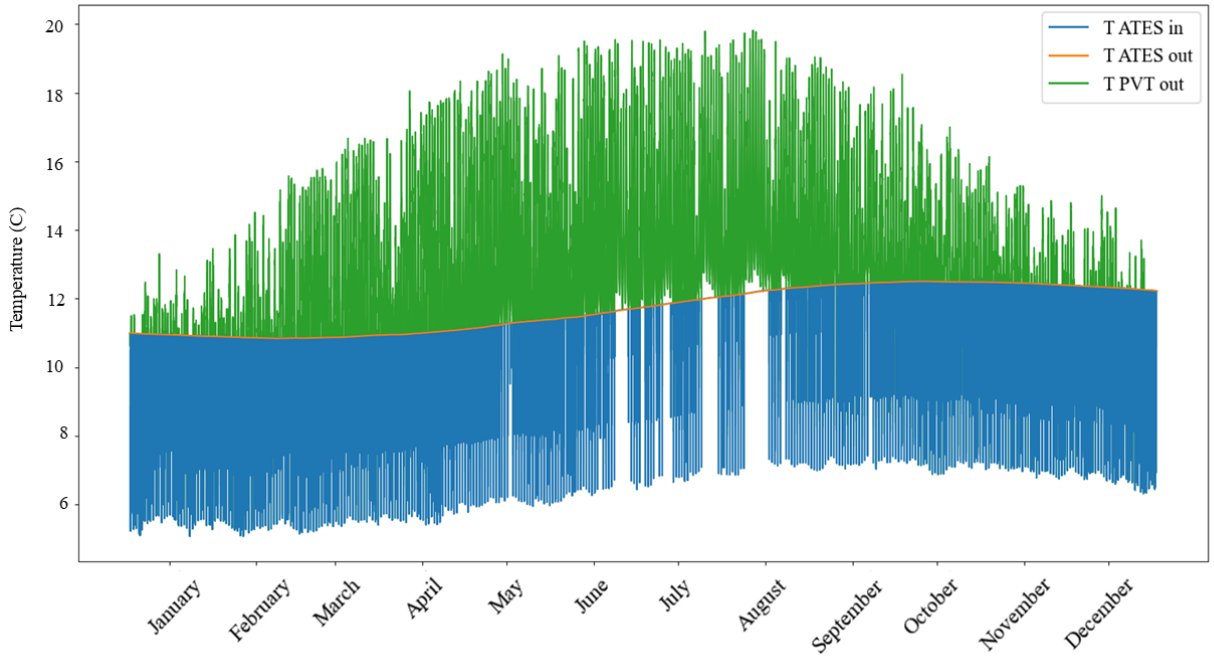

Figure 41: Temperatures district heating network other configuration

The heat transfer dynamics of all components are very similar to the original configuration described in Section 3.1. The main differences arise from temperature variations within the components. The water reaches its highest temperature upon leaving the PVT and entering the ATES, resulting in slightly higher heat loss from the ATES. Generally, the ATES cools the water, leading to a relatively lower temperature entering the building district. Consequently, the heat pumps extract less heat from the district heating network. The cooler district results in lower temperature water entering the PVT, enabling the PVT to deliver more heat to the water. This is shown in Figure 42 and Table 21.

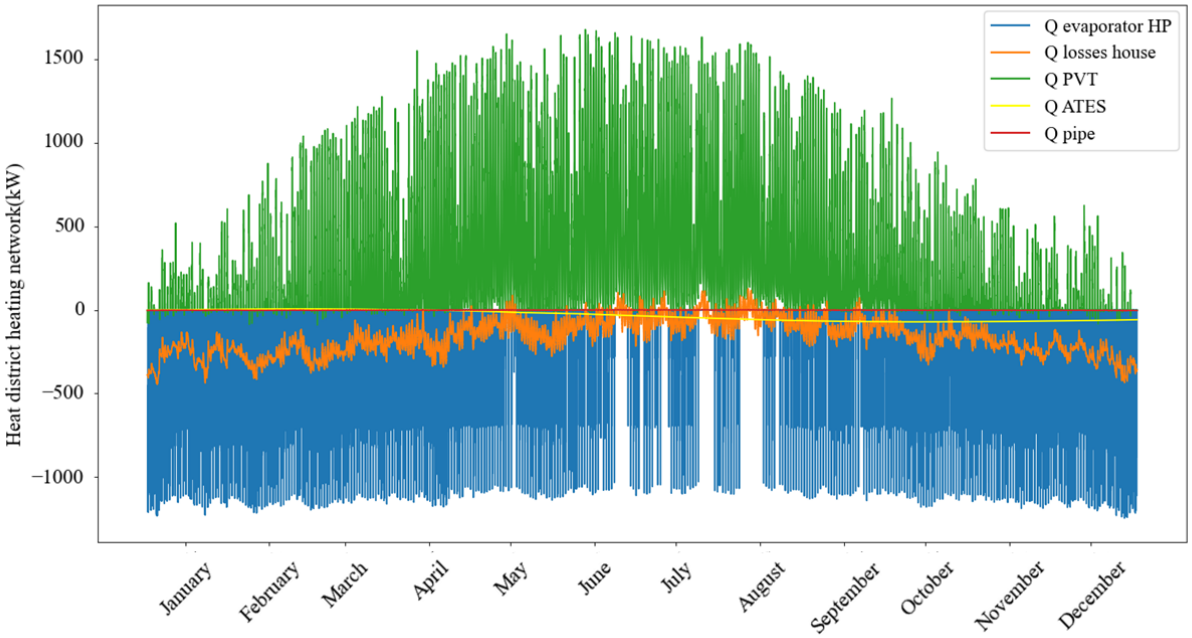

Figure 42: Heat transfer per component other configuration

Table 18: Total heat transfer per component

Result	**Symbol**	**Value [MWh]**
PVT	Q_{PVT}	2543
Losses buildings	Q_{loss}	-1410
Evaporator HP	Q_{evap}	-947.0
ATES loss	$Q_{\text{ATES,loss}}$	-286.8
Pipe losses	$Q_{\text{pipe,loss}}$	-1.705

The power consumption of all components are also very similar to the original configuration described in Section 3.1. The lower heat extraction by the heat pumps causes them to use more power, resulting in a slight increase in overall power consumption. Consequently, the grid usage is higher because the power supply remains the same.

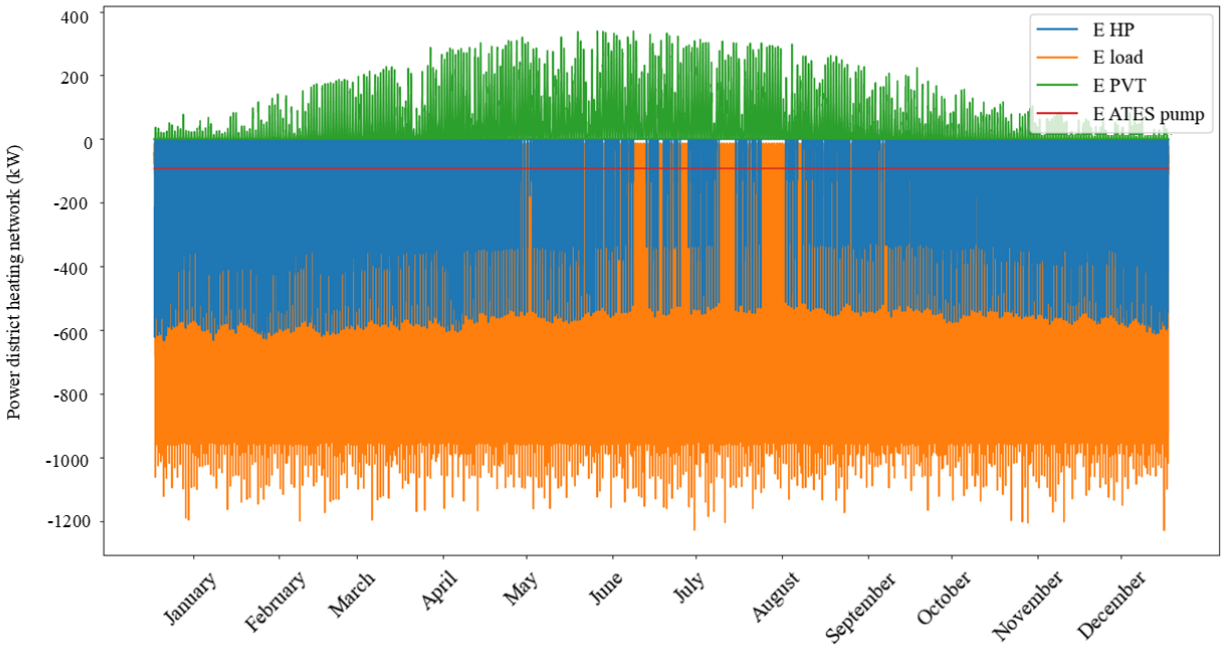

Figure 43: Power per component other configuration

Table 19: Total electrical energy transfer per component

Result	**Symbol**	**Value [MWh]**
PVT	E_{PVT}	393.7
Load buildings	E_{load}	-1120
Heat pump	E_{HP}	-462.0
ATES pump	E_{ATEP}	-805.6
Shortage grid	$E_{\text{grid,shortage}}$	-2032
Surplus grid	$E_{\text{grid,surplus}}$	38.28
Net grid	E_{grid}	-1994

The COP of the heat pumps corresponds to the temperature in the building district. The temperatures are relatively more stable due to the ATES, but also colder. The COP of the heat pumps are thus also lower with lower difference between the pumps. The COP ranges from 2.770 to 3.314.

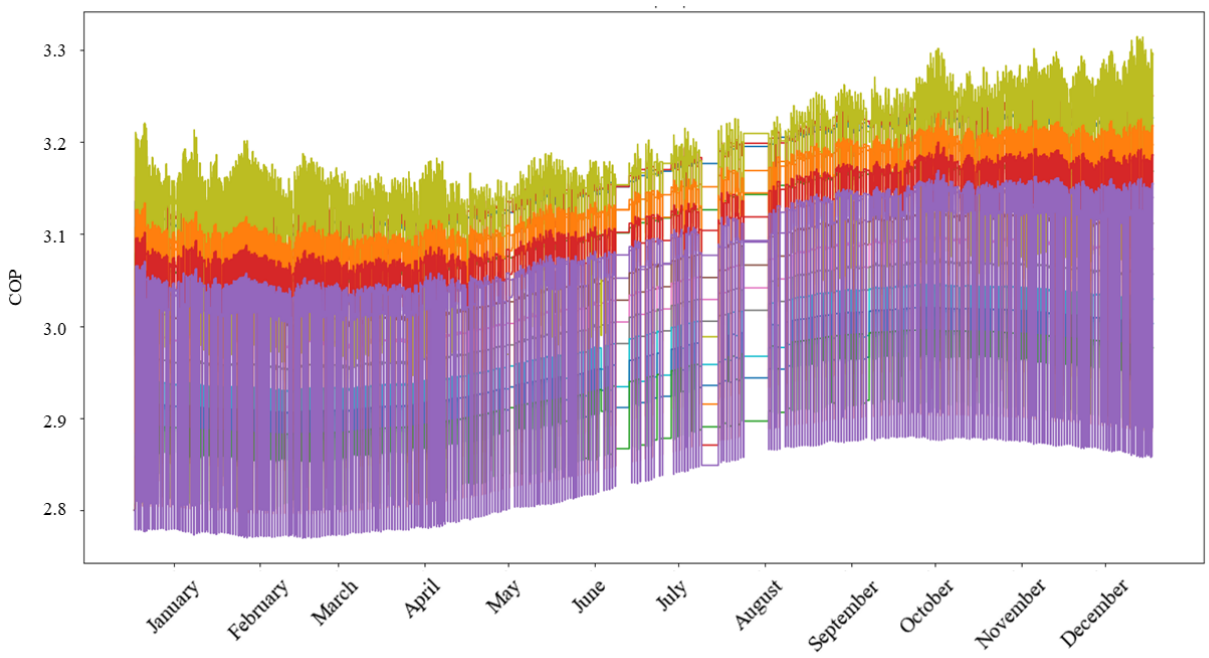

Figure 44: COP heat pumps other configuration

3.4 Results

The findings of this chapter are described next. As discussed in Section 3.2, the benefits of integrating power to storage are minimal, making the installation of an additional heat pump unnecessary. The savings in grid exchange are negligible, and overall power costs are slightly higher. Additionally, installing a cooling network is deemed unnecessary as well. The building temperatures do not exceed levels where cooling would be required, even during extreme summers, given the mild Dutch climate.

From the distribution research, the centralised case was evaluated against the distributed case, leading to two main conclusions. The distributed ATES maintained higher temperatures within the district heating network compared to the centralised case with the same ATES volume. This resulted in higher and more stable water temperatures throughout the district heating network, as the water frequently adopted the aquifer temperature. The increased and stabilised temperatures slightly improved the COP (Coefficient of Performance) of the heat pumps, thereby reducing power consumption. Annually, the power consumption for the centralised case was $E_{HP} = 452.9$ MWh, while the distributed case was $E_{HP} = 440.0$ MWh. However, the distributed case required significantly more power to operate the extra ATES pump units, consuming 805.6 MWh annually per unit. Installing two additional ATES units would cost 1611.2 MWh annually, outweighing the power savings. Therefore, the losses outweigh the benefits in the distributed case, making the centralised case the preferred option for further research.

Lastly, different configurations were evaluated. In the one alternative configuration, water enters the PVT after passing through the building district and before entering the ATES. This setup results in the ATES warming up more, but it does not increase the temperature of the water entering the heat pumps. Consequently, the water temperature entering the district remains relatively stable throughout the year, mirroring the ATES temperature. This leads to an overall lower temperature and reduced COP variance for the heat pumps, ultimately resulting in higher power consumption. Therefore, the configuration where the PVT follows the ATES is maintained, ensuring the highest temperatures are located at the heat pumps.

3.5 Discussion

The results are discussed here, aiming to clarify their significance in the context of the research. The limitations and assumptions of the study are described and the corresponding implications are explained. These limitations are present at both the physics and modeling levels and are discussed for each relevant system component.

Buildings

In this study, the thermodynamics of buildings have been simplified to create a representative building district within the prescribed timeframe. To achieve this, the buildings are first categorised into three different size categories, which are based on the averages of the real planned dimensions of the buildings, though not being the exact sizes. The thermal heat exchange between the buildings and the ambient air is modeled based on conduction, convection, ventilation, and infiltration processes. For conductive and convective heat transfer, the material and thickness of the walls, windows, and roofs are assumed to be identical for each building. The convective heat loss is further influenced by the outside wind speed, which is considered constant throughout the year, as variations are assumed to have a negligible impact on the buildings' thermal behavior. The infiltration exchange relies on basic assumptions regarding the number of windows, doors, wall, and roof surfaces, along with their corresponding average infiltration coefficients. It is noted that more detailed information on the buildings' external properties would be required for more precise infiltration calculations. Meanwhile, ventilation exchange is challenging to approximate accurately due to its strong dependence on human behavior, such as the frequency of opening windows. Consequently, a conservative estimate for ventilation has been chosen for this study.

Some heat exchanges with the buildings and their environment are not taken into account due to their complexity. The heat exchange with the ground is excluded because estimating the ground temperature is considered too complex for this thesis. Unlike ground temperature calculations for district heating, building influence on the ground temperature, including surrounding and deeper ground, adds to the complexity. Another excluded factor is thermal radiation. These calculations require specific orientation of each wall and roof relative to the solar trajectory for each day. Additionally, the exact locations of windows, which would specifically influence heat entry, were unknown. Thus, detailed thermal radiation calculations were considered outside the scope of this thesis. Internal heat sources within buildings, such as heat-producing industries or the number of occupants generating heat, were also not considered due to the lack of data and the complexity of estimation. The uniform temperature preference assumed for each building does not account for individual variations. Furthermore, the thermal capacity of the buildings is simplified, treating each as a block of air with walls, windows, and a roof, ignoring the heat conservation capacity of interiors and multiple rooms. The temperature variations within buildings, such as differences between attics and basements due to convection, were not considered due to the lack of interior details and the complexity of such calculations.

These simplifications and assumptions can affect the thermal behavior of the buildings and thereby the inside temperature. Some simplifications might result in a lower estimated inside temperature than what would be realistic. Factors like thermal radiation, internal heat production, and heat accumulation in the top of the building would add additional heat into specific places in the building. Consequently, these additional considerations could lead to an overall higher building temperature, reducing the heating power required and possibly necessitating cooling.

PVT

For the PVT system, the thermal and electrical power is directly derived from the KNMI irradiance data measured. For a more detailed analysis, the PV topology can be considered, allowing for the electrical current and voltage to be managed by designing the PV system with series of PV strings in parallel, along with appropriate converter, inverter, and cable management. Additionally, the optimal orientation of the modules can be further analysed, considering whether they are placed in portrait or landscape and determining the optimal tilt. A calculation of the effective total irradiance on the PV system using a method used in [39]. Here, an azimuth orientation of the carport with the same direction for each module is considered, including a typical Dutch PV tilt, taking into account the solar trajectory. This revealed that the irradiance was around 90% of the total used for the research. The overall PV generation capability significantly impacts the potential surplus power available for power-to-heat conversion. Additionally, the PVT system's influence on the water temperature entering the system is also crucial. A slight decrease in heat and electricity generation could potentially affect the results.

Control

Within the model, a simple control sequence is embedded. This control system could be made more complex. For instance, the heat pumps could be programmed to react to power pricing, activating when prices are low. Implementing such a response mechanism could enhance the overall economic performance of the system. This could influence the power pricing results used in the power-to-heat analysis.

It is also possible to control the temperature within the ATES or the input of the heat pumps by controlling the mass flow of the thermal carrier. This would also result in a dynamical load for the ATES pump system. Resulting in a different ATES power consumption, which is notably significant and the largest power consumption in distributed scenario. However, this control mechanism was considered too complex and outside the scope of this research.

4 Sizing

The following chapter will investigate the various effects of sizing the components of ATES and PVT systems. The insights from Section 3.4 will determine the chosen setup and configuration of the model.

4.1 Component size analysis

The configuration with centralised ATES before the PVT has been chosen, without additional storage or cooling. Now, the sizes of the PVT and ATES components will be analysed.

An initial series of tests will be conducted, varying the number of PVT modules and the radius of the ATES. The maximum number of PVT modules considered is 800. In this chapter, simulations for configurations with 800 and 600 modules will be conducted. Additionally, the ATES radius will be tested at 100 m, 200 m, and 300 m. The initial configuration of 800 PVT modules and a 250 m radius ATES, already analysed in Chapter 3.1, will be included in the results. For simplicity and to highlight relevant information, only the the temperatures of the district heating network and the total heat and power supply and consumption are presented.

First, the temperatures of the district heating system are shown in the graphs below for the different sizes. Where R is the radius of the ATES and n the number of PVT modules installed.

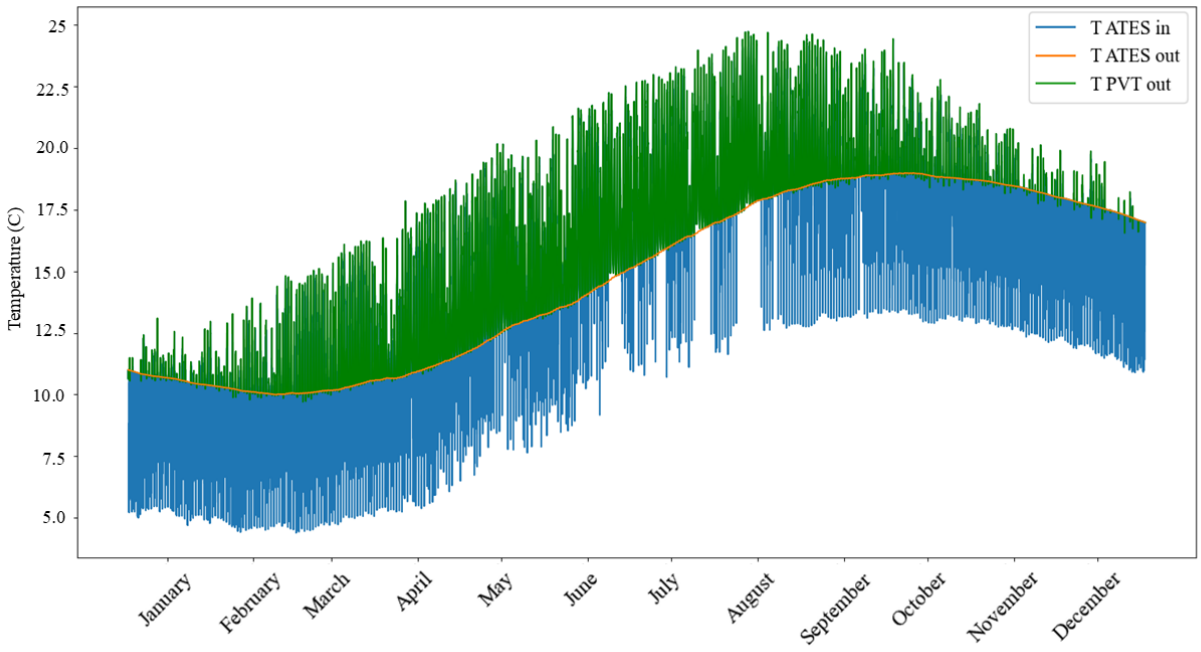

Figure 45: Temperatures: R = 100 m, n = 600

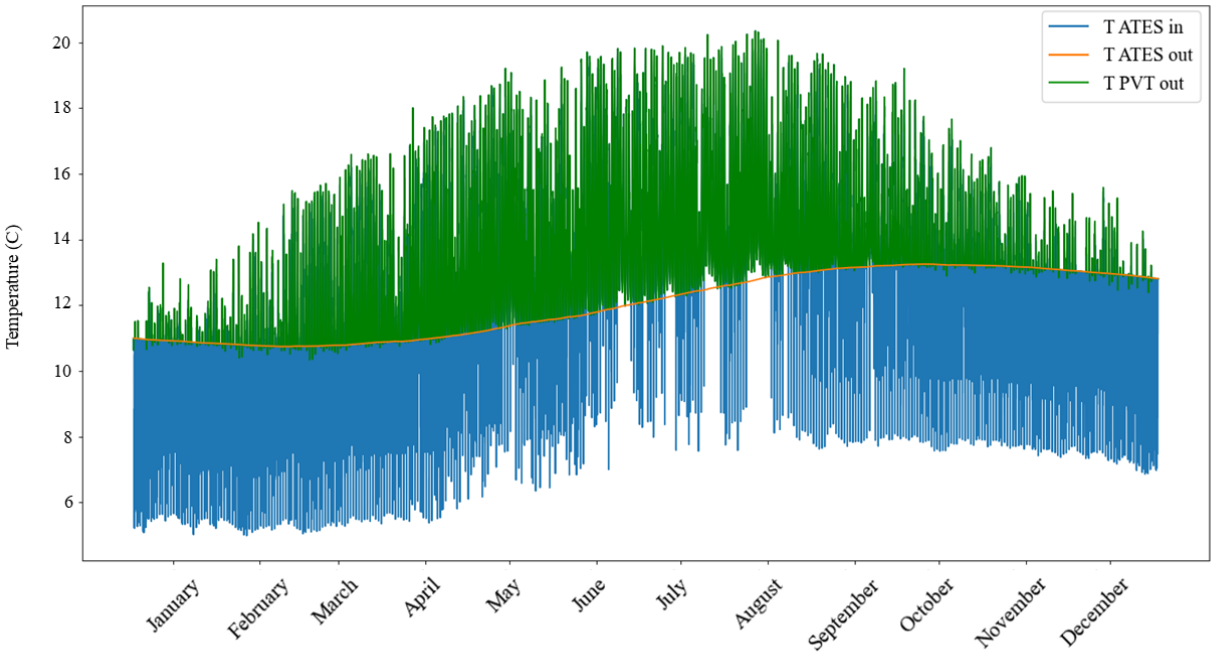

Figure 46: Temperatures: R = 200 m, n = 600

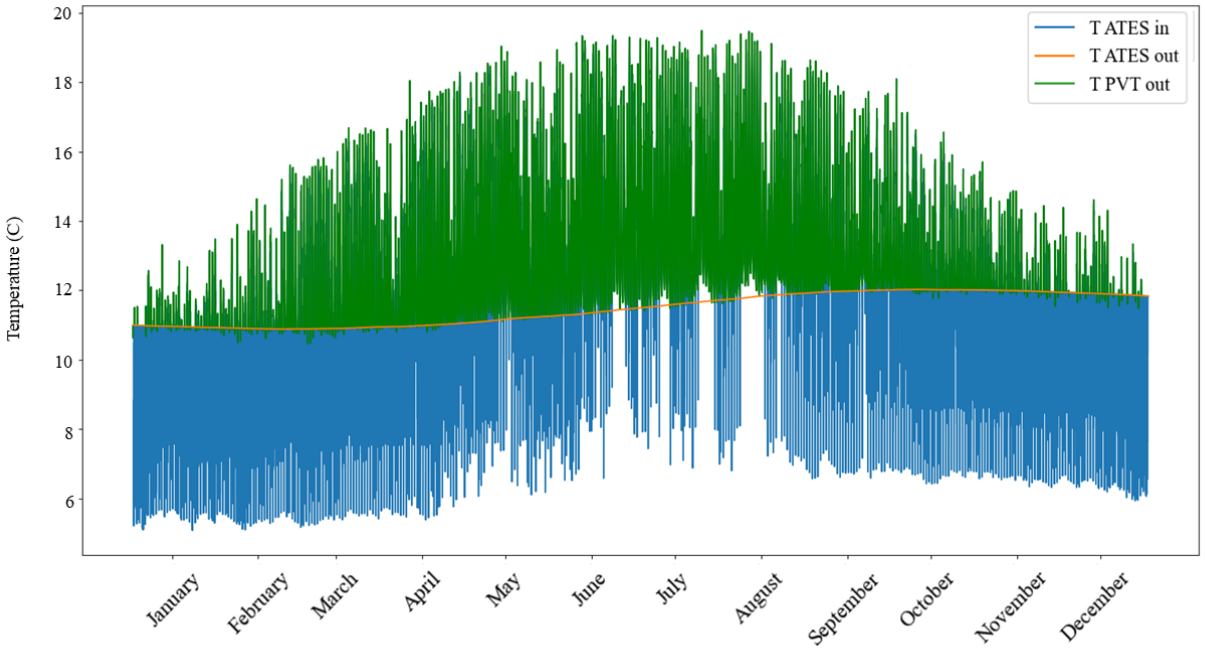

Figure 47: Temperatures: R = 300 m, n = 600

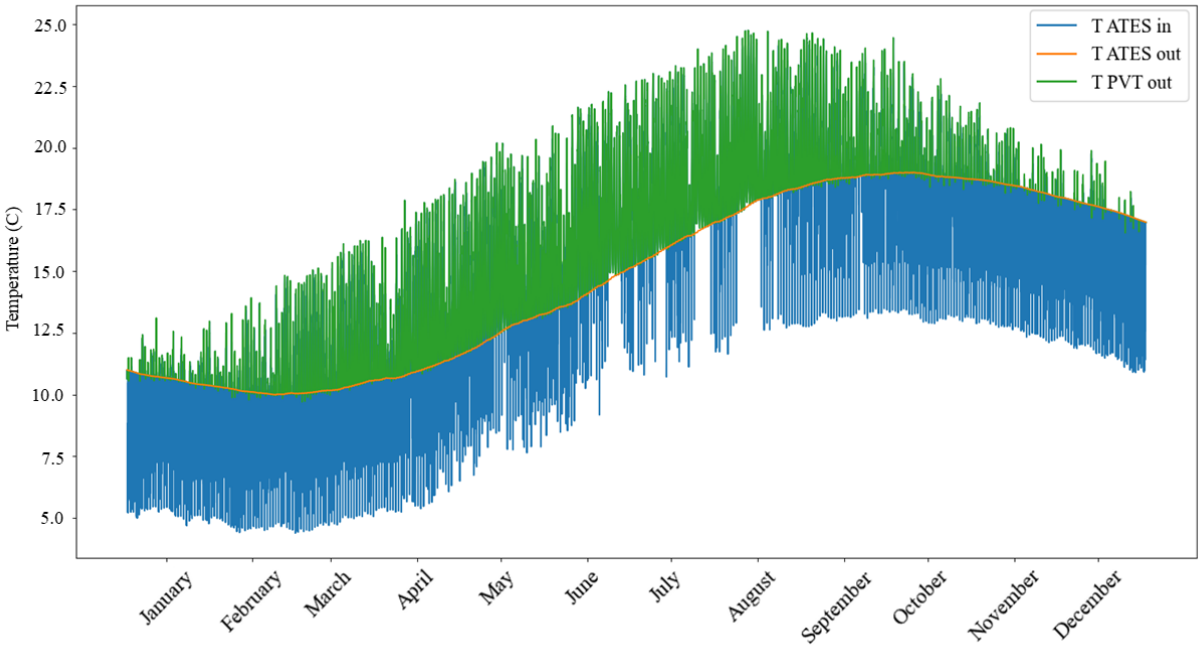

Figure 48: Temperatures: R = 100 m, n = 800

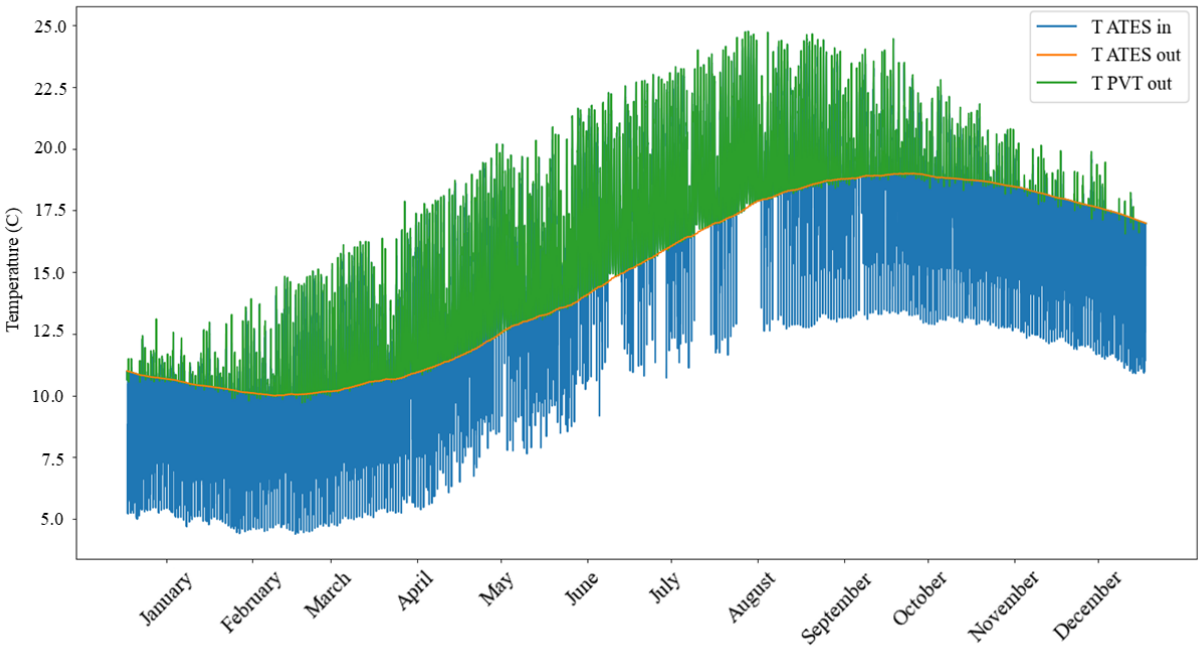

Figure 49: Temperatures: R = 200 m, n = 800

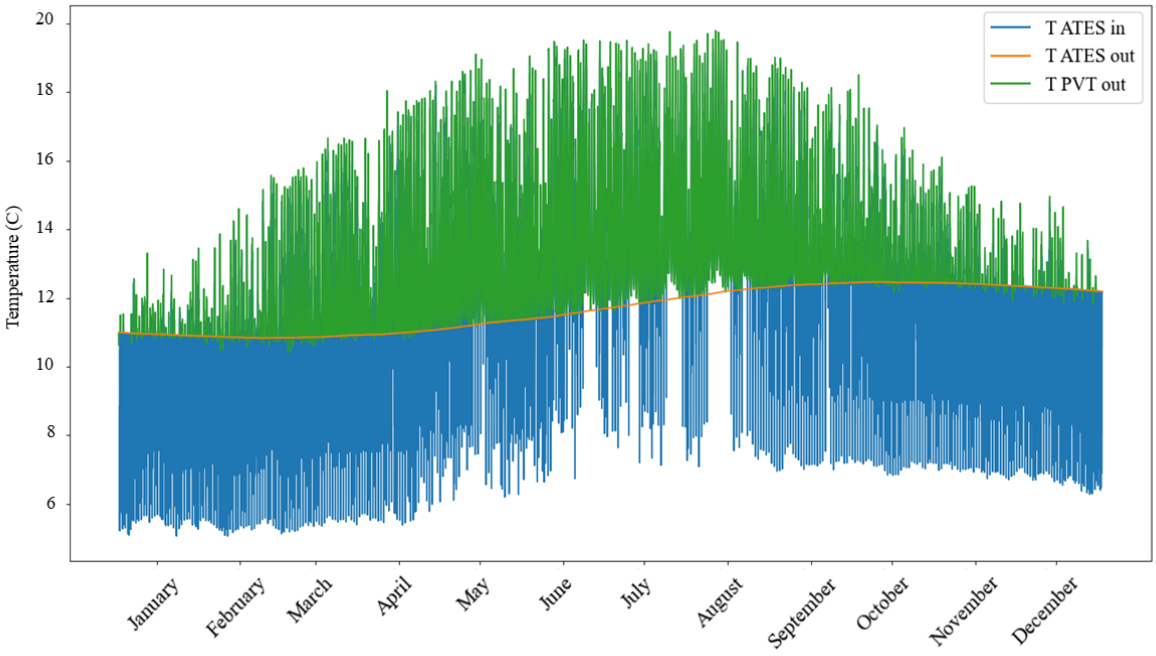

Figure 50: Temperatures: R = 250 m, n = 800

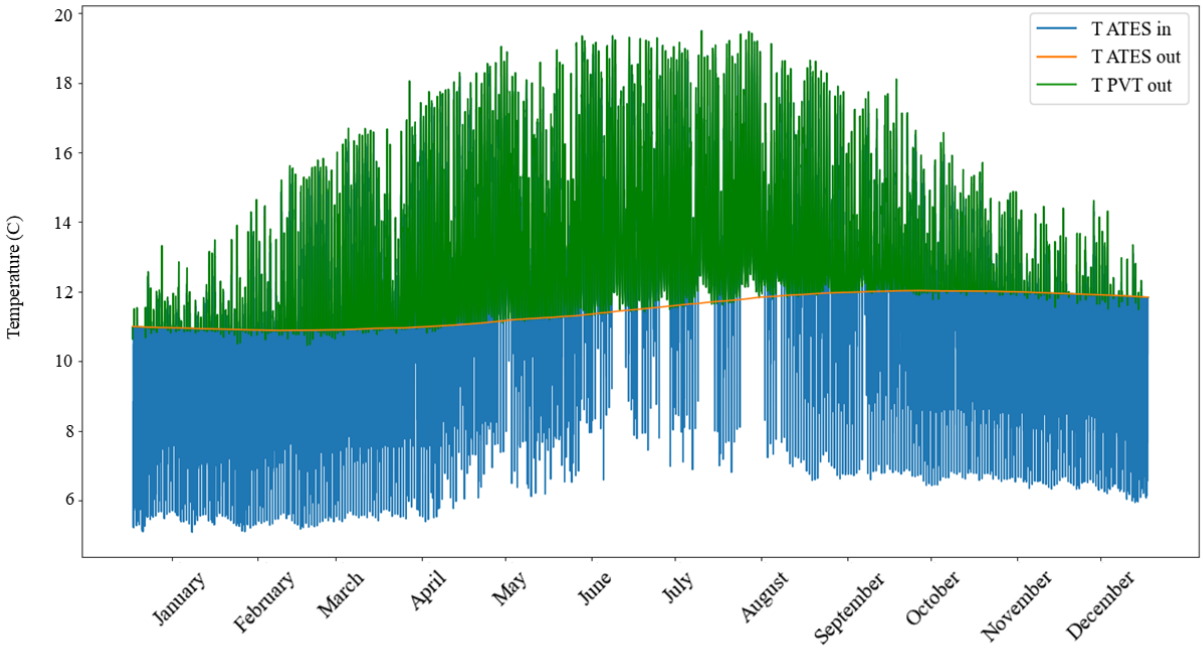

Figure 51: Temperatures: R = 300 m, n = 800

Next, The following tables display the total heat transfer amounts for the components across the various size scenarios.

Table 20: Total thermal energy transfer: R = 100 m, n = 600

Result	**Symbol**	**Value [MWh]**
PVT	Q_{PVT}	2244
Losses buildings	Q_{loss}	-1410
Evaporator HP	Q_{evap}	-975.6
ATES loss	$Q_{\text{ATES,loss}}$	-243.5
Pipe losses	$Q_{\text{pipe,loss}}$	-7.455

Table 21: Total thermal energy transfer: R = 100 m m, n = 800

Result	**Symbol**	**Value [MWh]**
PVT	Q_{PVT}	2247
Losses buildings	Q_{loss}	-1410
Evaporator HP	Q_{evap}	-975.7
ATES loss	$Q_{\text{ATES,loss}}$	-244.3
Pipe losses	$Q_{\text{pipe,loss}}$	-7.473

Table 22: Total thermal energy transfer: R = 200 m, n = 600

Result	**Symbol**	**Value [MWh]**
PVT	Q_{PVT}	2465
Losses buildings	Q_{loss}	-1410
Evaporator HP	Q_{evap}	-959.0
ATES loss	$Q_{\text{ATES,loss}}$	-272.0
Pipe losses	$Q_{\text{pipe,loss}}$	-3.981

Table 23: Total thermal energy transfer: R = 200 m, n = 800

Result	**Symbol**	**Value [MWh]**
PVT	Q_{PVT}	2469
Losses buildings	Q_{loss}	-1410
Evaporator HP	Q_{evap}	-959.0
ATES loss	$Q_{\text{ATES,loss}}$	-272.9
Pipe losses	$Q_{\text{pipe,loss}}$	-3.989

Table 24: Total thermal energy transfer: R = 250 m, n = 800

Result	**Symbol**	**Value [MWh]**
PVT	Q_{PVT}	2504
Losses buildings	Q_{loss}	-1410
Evaporator HP	Q_{evap}	-956.0
ATES loss	$Q_{\text{ATES,loss}}$	-277.1
Pipe losses	$Q_{\text{pipe,loss}}$	-3.520

Table 25: Total thermal energy transfer: R = 300 m, n = 600

Result	**Symbol**	**Value [MWh]**
PVT	Q_{PVT}	2518
Losses buildings	Q_{loss}	-1410
Evaporator HP	Q_{evap}	-954.3
ATES loss	$Q_{\text{ATES,loss}}$	-278.7
Pipe losses	$Q_{\text{pipe,loss}}$	-3.253

Table 26: Total thermal energy transfer: R = 300 m, n = 800

Result	**Symbol**	**Value [MWh]**
PVT	Q_{PVT}	2523
Losses buildings	Q_{loss}	-1410
Evaporator HP	Q_{evap}	-954.4
ATES loss	$Q_{\text{ATES,loss}}$	-279.6
Pipe losses	$Q_{\text{pipe,loss}}$	-3.259

Lastly, The following tables display the total electrical energy usage or supply amounts for the components for the size scenarios.

Table 27: Total electrical energy transfer: R = 100 m, n = 600

Result	Symbol	Value [MWh]
PVT	E_{PVT}	295.2
Load buildings	E_{load}	-1120
Heat pump	E_{HP}	-433.4
ATES pump	E_{ATEP}	-805.6
Shortage grid	$E_{\text{grid,shortage}}$	-2075
Surplus grid	$E_{\text{grid,surplus}}$	10.94
Net grid	E_{grid}	-2064

Table 28: Total electrical energy transfer: R = 100 m, n = 800

Result	Symbol	Value [MWh]
PVT	E_{PVT}	393.7
Load buildings	E_{load}	-1120
Heat pump	E_{HP}	-433.3
ATES pump	E_{ATEP}	-805.6
Shortage grid	$E_{\text{grid,shortage}}$	-2004
Surplus grid	$E_{\text{grid,surplus}}$	38.47
Net grid	E_{grid}	-1965

Table 29: Total electrical energy transfer: R = 200 m, n = 600

Result	Symbol	Value [MWh]
PVT	E_{PVT}	295.2
Load buildings	E_{load}	-1120
Heat pump	E_{HP}	-450.0
ATES pump	E_{ATEP}	-805.6
Shortage grid	$E_{\text{grid,shortage}}$	-2091
Surplus grid	$E_{\text{grid,surplus}}$	10.93
Net grid	E_{grid}	-2081

Table 30: Total electrical energy transfer: R = 200 m, n = 800

Result	Symbol	Value [MWh]
PVT	E_{PVT}	393.7
Load buildings	E_{load}	-1120
Heat pump	E_{HP}	-450.0
ATES pump	E_{ATEP}	-805.6
Shortage grid	$E_{\text{grid,shortage}}$	-2021
Surplus grid	$E_{\text{grid,surplus}}$	38.46
Net grid	E_{grid}	-1982

Table 31: Total electrical energy transfer: R = 250 m, n = 800

Result	Symbol	Value [MWh]
PVT	E_{PVT}	393.7
Load buildings	E_{load}	-1120
Heat pump	E_{HP}	-452.9
ATES pump	E_{ATEP}	-805.6
Shortage grid	$E_{\text{grid,shortage}}$	-2023
Surplus grid	$E_{\text{grid,surplus}}$	38.46
Net grid	E_{grid}	-1985

Table 32: Total electrical energy transfer: R = 300 m, n = 600

Result	Symbol	Value [MWh]
PVT	E_{PVT}	295.2
Load buildings	E_{load}	-1120
Heat pump	E_{HP}	-454.6
ATES pump	E_{ATEP}	-805.6
Shortage grid	$E_{\text{grid,shortage}}$	-2096
Surplus grid	$E_{\text{grid,surplus}}$	10.93
Net grid	E_{grid}	-2085

Table 33: Total electrical energy transfer: R = 300 m, n = 800

Result	Symbol	Value [MWh]
PVT	E_{PVT}	393.7
Load buildings	E_{load}	-1120
Heat pump	E_{HP}	-454.6
ATES pump	E_{ATEP}	-805.6
Shortage grid	$E_{\text{grid,shortage}}$	-2025
Surplus grid	$E_{\text{grid,surplus}}$	38.46
Net grid	E_{grid}	-1987

When altering the sizes of the PVT and ATES systems, several observations come up. Increasing the number of PVT consistently results in higher heat and electricity production, thereby enhancing overall system performance without any additional downsides. Conversely, reducing the size of the ATES leads to a warmer network, which decreases the power consumption of heat pumps due to a higher COP. However, it also causes more temperature divergence within the system and increases losses in the ATES and pipes, and decreases heat provided by the PVT. A warmer network reduces heat pump power consumption, which is the only power

variable affected by the dimensions of the ATES. Consequently, a smaller ATES results in lower net power use. The net grid exchange is considered the best result for monitoring system performance. An overview of the different dimensions and resulting net grid exchange is shown in Table 34.

Table 34: Total net grid exchange per size

ATES R [m]	**n modules**		**Unit**
	600	**800**	
100	-2064	-1965	MWh
200	-2081	-1982	MWh
250	-2083	-1985	MWh
300	-2085	-1987	MWh

4.2 Long term operation analysis

It is observed that overall temperatures rise during the year within the aquifer and the system, especially for smaller dimension aquifers, this is shown in Figure 52. The starting temperature for the measurements was set at 11°C, but the real starting temperature each year will be higher due to the cumulative temperature increase. For larger ATES sizes, the surrounding soil has a greater influence than the district heating network, leading to temperature profiles that more closely resemble those of the soil. This results in relatively low heat exchange with the soil. In contrast, smaller ATES sizes, which operate at higher temperatures, experience increased heat losses. As these losses grow, it becomes increasingly difficult for the district heating network to maintain the desired higher operating temperatures.

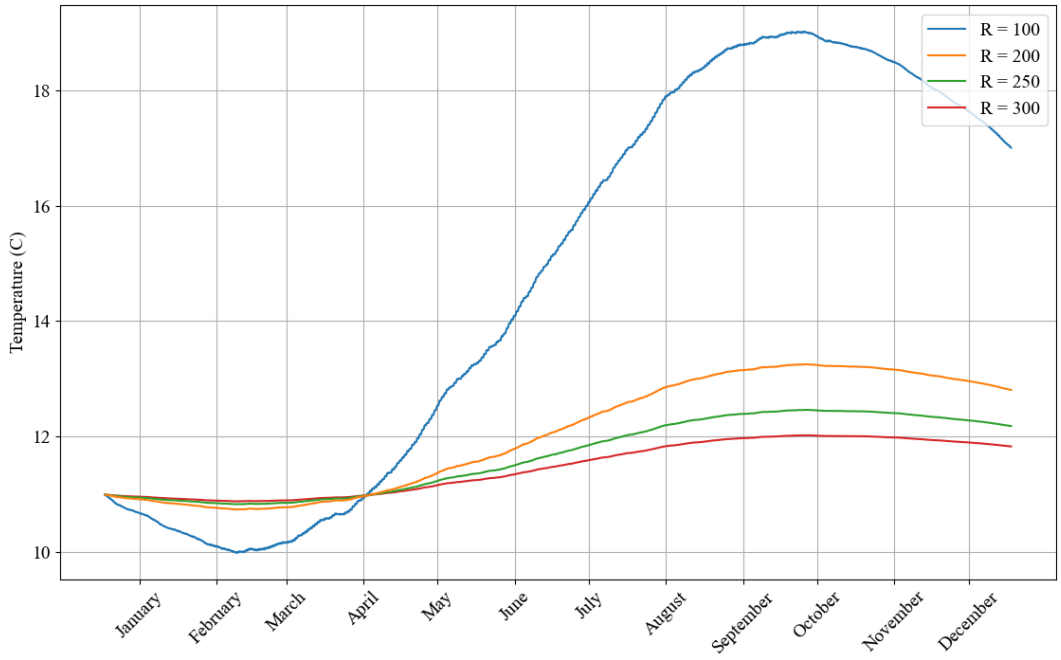

Figure 52: Rising temperatures ATES

Consequently, for each ATES size, the operating temperature should converge to a specific level. To account for this, the model has simulated the ATES temperature after five years of operation with 800 PVT modules and different ATES sizes. Due to the duration of the simulations, the step size was increased from 15 minutes to one hour. Because the performance was relatively best for ATES with a radius of 100 meters, smaller ATES sizes are also taken into account.

The ATES temperatures after five years of operation are shown in Figure 53. The temperatures of smaller ATES systems are higher but exhibit greater temperature divergence throughout the seasons. In most cases, the temperature continues to rise after the fifth year. Since this depends on the season, a temperature differential (ΔT) with a maximum of 1°C is considered stable. Although a smaller divergence would be preferable, the results are influenced by weather conditions, which can vary annually.

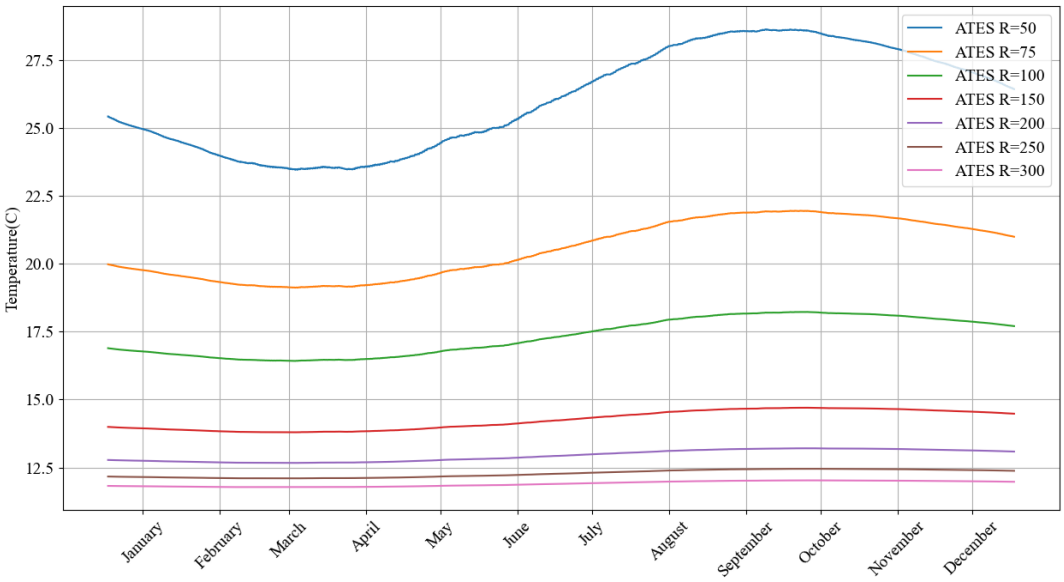

Figure 53: Temperatures ATES after 5 years in operation, one hour timestep

Not all ATES sizes achieved a stable temperature difference of 1°C after 5 years. Therefore, the final temperatures obtained from the 5-year simulations with a one-hour timestep will be used as the starting temperatures for a continuing simulation for additional years. Results have shown variations when comparing simulations with a one-hour timestep to those with a 15-minute timestep. Overall outputs can differ when the resolution is altered, and the control of the system is less responsive. To eliminate these errors, the continuing simulation for additional years will use the original 15-minute timestep until the temperature difference is less than 1°C, ensuring the most accurate steady-state temperature values for the different ATES sizes. The steady-state temperatures for different ATES sizes are shown in Figure 54. The corresponding net grid exchanges are summarised in Table 35.

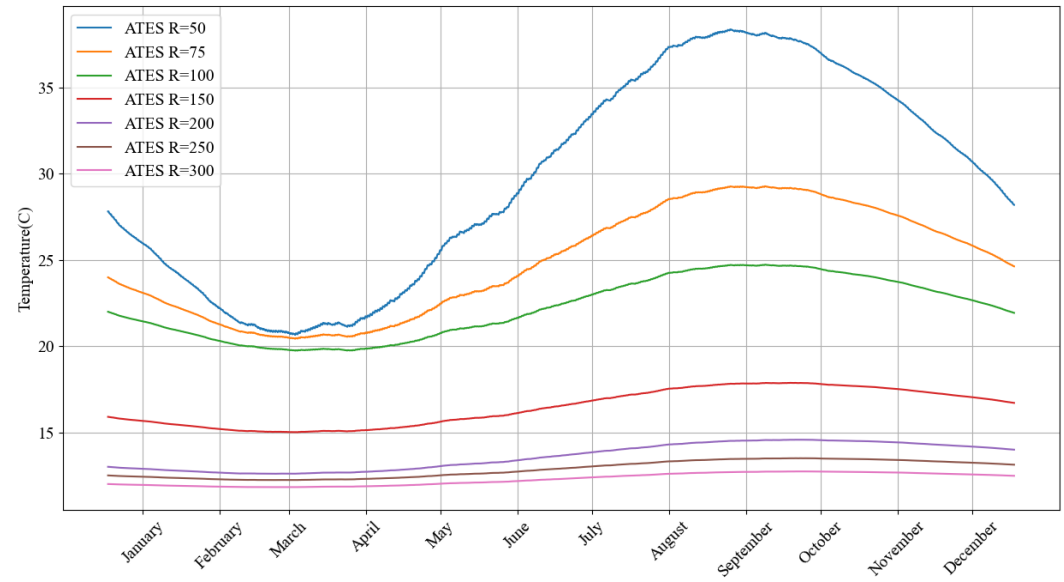

Figure 54: Temperatures ATES at steady state, 15-minute timestep

Table 35: Total net grid exchange for steady state

ATES R(m)	n modules	T_0(°C)	Net grid(MWh)
35	800	27.4	-1928
50	800	27.8	-1923
75	800	24.0	-1922
100	800	22.0	-1924
125	800	18.0	-1931
150	800	15.9	-1942
200	800	13.0	-1966
250	800	12.5	-1973
300	800	12.0	-1978

A smaller ATES can heat up more, increasing the heat pump's COP, but the temperatures will fluctuate more throughout the seasons. This indicates a much larger weather dependency on the overall stability of the aquifer temperatures. An aquifer that is too small can lead to too extreme temperatures. An example is shown in Figure 55. Here, an ATES with a radius of 25 meters is modeled under the same conditions.

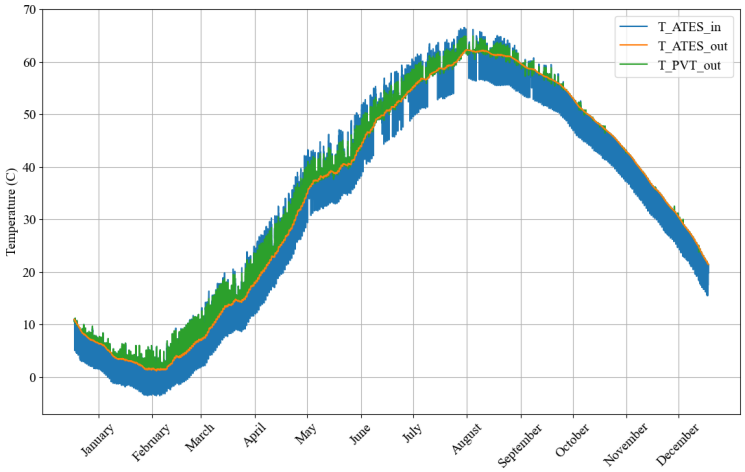

Figure 55: Temperatures ATES at steady state with a radius of 25 meters

4.3 Results

The sizing analysis has given the following results. Increasing the number of PVT modules until the maximum of 800 enhances both electrical and thermal generation, thereby improving overall system performance without direct drawbacks. A larger ATES unit helps maintain a more stable temperature gradient throughout the year, though it operates at lower temperatures, whereas smaller volume aquifers experience greater temperature fluctuations.

The variable net power consumption depends primarily on the heat pumps and their corresponding COP. Due to the maximum operational COP of the heat pumps, there exists an optimal boundary temperature, around 19.5°C, at which they function most efficiently. Thus, the objective is to maintain the inlet temperature (T_{in}) for each heat pump as close to this optimal temperature as possible across all seasons. Operating at higher temperatures results in increased heat losses. Smaller ATES units, with higher operating temperatures, can experience excessively low temperatures during winter, as illustrated in Figure 54 and Figure 55. Therefore, a balance must be struck between maintaining the correct operating temperature, minimising heat losses, and managing seasonal temperature fluctuations.

4.4 Discussion

These results are be discussed in this section. The limitations and assumptions of relevant components are described with the corresponding influences on the results.

ATES

The thermodynamics of the ATES system are simplified in this research, which can alter the results compared to a real ATES. In this model, the aquifer is considered perfectly mixed, meaning the temperature of the output from the ATES is always the average temperature within the aquifer. This assumption ignores the placement of the inlets and outlets, which in reality would create a temperature profile affecting the output temperature. Additionally, the sand-water ratio within the aquifer is assumed to be uniform, although in reality, variations in this ratio can impact thermal properties. The model also assumes that the water in the aquifer remains stationary, despite it actually moving approximately 20 m per year towards the ocean. This slow movement, translating to about 5 cm per day, is considered negligible and is thus not accounted for. Furthermore, the aquifer is modeled as a disc-shaped ATES, whereas a real aquifer would have a more natural and potentially irregular shape, affecting its thermodynamic behavior. Lastly, the aquifer is simplified to a single ATES tank instead of a doublet system consisting of separate warm and cold water wells. In this research, a potential cold water well would be redirected to the warm water well without additional heat, so it is expected to yield similar results when focusing solely on the warm water well. These simplifications might result in deviations from real-world performance, potentially impacting the accuracy of the thermal behavior predictions for the ATES system.

Electrical components

The electrical flow of all electrical assets is simplified in the form of a simple generation and load with resulting grid exchange for each time interval. The electronics within the model are an input and result of the thermodynamics of the system. In this context, PV generation is primarily dependent on the input weather data and slightly dependent on the temperature of the water flowing through the PV. The load from the building and ATES pump are simply input data, whereas the heat pump load is a direct result of the system's thermodynamics, thereby influencing the final grid exchange. The electrical simplification does not account for some important electrical components such as DC-DC converters, DC-AC inverters, charge controllers, diodes, and cables. The efficiency of these components can contribute to additional power losses, potentially leading to a higher overall grid load in reality. However, estimating whether the relative sizing of the ATES and PVT would significantly alter these electrical losses, and thus overall results, remains uncertain.

Conditions

The inputs for the model are based on conditions from a single year. This includes weather conditions such as ambient temperature and irradiance, as well as power prices used in the power-to-heat storage analysis. Additionally, the building load data was created once and is consistently applied across all different configurations. In reality, these inputs vary over time, so a reference case is used to provide a most representative scenario. Exploring different scenarios for these inputs could strengthen the research by yielding results that are more resilient to varying conditions.

5 Optimisation

In this chapter, the system's sizes to minimise CO_2 emissions will be optimised. These emissions are directly correlated with the power drawn from the grid for system operation and the emissions from component installation. The target is to develop an optimisation problem that aims to minimise CO_2 emissions. The variables in this function will include the number of PVT modules and the sizes of the ATES units. Constraints will be based on the available area and the results of the component size analysis. Where the findings from Section 4.3 are used for further analysis.

5.1 CO_2 emissions

To minimise CO_2 emissions, we need to quantify both the installation and operational phases of the system in a common unit: equivalent kg CO_2. For operational CO_2 emissions, we will use data from Nowtricity [40], which provides monthly average grams of CO_2 equivalent per kWh for power generated in the Netherlands. By multiplying these values by the system's grid power usage for each corresponding month, we can calculate the system's operational CO_2 emissions. The monthly average kg CO_2 equivalent per kWh emissions are illustrated in Figure 56.

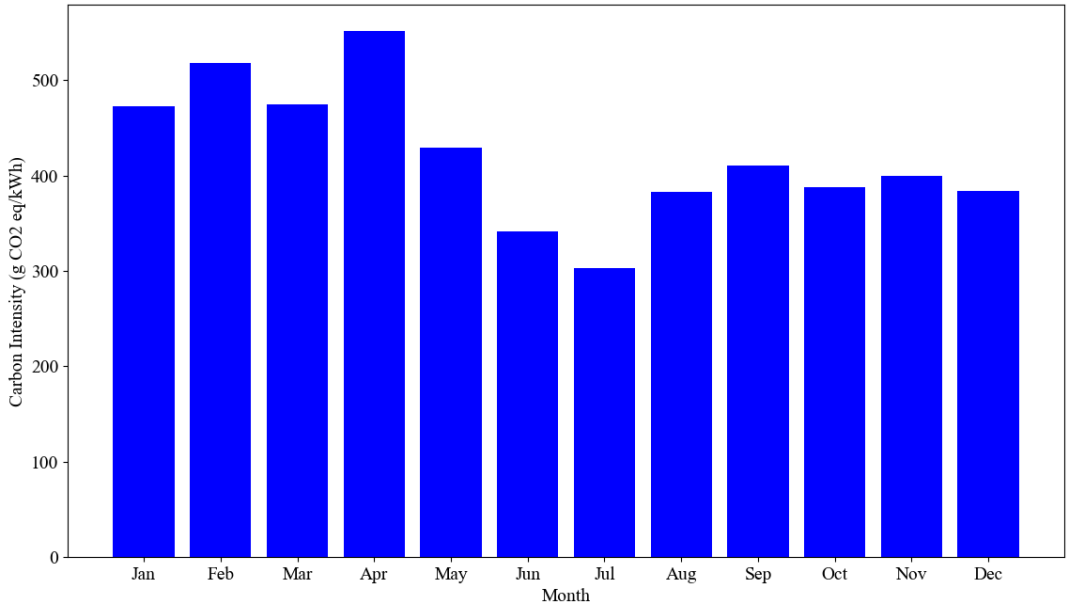

Figure 56: Monthly average CO_2 intensities Netherlands power generation 2022

Then, the carbon emissions for the variable component installation must be determined. By integrating this data, an estimation of CO_2 emissions associated with the variable components PVT and ATES can be quantified. The carbon emissions for the PVT are primarily dependent on the emissions resulting from the manufacturing of the modules. Estimations for PV modules, expressed in grams of CO_2 equivalent, take into account the entire lifecycle, including manufacturing and electricity generation. According to a study by Virtuani [41], the CO_2 emissions for PV modules in the Netherlands, considering the local climate, are estimated at 40.1 g CO_2eq/kWh for optimally tilted modules. Since this intensity factor pertains only to the PV part of the PVT, it will be multiplied by the electricity generation of the PVT to quantify its carbon emissions.

The installation emissions of the ATES are challenging to quantify scaled to the size of the aquifer. Research into the emissions of the ATES shows that they are largely dependent on the operation of the system [42]. However, a case study in the Netherlands has documented the amount of diesel used for constructing an ATES well, which is determined to be 3,250 liters [42]. By using the CO_2 emission factor of 2.68 kg/L for diesel, the

construction of an ATES well results in 8,710 kg of CO_2 emissions. Over an estimated lifetime of 30 years, this annual CO_2 emission is negligible for the optimisation problem.

5.2 Optimisation problem

To optimise the sizes of the PVT and ATES systems for minimal CO_2 emissions, an optimisation function will be developed. The total CO_2 emissions will include both the operational emissions of the system and the installation emissions of the PVT modules. The installation emissions of the ATES are excluded as they are considered negligible. The equation for the total emissions is expressed as follows:

$$CO_2e_{\text{total}}(n, R) = E_{\text{op}}(n, R, T_0) + E_{\text{inst}}(n, R, T_0) \tag{88}$$

$$CO_2e_{\text{op}}(n, R) = a \times P_{\text{G}}(n, R, T_0)$$

$$CO_2e_{\text{inst}}(n) = b \times P_{\text{PV}}(n, R, T_0)$$

Here, CO_2e_{total} represents the total CO_2 emissions, CO_2e_{op} the operational CO_2 emissions, and CO_2e_{inst} is the installation CO_2 emissions. The variables n and R correspond to the number of PVT modules and the ATES radius, respectively. The initial operational temperature of each ATES size is expressed as T_0. The kg CO_2 equivalent per kWh of grid consumption is expressed as a, with these values illustrated in Figure 56. The kg CO_2 equivalent per kWh of PV generation is expressed as b, which is set at 40.1 g CO_2eq/kWh. P_{G} and P_{PV} represent the power consumption from the grid and the power generation by the PVT modules, respectively.

Next, the constraints for the variables in the optimisation function must be determined. The number of PVT modules (n) will be analysed within the range of 700 to 800 modules. Sizing analysis has shown that increasing the number of solar modules up to the maximum enhances the system's performance, with the carport's maximum capacity being 800 modules. To assess the significance of installation emissions, a range of 700 to 800 modules is chosen for analysis.

For the ATES size, expressed as the radius R, it has been shown that net power grid consumption is lowest for an ATES radius of 75 m. Similarly low net grid power consumption results were observed for ATES radii of 50 m and 100 m. Therefore, the CO_2 emissions will be analysed for ATES radii between 50 m and 100 m, with a median value of 75 m. The solution to the problem will be calculated discretely. The resolution will be set at 10 PVT modules and 5 m for the ATES radius. This approach allows for the creation of an eleven by eleven matrix representing the total emissions for each variable combination. The optimisation problem is formulated as follows:

Minimise

$$CO_2e_{\text{total}}(n, R, T_0) = a \times P_{\text{G}}(n, R, T_0) + b \times P_{\text{PV}}(n, R, T_0)$$

Subject to

$$700 \leq n \leq 800$$

$$50 \leq R \leq 100$$

As the radii of the ATES will change to solve the problem, a specific initial operational temperature for each ATES size needs to be determined, as discussed in Chapter 4. The known stable operating temperatures are plotted in Graph 57, and a polynomial trendline is fitted through the data. For each ATES radius between 50 m and 100 m, with a step of 5 m, a corresponding operating temperature is determined along the trendline, as shown in Table 44.

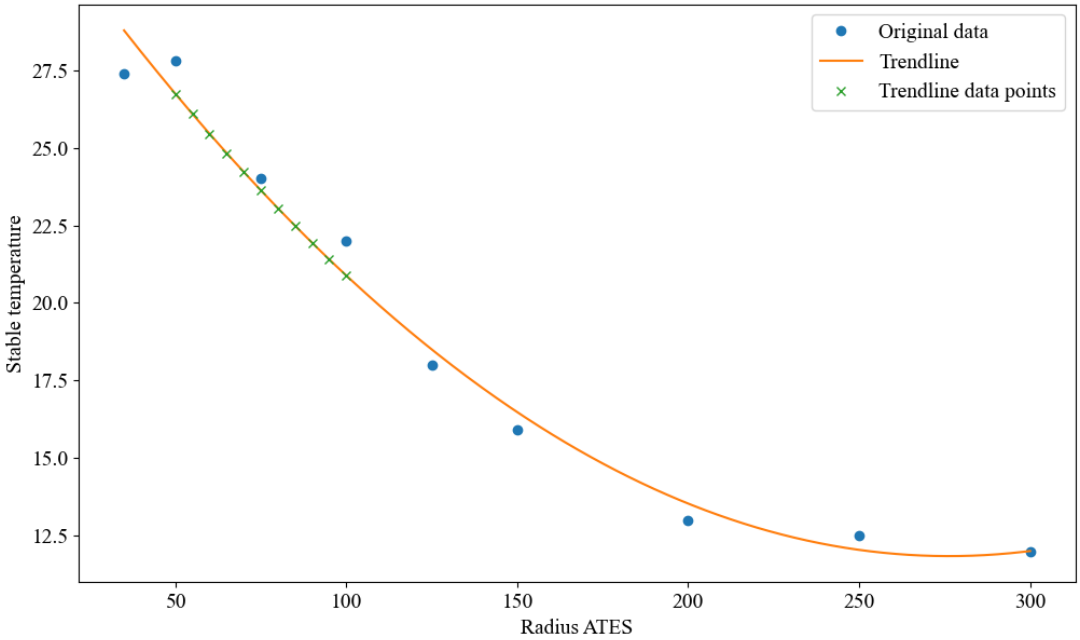

Figure 57: Operating temperature trendline for different ATES radii

ATES Radius [m]	50	55	60	65	70	75	80	85	90	95	100
Operating Temperature [°C]	26.7	26.1	25.5	24.8	24.2	23.6	23.1	22.5	21.9	21.4	20.9

Table 36: Operating temperatures for different ATES radii

5.3 Results

The total CO_2 emissions for all measured sizes are illustrated in Figure 58. It is clear that the optimal solution for minimising CO_2 emissions is achieved with the maximum number of PVT modules, which is 800. This indicates that the operational CO_2 emissions of the entire system are more significant than the installation emissions of the PVT modules. The configuration with the lowest CO_2 emissions features a 60-meter ATES radius and 800 solar modules. However, the difference between this and other configurations is minimal; a deviation of 5 m from the 60 m ATES radius results in only a 10 kg CO_2 equivalent change.

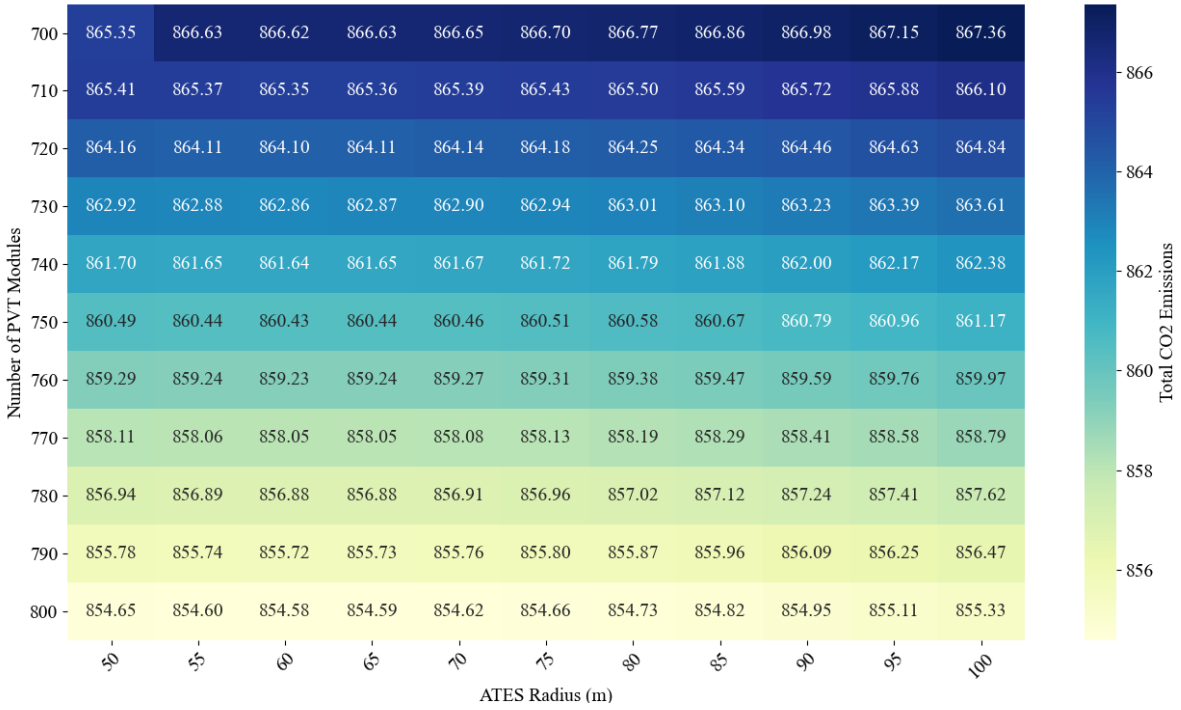

Figure 58: Total CO2 Emissions for Different PVT Modules and ATES Radii

To obtain a more specific value as the optimal solution, additional boundaries are set for the problem. First, a maximum temperature for the ATES is established. Since ATES systems can affect the subsurface, the injected water cannot be too hot. The maximum injection temperature in the ATES can range from 25°C to 30°C [43]. The Following Figures 59 and 60 show the configurations that exceed the threshold temperature, with one case at 30°C and the other at 25°C. The configurations exceeding the maximum temperature have a shade of grey.

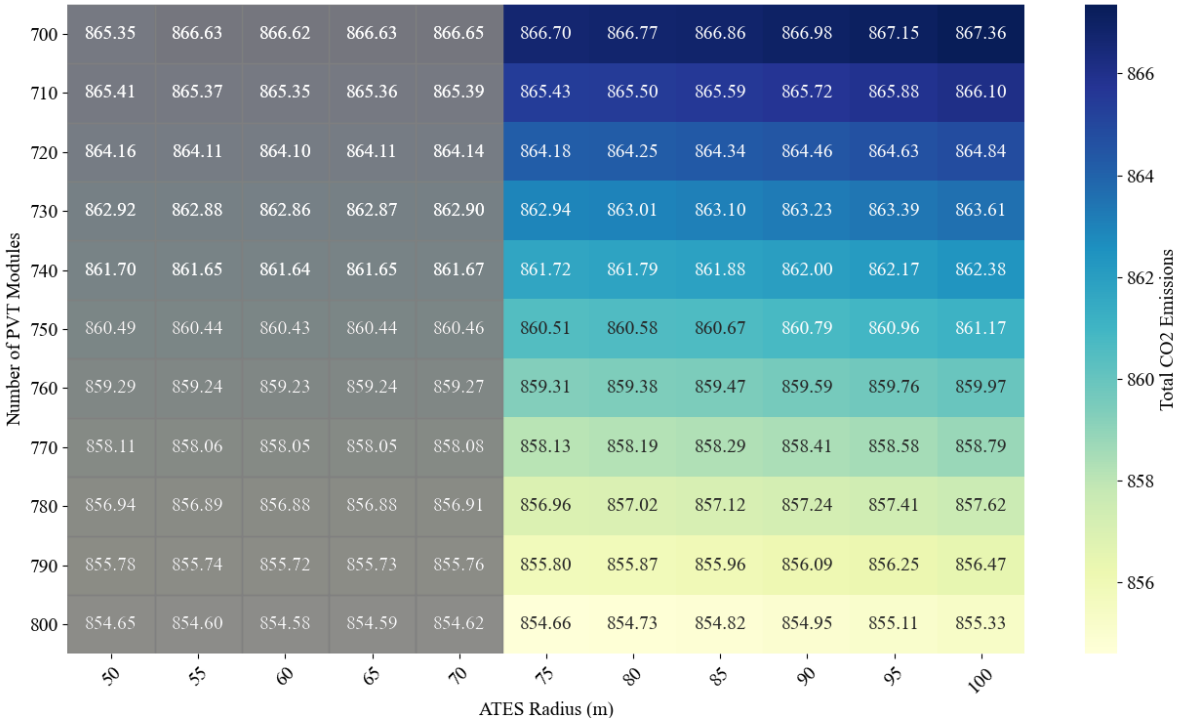

Figure 59: Total CO2 Emissions with 30°C threshold

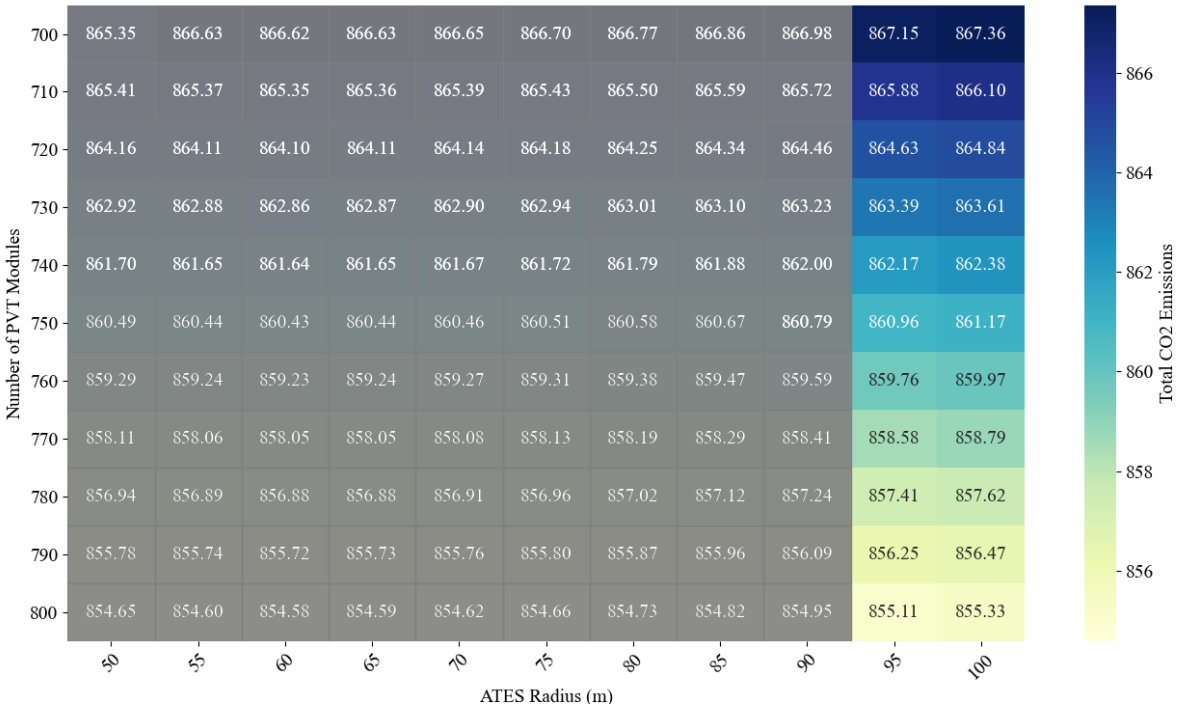

Figure 60: Total CO2 Emissions with 25°C threshold

Next, the optimal solution is identified at the maximum number of PVT modules. A new optimisation expression is formulated, incorporating both the maximum number of PVT modules and the maximum temperature for the ATES. To encompass both the 30°C and 25°C threshold cases, the minimum ATES radius is set at 75 m. To provide a comprehensive view of the wider variation in CO_2 emissions, the maximum ATES radius is extended to 150 m. The operating temperatures for the new radii are constructed with the same method as in Figure 57 and can be found in Appendix A.3. This results in the following optimisation expression.

Minimise

$$CO_2e_{\text{total}}(n, R) = a \times P_{\text{G}}(n, R) + b \times P_{\text{PV}}(n, R)$$

Subject to

$$n = 800$$

$$75 \leq R \leq 150$$

Figure 61 presents the results of the optimisation problem. It illustrates that the amount of CO_2 equivalent decreases as the ATES size approaches its maximum temperature threshold. The two threshold values, maximum 30°C and 25°C, are indicated by red lines. The minimum CO_2 equivalent for both cases occurs precisely at these specific thresholds. Additionally, the data reveals that the deviation of CO_2 equivalent increases with the ATES size, indicating an exponential relationship between the ATES size and the CO_2 equivalent. The difference in CO_2 equivalent between the smallest ATES sizes, R = 75 m and R = 80 m, is merely 80 kg. In contrast, the difference between the largest ATES sizes, R = 145 m and R = 150 m, is as much as a ton of CO_2 equivalent.

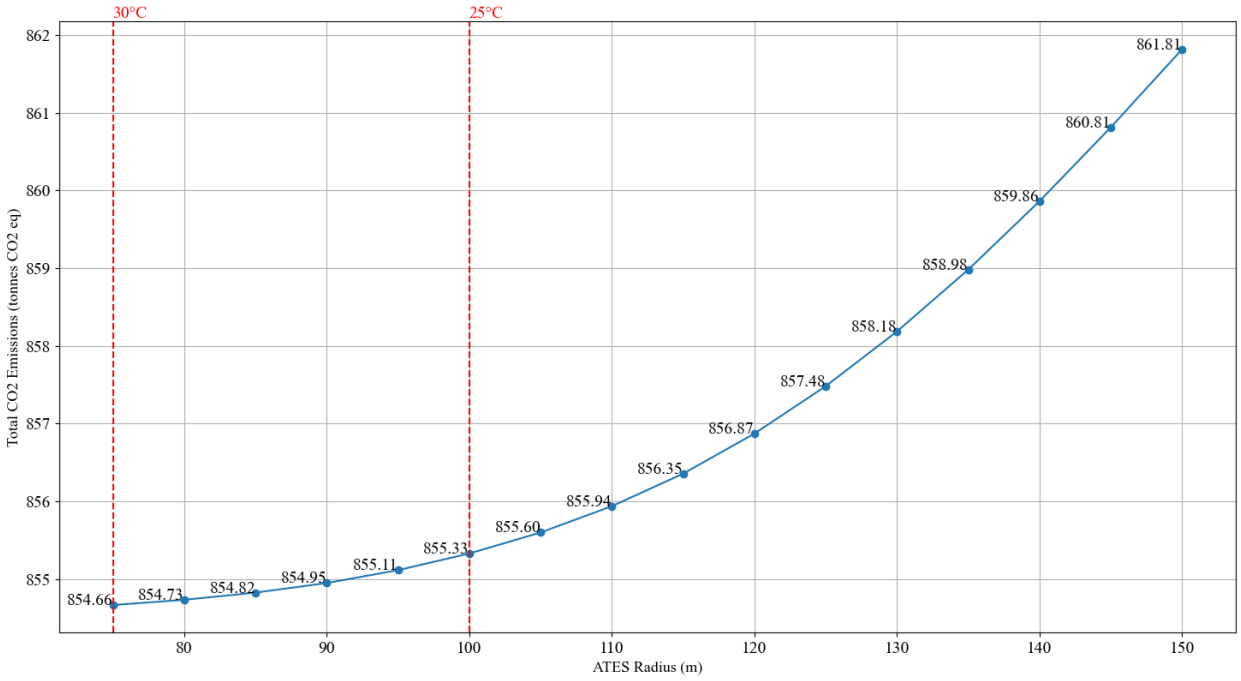

Figure 61: Total CO2 Emissions with 800 PVT modules and maximum temperature threshold

Figure 62 presents the amount CO_2 equivalent against the volume of the ATES. These results are more reflectable for multiple shapes of aquifer.

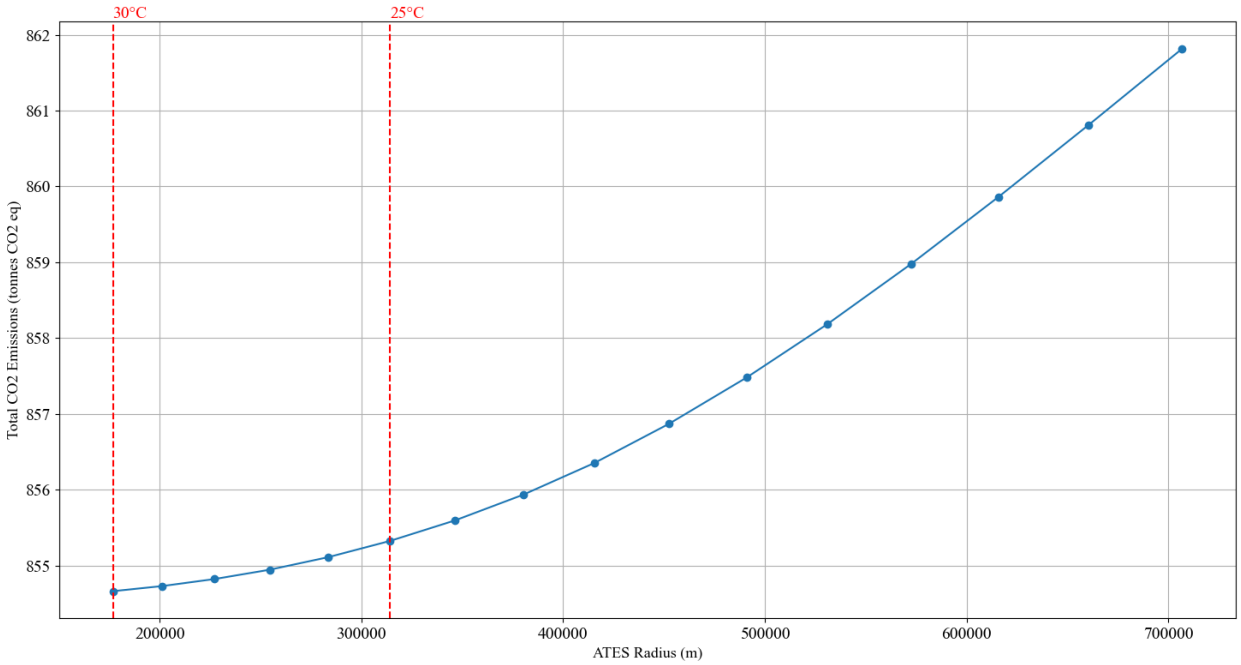

Figure 62: Total CO2 Emissions against ATES volume with 800 PVT modules and maximum temperature threshold

Figure 63 illustrates the percentage increase in CO_2 emissions as the ATES radius expands. While the overall CO_2 emissions exhibit an exponential relationship with the ATES radii, the percentage difference between the data points appears to demonstrate a more linear relationship.

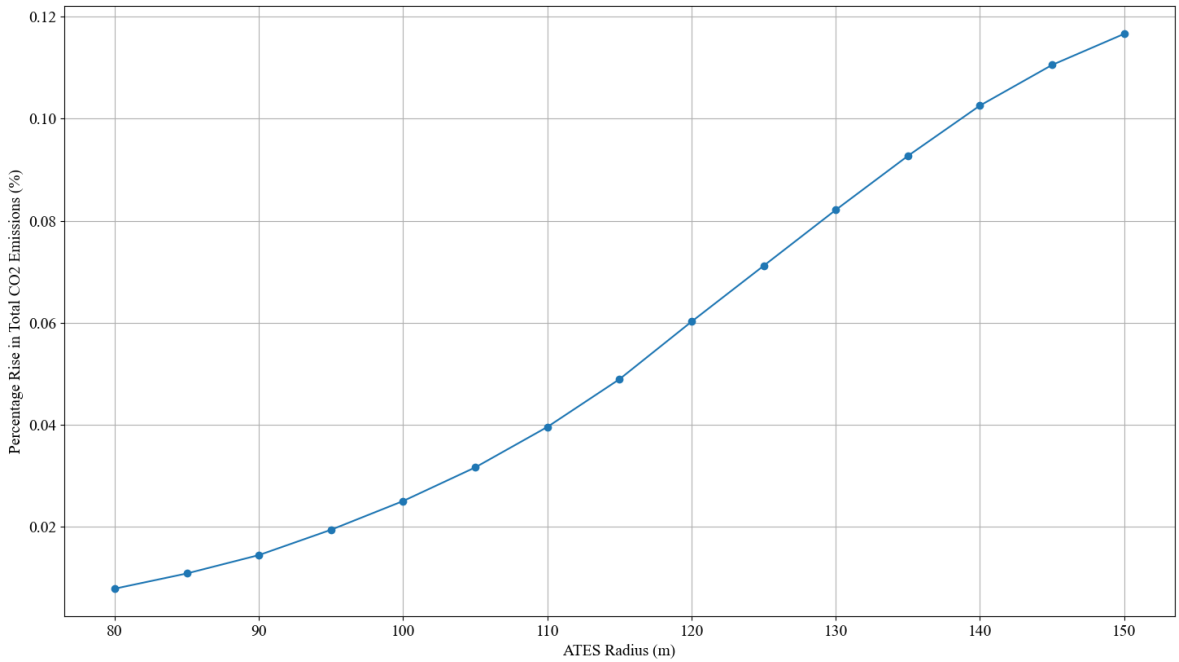

Figure 63: Percentual rise of CO2 Emissions for larger ATES radius

The optimisation analysis provides the following results. The CO_2 emissions caused by the PVT installation are significantly lower than those resulting from grid electricity purchases, leading to optimal solutions at the maximum number of PVT modules. The minimal CO_2 emission solutions can be found at the maximum temperature thresholds for this system. For the optimal aquifer size regarding just CO_2 emissions, the temperatures

becomes too high regarding the maximum temperatures. Additionally, CO_2 emissions remain low within this range of aquifer sizes near the maximum temperature thresholds, resulting in only minor differences between the 30°C and 25°C boundaries, indicating low significance in the results at these temperature borders.

5.4 Discussion

This section discusses the final optimisation results, with a focus on emission factors and the importance of boundary conditions

As discussed in Section 4.4, the model's input conditions are based on data from a single year, including the CO_2 intensities of the Netherlands' power supply. Since the CO_2 intensity of the power supply is decreasing and is expected to continue declining in the coming years. This trend should impact the CO_2 emission optimisation results when the system operates over multiple years.

The effects of ATES temperatures on the subsurface are currently under investigation. Given the novelty of this thermal storage technique, many aspects remain uncertain. Temperature variations and groundwater displacement can lead to changes in hydraulic head changes, groundwater quality, and groundwater ecology. However, the maximum permissible temperature for ATES is still being studied and is highly dependent on the specific situation.

6 Conclusion

In conclusion, this chapter will answer the initial research questions, providing an overall summary of the findings based on the results. Additionally, recommendations for future research will be outlined.

This research describes an analytical model for a case scenario of a multi-carrier energy system, utilising heat pumps, PVT, and ATES to achieve optimal sizing. Multiple configurations and a distribution scenario are analysed, following with the determination of optimal component sizes. The primary goal is to minimise CO_2 emissions, primarily by optimising grid exchange resulting from the system's performance. The research will be concluded by answering the research questions from section 1.3.1.

- What effect has storage distribution and configuration of district heating and ATES have on the thermal performance?

With respect to sorage distribution, a centralised ATES and a distributed ATES case is researched. It can be concluded that a distributed ATES maintained higher temperatures within the district heating network compared to the centralised case with the same ATES volume. Resulting in higher temperatures as input for the heat pumps, enhancing their COP. However, the additional ATES pumps require too much power overruling the slight gain in heat pump performance. Furthermore, the layout of the piping network was deemed insignificant, as the heat loss in the pipes was relatively minimal and did not necessitate optimisation for distance.

An alternative configuration was researched by swapping the sequence of the PVT installation with the ATES. In this configuration, water flows through the PVT installation and then enters the ATES before circulating through the district. This approach results in the ATES being warmed up relatively more, additionally stabilising the water temperatures in the district heating network over the year. However, the overall temperatures in the district heating network are lower compared to the configuration where water flows through the ATES before the PVT installation. This reduction in temperature negatively impacts the heat pump and, consequently, the overall system performance.

- How does the size of the components influence the system's temperature stability throughout a year?

The number of PVT modules directly influences the amount of heat added to the district heating network, which directly influences the system temperature. As the number of PVT modules increases, the system temperature rises, improving performance up to the capacity limit of the PVTs. The size of the ATES system influences the magnitude and variability of temperature throughout the year. When the temperature divergence in the ATES is relatively high, it is largely due to the significant impact of the district heating network, which is more noticeable in smaller ATES systems. These smaller systems experience greater seasonal temperature fluctuations, lower temperatures in winter and higher in summer, because the mass flow of thermal carrier from the district heating network is relatively large compared to the ATES size. Consequently, smaller ATES systems operate at higher temperatures overall, leading to increased heat losses to the surrounding soil, which remains at approximately 11°C. Over time, the temperature within the ATES converges to an equilibrium point, balancing the heat input from the district heating network with the heat losses to the soil. Larger ATES systems, operating at temperatures closer to that of the surrounding soil, experience less seasonal temperature variability, resulting in a more reliable system for storing heat through colder seasons.

- How does the size of the components influence the system's generation capability and net grid exchange?

Increasing the number of PVT modules to the maximum of 800 significantly enhances both the thermal and electrical generation of the system. The thermal output reduces the overall power consumption of the heat pumps, thereby decreasing the amount of electricity drawn from the grid. The electricity generated by the PV modules is largely consumed within the system due to the high power demands of its components, resulting in a low power surplus and minimal grid injection. Thus, maximizing the number of PVT modules optimises system performance.

The size of the ATES has a direct impact on the system's temperature, influencing both the variation and magnitude of temperature throughout the year. This temperature fluctuation, in turn, affects grid exchange because the electricity consumption of heat pumps depends on their COP, which is dependant to the network

temperature. The COP reaches its maximum efficiency at a water inlet temperature around 19.5°C. The grid exchange variation due to network temperature primarily depends on the power usage of the heat pumps. The building load and ATES pump load are fixed values and the PV generation is only marginally affected by network temperature. This implies that an optimal combination of ATES size and the number of PVT modules should be designed to produce water at a temperature that allows each heat pump to operate as close to 19.5°C as possible, where all heat pumps individually extract heat. This balance is crucial because if the water temperature is too low, the COP of the heat pumps decreases. Conversely, if the temperature is too high, heat losses increase, reducing overall system efficiency. Additionally, temperature divergence tends to be higher when the ATES operates at higher temperatures. This causes the importance of achieving a balanced ATES and PVT sizing. This combination should deliver a thermal carrier at a temperature that is near the optimal input for the heat pumps, ensuring the highest efficiency across all pumps for as much of the year as possible.

- What are the optimal component sizes to minimise CO2 emissions while ensuring system reliability and reduce grid power exchange?

The optimal sizes of the components are dependent on the environmental conditions of the underground layers, which set a maximum temperature for the ATES. When high temperatures are feasible, an ATES with a radius of 60 m and a volume of 115,000 m^3 corresponds to the lowest CO_2 emissions. However, the differences in CO_2 emissions with adjacent radii are minimal. Considering maximum temperatures of 25°C and 30°C, the optimal solutions lie at a 75 m radius for 25°C and a 100 m radius for 30°C, corresponding to volumes of around 175,000 m^3 and 315,000 m^3. To ensure system reliability, a relatively larger aquifer offers advantages, reducing the risk of exceeding the maximum temperature and enhancing system stability by making it less dependent on seasonal changes. Taken into account that CO_2 emissions remain low within this range of sizes. An aquifer with a 110 m radius, corresponding to 380,000 m^3, can be considered for this scenario, in combination with 800 PVT modules. This results in an overall emission of 855.98 tonnes of CO_2 equivalent.

6.1 Future research

Given the discussion and conclusion, several recommendations can be made for future research on this topic. Initial improvements should focus on the detailed physics of separate components. Simplifications and assumptions currently in place can affect overall results. Specific research into the heat exchange within and around buildings, as well as the thermodynamics of an ATES, would be useful. Gathering more information on specific buildings can enhance model reliability, such as detailed descriptions of hourly electricity and heat consumption loads, and the specific interior layouts and number of rooms.

Further research should also delve into the electrical network in greater detail, particularly in the context of a multi-energy carrier network, including aspects like cable management, converters, and inverters.

The model itself can also be improved for more in-depth future research. The optimisation focus could shift more towards the optimal inlet temperature of the heat pumps, as this is the sole temperature factor influencing power consumption, thereby simplifying the overall model. Alternatively, the control of the heat pumps could incorporate an economic perspective, adjusting not only to inlet temperature but also to power prices. Additionally, the optimisation focus could be adjusted to include economic factors, such as installation and operational costs, to create a comprehensive business model.

While the current model provides a good approximate representation of a multi-energy carrier system in reality, ongoing research can always contribute to improving these systems for scenarios like this.

references

International Energy Agency. Statistics report Key World Energy Statistics 2021. Technical report, 2021.

International Energy Agency. The Netherlands Energy Mix, 12 2023.

J. Pool, E. Schouten, O. Van Rieven, T. Bal, and R. Spuijbroek. Rapport Vooronderzoek Duurzaam Werfgebied Naar een energiepositieve Werf: Het kan als je het wil! Technical report.

M. Barbu, M. Siroux, and G. Darie. Numerical model and parametric analysis of a liquid based hybrid photovoltaic thermal (PVT) collector. *Energy Reports*, 7:7977–7988, 11 2021.

A. Ramos, I. Guarracino, A. Mellor, D. Alonso-álvarez, P. Childs, N. J. Ekins-daukes, and C. N. Markides. Solar-Thermal and Hybrid Photovoltaic-Thermal Systems for Renewable Heating. *Grantham Institute, Briefing paper No 22. Imperial College London*, (22):1–20, 2017.

A. K. Tiwari, K. Chatterjee, S. Agrawal, and G. K. Singh. A comprehensive review of photovoltaic-thermal (PVT) technology: Performance evaluation and contemporary development. *Energy Reports*, 10:2655–2679, 11 2023.

J. Alpízar-Castillo, L. M. Ramírez-Elizondo, and P. Bauer. Modelling and evaluating different multi-carrier energy system configurations for a Dutch house. *Applied Energy*, 364:123197, 6 2024.

B. Mitterrutzner, C. Z. Callegher, R. Fraboni, E. Wilczynski, and S. Pezzutto. Review of heating and cooling technologies for buildings: A techno-economic case study of eleven European countries. *Energy*, 284:129252, 12 2023.

K. Ninikas, N. Hytiris, R. Emmanuel, B. Aaen, and S. McMillan. A renewable heat solution for water ingress in the Glasgow subway tunnel system. *WIT Transactions on Ecology and the Environment*, 186:161–171, 2014.

S. S. Meibodi and F. Loveridge. The future role of energy geostructures in fifth generation district heating and cooling networks. *Energy*, 240:122481, 2 2022.

K. S. Lee. A review on concepts, applications, and models of aquifer thermal energy storage systems. *Energies*, 3(6):1320 – 1334, 6 2010.

M. Bloemendal and N. Hartog. Analysis of the impact of storage conditions on the thermal recovery efficiency of low-temperature ATES systems. *Geothermics*, 71:306–319, 1 2018.

E. Khlebnikova, I. Pothof, S. van der Zwan, and L. Loverdou. On the design of 5GDHC substation control systems. *International Journal of Sustainable Energy*, 43(1):1 – 16, 1 2024.

S. Jansen, S. Mohammadi, and R. Bokel. Developing a locally balanced energy system for an existing neighbourhood, using the 'Smart Urban Isle' approach. *Sustainable Cities and Society*, 64:102496, 1 2021.

S. Picone, M. Bloemendal, M. Pellegrini, N. Hoekstra, A. Andreu Gallego, J. Rodriguez Comins, and A. Murrel. Novel combinations of aquifer thermal energy storage with solar collectors, soil remediation and other types of geothermal energy systems. pages 11–14, 2019.

J. Jebamalai, K. Marlein, and J. Laverge. Influence of centralized and distributed thermal energy storage on district heating network design. *Energy*, 202:117689, 7 2020.

J. Röder, B. Meyer, U. Krien, J. Zimmermann, T. Stührmann, and E. Zondervan. Optimal design of district heating networks with distributed thermal energy storages – method and case study. *International Journal of Sustainable Energy Planning and Management*, 31:5–22, 2021.

T. Nuytten, B. Claessens, K. Paredis, J. Van Bael, and D. Six. Flexibility of a combined heat and power system with thermal energy storage for district heating. *Applied Energy*, 104:583–591, 4 2013.

M. Geraedts, J. Alpizar-Castillo, L. Ramirez-Elizondo, and P. Bauer. Optimal Sizing of a Community Level Thermal Energy Storage System. *MELECON 2022 - IEEE Mediterranean Electrotechnical Conference, Proceedings*, pages 52–57, 2022.

G. S. Krishna Priya, M. S. Thakare, P. C. Ghosh, and S. Bandyopadhyay. Sizing of standalone photovoltaic thermal (PVT) systems using design space approach. *Solar Energy*, 97:48–57, 11 2013.

D. Testi, E. Schito, and P. Conti. Cost-optimal Sizing of Solar Thermal and Photovoltaic Systems for the Heating and Cooling Needs of a Nearly Zero-energy Building: Design Methodology and Model Description. *Energy Procedia*, 91:517–527, 6 2016.

R. Y.M. Wong, C. Y. Tso, S. Y. Jeong, S. C. Fu, and C. Y.H. Chao. Critical sky temperatures for passive radiative cooling. *Renewable Energy*, 211:214–226, 7 2023.

R. K. Singh and R. V. Sharma. Numerical analysis for ground temperature variation. *Geothermal Energy*, 5(1):1–10, 12 2017.

W. Van Dalfsen. The Shallow Subsurface Temperature Field in the Netherlands. *Advances in European Geothermal Research*, pages 496–505, 1980.

M. Boers and H. van Hateren. Gebiedsstudie bodemenergie. Technical report, VHGM B.V., Hilversum, 2024.

N. Damianakis, G. C. R. Mouli, and P. Bauer. Risk-averse Estimation of Electric Heat Pump Power Consumption. *CPE-POWERENG 2023 - 17th IEEE International Conference on Compatibility, Power Electronics and Power Engineering*, 2023.

HR Energy. productblad-qube.

Z. Sun, Q. Cui, Q. Wang, J. Ning, J. Guo, B. Dai, Y. Liu, and Y. Xu. Experimental study on CO2/R32 blends in a water-to-water heat pump system. *Applied Thermal Engineering*, 162:114303, 11 2019.

S. Bordignon, J. D. Spitler, and A. Zarrella. Simplified water-source heat pump models for predicting heat extraction and rejection. *Renewable Energy*, 220:119701, 1 2024.

T. J. De Boer. Optimization of a Dis-trict Heating Network with the Focus on Heat Loss. Technical report.

Y. A. Cengel, J. M. Cimbala, and R. H. Turner. *Fundamentals of thermal-fluid sciences*.

D. Wessel. *ASHRAE Handbook-fundamentals*. 'Comstock, Stephen', 2001.

Invloed warmtenetten op temperatuur drinkwater. ResultatenTKI Engine.

P. Wallentén. Steady-state heat loss from insulated pipes, 1991.

men in green B.V., The flower farm, Care to change, Werkplaats hanegraaf, Build this up, Imediate holding B.V., and Elcheapo B.V. ENERGIE POTENTIEELSCAN. Technical report.

J. Alpízar-Castillo, L. Ramírez-Elizondo, and P. Bauer. Modelling and Evaluating Different Multi-Carrier Energy System Configurations for a Dutch House.

Meteo data - actual synoptic observations KNMI the Netherlands per 10 minutes.

HR Energy. Productblad Qpanel (HEN).

J. Alpízar-Castillo, V. Vega-Garita, N. Narayan, and L. Ramirez-Elizondo. Open-Access Model of a PV–BESS System: Quantifying Power and Energy Exchange for Peak-Shaving and Self Consumption Applications. *Energies*, 16(14):5480, 7 2023.

Nowtricity. Nowtricity, 2024.

A. Virtuani, A. Borja Block, N. Wyrsch, and C. Ballif. The carbon intensity of integrated photovoltaics. *Joule*, 7(11):2511–2536, 11 2023.

J. Godinaud, P. Loubet, S. Gombert-Courvoisier, A. Pryet, A. Dupuy, and F. Larroque. Life Cycle Assessment of an Aquifer Thermal Energy Storage System: Influence of design parameters and comparison with conventional systems. *Geothermics*, 120, 6 2024.

N. Hoekstra and J. Valstar. Deltares: Aquifer thermal energy storage.

A Appendix

A.1 Parameters model

Table 37: Parameters PVT [36] [38]

Parameter	Symbol	Value	Units	Parameter	Symbol	Value	Units
Glass area	A_{glass}	1.77	m^2	Glass thermal conductivity	k_{glass}	1.8	W/(m·K)
PV area	A_{PV}	1.77	m^2	Air thermal conductivity	k_{air}	0.024	W/(m·K)
Absorber area	A_{a}	1.77	m^2	PV glass thermal conductivity	k_{PV}	1.8	W/(m·K)
Tube area	A_{t}	1.77	m^2	PV EVA thermal conductivity	k_{PV}	0.35	W/(m·K)
Glass density	ρ_{glass}	2200	kg/m^3	PV tedlar thermal conductivity	k_{PV}	0.2	W/(m·K)
PV density	ρ_{PV}	2330	kg/m^3	Fluid thermal conductivity	k_{f}	0.6	W/(m·K)
Absorber density	ρ_{a}	2699	kg/m^3	Insulation thermal conductivity	k_{ins}	0.035	W/(m·K)
Fluid density	ρ_{f}	1050	kg/m^3	Glass specific heat	c_{glass}	670	J/(kg·K)
Glass thickness	L_{glass}	0.0032	m	PV specific heat	c_{PV}	900	J/(kg·K)
Air gap thickness	L_{air}	0.02	m	Absorber specific heat	c_{a}	800	J/(kg·K)
PV glass thickness	L_{PV}	0.003	m	Fluid specific heat	c_{f}	3800	J/(kg·K)
PV EVA thickness	L_{PV}	0.0005	m	Glass diffusivity	α_{glass}	0.9	-
PV tedlar thickness	L_{PV}	0.0001	m	PV diffusivity	α_{PV}	0.9	-
Absorber thickness	L_{a}	0.005	m	Glass emissivity	$\varepsilon_{\text{glass}}$	0.9	-
Insulation thickness	L_{ins}	0.04	m	PV emissivity	ε_{PV}	0.96	-
Mass flow	$\dot{m}_{\text{f}}$	0.029	kg/s	Glass transmittance	τ_{glass}	0.1	-
Tank mass	m_{tank}	2000	kg	Heat exchanger efficiency	η_{r}	0.8	-
				PV cell reference efficiency	η_{PV}	0.2031	-
				PV temperature coefficient	β_{PV}	0.365	%/°C

Table 38: Parameters ATES [25]

Parameter	Symbol	Value	Units
Specific heat of the sand	c_r	830	J/(kg·K)
Specific heat of the fluid	c_f	4200	J/(kg·K)
Density of the sand	ρ_r	1602	kg/m^3
Density of the fluid	ρ_r	1050	kg/m^3
Depth of Aquifer	d	150	m
Soil thermal conductivity	k_{soil}	1.19	W/(m·K)
Soil temperature	T_{soil}	11	°C
Mass flow	$\dot{m}_f$	50	kg/s

Table 39: Parameters Heat Pump [36]

Parameter	Symbol	Value	Units
Efficiency	η_{HP}	0.8	-
Mass flow rate	$\dot{m}_f$	10	kg/s
Specific heat of fluid	c_f	4200	J/(kg·K)
Supply temperature	T_{sup}	53	°C

Table 40: Parameters District Heating [36]

Parameter	Symbol	Value	Units
Mass flow rate	$\dot{m}_f$	50	kg/s
Specific heat of fluid	c_f	4200	J/(kg·K)
Thermal emissivity soil	ϵ	0.25	-
Soil thermal conductivity	k_{soil}	1.19	W/(m·K)
Absorptivity soil	α_0	0.25	-
Stefan-Boltzmann constant	σ	5.67×10^{-8}	$W/(m^2K^4)$
Depth to boundary	d	6	m
Depth of pipe	H	1	m
Inside radius	r_i	0.13	m
Outside radius	r_o	0.4	m
Inner diameter of insulation	r_{i-o}	0.15	m
Thermal conductivity tube	κ_t	398	W/(m·K)
Thermal conductivity insulation	κ_i	0.038	W/(m·K)
Thermal conductivity fluid	κ_f	0.6071	W/(m·K)

Table 41: Parameters ATES pump

Parameter	Symbol	Value	Units
Mass flow	$\dot{m}$	50	$\dot{m}$
Density fluid	ρ_f	1050	kg/m^3
Gravitational acceleration	g	9.81	m/s^2
Depth	h	150	m
Length	L	150	m
Efficiency	η_{ATEP}	0.8	-

Table 42: Parameters of Building [36] [32]

Parameter	Symbol	Value				Unit
		Roof (glass fiber)	Walls (concrete)	Windows (glass)	Windows (cavity)	
Density	ρ	2440	2400	2500	1.025	kg/m^3
Thickness	L	0.2	0.25	0.004	0.014	m
Specific heat	c	835	750	840	1005.4	J/(kg·K)
Conductivity	k	0.04	0.14	0.8	0.0257	W/(kg·K)
Leakage area	A_l	0.01				m^2
Stack coefficient	C_s	0.000435				-
Wind coefficient	C_w	0.000161				-
Heat capacity air	c_a	1012				J/g/K

Table 43: Convective Heat Transfer Coefficients for Buildings [36]

Parameter	Value	Unit
Indoor air - wall	0.9	W/m^2·K
Wall - atmosphere	0.9	W/m^2·K
Indoor air - window (glass)	25	W/m^2·K
Window (glass) - atmosphere	32	W/m^2·K
Indoor air - roof	12	W/m^2·K
Roof - atmosphere	38	W/m^2·K

A.2 Operating temperatures optimisation

75	80	85	90	95	100	105	110	115	120	125	130	135	140	145	150
23.6	23.1	22.5	21.9	21.4	20.9	20.4	19.9	19.4	18.9	18.5	18.1	17.6	17.2	16.9	16.5

Table 44: Operating temperatures (°C) for different ATES radii (m), optimisation n = 800, 75 < R < 150

A.3 Model inputs

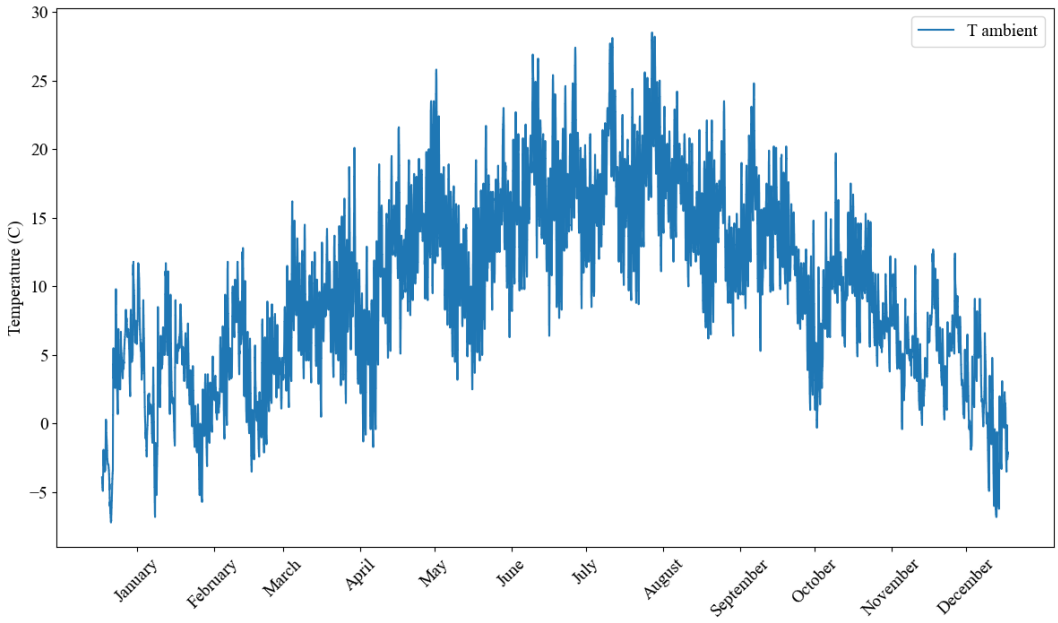

Figure 64: Ambient temperature (°C)

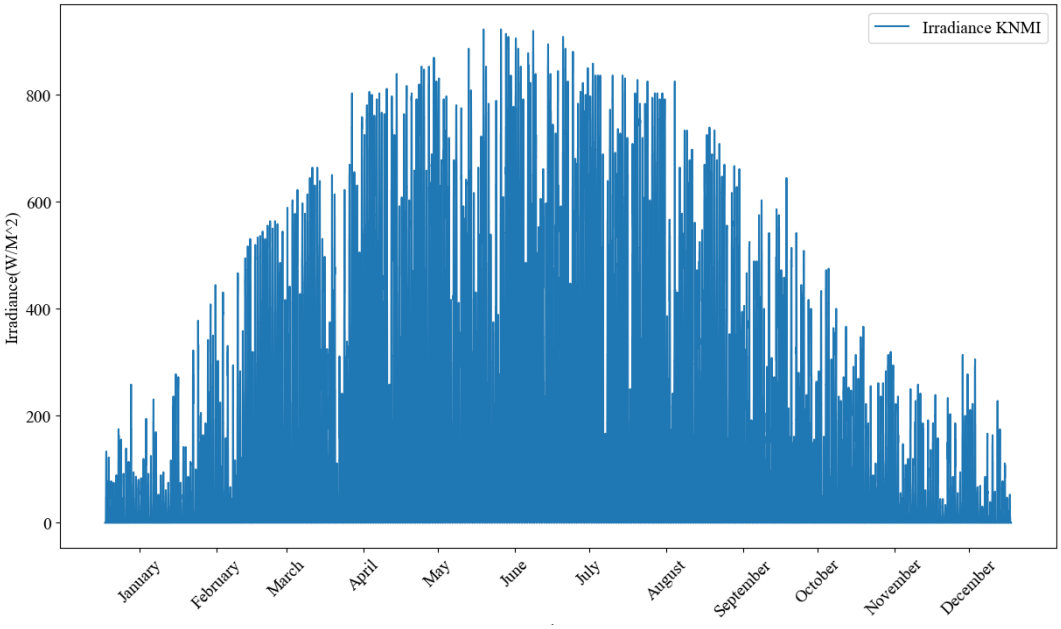

Figure 65: Irradiance (W/m^2)

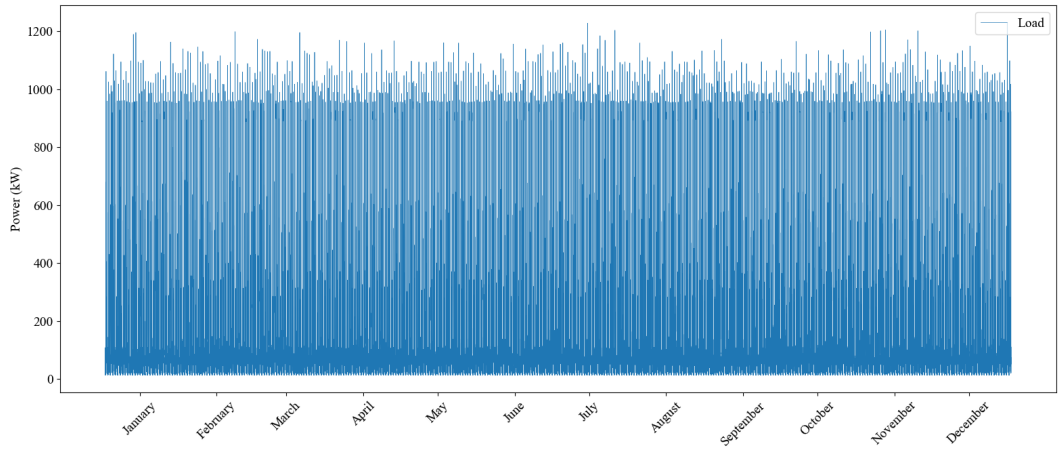

Figure 66: Building load kW

The models used for all calculations can be found here:
https://github.com/TiesB-2017/Photovoltaic-Thermal-System-Design-Model.git
Based on the model used by Joel-Alpízar Castillo [7].